NUMERICAL MODELING OF TIME-LAPSE SEISMIC DATA FROM FRACTURED RESERVOIRS INCLUDING FLUID FLOW AND GEOCHEMICAL PROCESSES

A Dissertation

by

RAVI SHEKHAR

Submitted to the Office of Graduate Studies of
Texas A&M University
in partial fulfillment of the requirements for the degree of

DOCTOR OF PHILOSOPHY

May 2008

Major Subject: Geophysics

NUMERICAL MODELING OF TIME-LAPSE SEISMIC DATA FROM FRACTURED RESERVOIRS INCLUDING FLUID FLOW AND GEOCHEMICAL PROCESSES

A Dissertation

by

RAVI SHEKHAR

Submitted to the Office of Graduate Studies of
Texas A&M University
in partial fulfillment of the requirements for the degree of

DOCTOR OF PHILOSOPHY

Approved by:

Chair of Committee,	Richard L. Gibson
Committee Members,	Akhil Datta-Gupta
	David W. Sparks
	Judith S. Chester
	Mark E. Everett
Head of Department,	Andreas Kronenberg

May 2008

Major Subject: Geophysics

ABSTRACT

Numerical Modeling of Time-Lapse Seismic Data From Fractured Reservoirs
Including Fluid Flow and Geochemical Processes . (May 2008)
Ravi Shekhar, B.S., Indian Institute of Technology (IIT), Kharagpur;
M.S., Indian Institute of Technology (IIT), Kharagpur
Chair of Advisory Committee: Dr. Richard L. Gibson

Fractured reservoirs, especially in low permeable carbonate rocks, are important target for hydrocarbon exploration and production because fractures can control fluid flow inside the reservoir. Hence, quantitative knowledge of fracture attributes is important for optimal hydrocarbon production. However, in some cases fractures can cause leakage of injected CO_2 during enhanced oil recovery (EOR) or CO_2 sequestration. Furthermore, CO_2 can geochemically interact with reservoir fluids and host rock. Hence, time-lapse monitoring of the progress of CO_2 in fractured reservoirs is also very important.

In order to address these challenges, I have developed an integrated approach for studying fluid flow and seismic wave propagation in fractured media using Discrete Fracture Network (DFN) models. My seismic simulation study suggests that CO_2 saturated reservoir shows approximately ten times more attenuation than brine saturated reservoir. Similarly, large P-wave velocity variation in CO_2 saturated reservoir and amplitude variation with offset (AVO) results for our example model predicts that CO_2 is easier to detect than brine in the fractured reservoirs.

The effects of geochemical processes on seismics are simulated by time-lapse modeling for t = 1000 years. My modeling study suggests that intra-aqueous reactions are more significant during injection of CO_2 for t = 6 years, while slower mineral reactions dominate after pressure equilibrium is achieved that is from t = 6 to 1000 years. Overall both types of geochemical reactions cause change in reflection coefficient of 2 to 5%, which may be difficult to detect in some cases. However, the significant change in the seismic properties at the boundary of the CO_2 front can be used to detect the flow path of CO_2 inside the reservoirs. Finally, a method for generating stochastic fracture models was extended and improved to more realistic field model for seismic and fluid modeling. My detail analysis suggests that fractures generated by isotropic stress field favor orthogonal sets of fractures in most subsurface rocks that can be

converted to seismic model, similar to DFN study. The quality and validity of the models is assessed by comparisons to DFN models, including calculations of fractal dimension measures that can help to characterize fractured reservoirs.

ACKNOWLEDGMENTS

First of all, I would like to thank my advisor Dr. Richard Gibson for his guidance during my stay at Texas A&M University. He always introduced challenging problems for research to test my scientific skills. Besides this, he was always there to guide me and help me if I struggled with my research. I would also like to thank my committee members Dr. Datta-Gupta, Dr. Sparks, Dr. Everett and Dr. Chester for their classes and advice on my research problems.

I gratefully acknowledge support for my research from the Department of Energy Basic Energy Sciences under Award No. DE-FG03-00ER15034. I would also like to thank CMG (Compute Modeling Group) for availability of their Green House Gas (GHG) simulator. Special thanks to Dr. Datta-Gupta and Ajitabh Kumar (Dept. of Petroleum Engineering, Texas A&M) for their assistance in flow modeling simulations.

I would also like to thank my colleagues in the Seismic Lab at Texas A&M. Hung-Liang was always nice and a helpful guy. Hung-Liang and Hoa always used to share valuable research suggestions with me. I would also like to thank Jin, John, Pablo, Seung Yoo, Rituparna and Kyubum for all their help.

I also appreciate the support of my family and friends. Last but not the least, I would like to thank my wife, Vinita, for her patience and encouragement.

TABLE OF CONTENTS

Page

CHAPTER Page

CHAPTER Page

LIST OF TABLES

LIST OF FIGURES

FIGURE Page

FIGURE Page

FIGURE Page

FIGURE Page

FIGURE Page

FIGURE Page

FIGURE Page

CHAPTER I

INTRODUCTION

1.1 Motivation and Overview

Fractures and faults are common in the volume of the earth's crust and in many cases control the mechanical strength and transport properties of the solid earth structure. These fractures can originate from several geological processes, and tectonic stress is particularly important (Tod, 2001). The intensity of fracturing and the interconnections of fractures form paths for fluid flow that depend on mineralogy and grain orientation within the rock, as well as the orientation of stress fields (Tod, 2001).

Quantitative measurements of fracture orientation, intensity, and spatial distributions, are very important for optimal hydrocarbon and ground water production or for monitoring the motion of pollutants in the subsurface. This is because fractures can control permeability by providing highly conductive flow paths that dominate fluid flow within a particular geologic formation. An important practical example where this phenomenon can be important for hydrocarbon extraction is in application to carbonate reservoirs, especially those with low matrix permeability. However, in some cases fractures can enhance risk of leaking environmentally hazardous fluids such as carbon dioxide during enhanced oil recovery or CO_2 sequestration. Hence, the knowledge of fracture orientations and distributions is important to monitor the progress of various fluids inside the earth. Since CO_2 is one of the most common injector fluids used by industry for enhanced oil recovery (EOR) and also is a hazardous fluid, it becomes important to monitor the movement of CO_2 inside the earth. Use of CO_2 as injector fluid also helps in sequestrating it in geological formations, known as CO_2 sequestration, to mitigate the effects of greenhouse gases and global warming, though there are still several challenges. One of the key problems is the low density and viscosity of CO_2 in subsurface conditions that may risk in leaking through frac-

---

This dissertation follows the style and format of Geophysics.

tures from the sequestration site into overlying rocks. Furthermore, CO_2 chemically interacts with reservoir fluids and host rocks, so understanding and predicting its behavior during and after sequestration is very important. Leakage of CO_2 through fractures from sequestration sites can lead to acidification of ground water and killing of plant life, besides contamination of the atmosphere (Ha-Dong and Keith, 2003; Ganda et al., 2004). Therefore, it requires improved characterization of the fractured media in which CO_2 is stored and development of advanced methods for monitoring the fluid movement. One of the most effective tools for identifying and mapping the distributions of fractures in such reservoirs is using seismic reflection data, because fractures can alter the seismic velocities and, therefore, amplitudes of seismic reflections.

An important step for interpretation or analysis of the seismic data is to develop rigorous models that relate the the intensity and orientation of fractures to changes in seismic velocities of the composite rock in which the fractures are located. One approach to this problem represents fractures as planar discontinuities in strain, an approach that provides an estimate of the decrease in seismic velocity caused by fractures (Schoenberg, 1980; Schoenberg and Sayers, 1995). Another set of solutions that is frequently applied to modeling and inversion tasks instead begins with a model of cracks as a set of "penny-shaped" (ellipsoidal) voids embedded within the isotropic, homogeneous host rock (Hudson, 1980; Hudson, 1981). When such cracks are randomly oriented, the resulting material is isotropic, but when they are parallel the material has seismic anisotropy (Pointer et al., 2000).

These models, however, neglect the possibility of fluid movement between fractures and a porous, permeable host rock. More recently, Thomsen (1995) showed that the fluid exchange between fracture and host rock as seismic wave propagates across the fracture can be significant. The time-dependent stress generated by seismic waves striking on the fracture surfaces can cause the flow of fluids from fractures to matrix. Simultaneously, this process causes attenuation and dispersion of seismic waves. Attenuation is the measurement of loss of energy and dispersion is the velocity variation with frequency. Also, Thomsen's (1995) study suggests that such phenomenon are more influenced by the crack density rather than crack shape. In fact, this theory for anisotropic fractured rocks produces velocity estimates that much more accurately reproduce laboratory measurements of velocity in anisotropic, fractured materials (Rathore et al., 1991; Rathore et al., 1995). However, the analytical

expressions used to estimate velocities, developed by Thomsen, to relate fractures with fluid flow is restricted for 'low frequency' and 'moderately high frequency' without quantification of frequency range. Since frequency of seismic waves have significant role in flow of fluids from fractures to matrix, so it was important to explore other relationships that can relate the effect of fracture parameters and fluid flow on seismic velocity at each frequency.

Recently Hudson et al. (1996), Pointer et al. (2000), Tod (2001) and Chapman (2003) have attempted to develop theoretical models that relate fracture properties with frequency dependence seismic properties. They also proposed strong attenuation and dispersion of seismic waves due to the presence of fractures in seismic frequency range where the flow between fracture and matrix is maximum. However, so far fewer studies have worked on reservoir scale models that directly incorporate models of fluid flow to develop methods for seismic detection of fluids in fractures. One of the goal of this research is to address this problem by integrating fluid flow, rock physics and seismic attributes to model randomly oriented fractured reservoirs, with a porous background matrix. This configuration is described as an *equant porosity model* (Pointer et al., 2000), in which fluid flows from cracks to porous background matrix and models show strong attenuation and dispersion in the seismic frequency range.

1.2 Objectives and Dissertation Structure

The primary objectives of my research are fracture modeling, integrating fluid flow, geochemical effects and seismic simulation. In detail, the objectives of this research are the following:

- Development of a systematic procedure to convert a Discrete Fracture Network (DFN) model used for flow modeling into a seismic model to relate the fracture properties with seismic velocity. Of late, the DFN technique has gained increasing attention to model complex fracture patterns (Dershowitz et al., 2000; Al-Harbi et al., 2004). The advantage of DFN is its ability to incorporate complex fracture patterns based on field, core, logs, seismic etc. to model fluid flow or the permeability of fracture swarms. However, the discrete set of fractures that comprise the DFN model cannot be used directly in the seismic models, which are instead expressed in terms of the number density of cracks. Hence,

our technique converts discrete fracture model into continuum crack density model for studying the influence of fluid flow on seismic properties.

- Numerical analysis of an equivalent medium theory (Pointer et al., 2000) to study the effects of individual fracture parameters on seismic velocity. Furthermore, based on numerical analysis, several synthetic models of fractured reservoirs on reservoir scale are generated to integrate the effect of fractures on flow and seismic simulation. This also includes modeling of compositional and geochemical reactions of injected CO_2 with reservoir fluids and host rock during CO_2 sequestration in existing or depleted hydrocarbon reservoirs.

- Extend and improve a modeling technique (Masihi and King, 2007) for generating distributions of fractures in a material in mechanical equilibrium to real field model. This method is based on statistical mechanics and stochastic processes and results will be compared with the DFN modeling technique. This modeling method generates correlated fracture models that can be used to improve the predictive capability relating to flow behavior in fractured rock.

1.2.1 Seismic Characterization of Fractured Reservoirs

In chapter II, we proposed a systematic procedure (including development of C++ code) to convert a Discrete Fracture Network (DFN) model used for flow modeling into a seismic model to relate the fracture properties with seismic velocity. This includes numerical analysis of Pointer's theory (Pointer et al., 2000) to study the effects of individual fracture parameters on seismic velocity. Furthermore, based on constraints of numerical analysis, we generate synthetic models of fractured reservoirs on reservoir scale to integrate the effect of fractures on flow and seismic simulation. This study includes the detail analysis of the effects of fractures on frequency dependent seismic attributes such as attenuation and dispersion. It also considers the influence of fluid saturated fractures on complex seismic attributes such as instantaneous amplitude, phase and frequency using full waveform synthetic seismograms computed with the discrete wavenumber method. Furthermore, time-lapse modeling of AVO attributes such as tuning intercept and gradient was analyzed to determine the effect of presence of various types of fluids within fractures. Seismic modeling for this 3D reservoir was performed using ray-Born algorithm which computes reflected amplitude due to small

perturbations caused by fractures saturated with different types of fluids.

1.2.2 Seismic Modeling of Geochemical Reactions in CO_2 Sequestration

In Chapter III, we develop a systematic procedure to model compositional and geochemical reactions of injected CO_2 with reservoir fluids and host rock during CO_2 sequestration. The good candidate geological formations for sequestration sites are depleted oil and gas reservoirs, unmineable coal seams, saline formations, shale and basalt formations. The motivation to use basalt formation is because of unique chemical properties of basalt that converts all injected CO_2 to a solid mineral form thus permanently storing into the formations (Energy, 2008). However, the most mature and effective technology still available for directly minimizing emissions is sequestration in existing or depleted hydrocarbon reservoirs (Hepple and Benson, 2005). Existing and depleted oil and gas reservoirs for CO_2 sequestration are more in demand compare to other formations because of two principal reasons. First, the economic benefits associated with enhanced oil and gas recovery are commercially proven and widely accepted by the industry. Second, oil and gas reservoirs provide abundance data sources such as porosity, permeability, seismic velocity etc. that can be used to design the sequestration sites. Hence, we analyzed our sequestration study in post-water flooded oil reservoirs. Our modeling procedure includes integration of fluid flow data into the seismic and rock physics study to analyze the effects of various geochemical reactions on seismic attributes (AVO attributes and Reflection coefficient) for long time scales for weakly and strongly heterogenous medium. Part of the analysis relied on a new analytic solution for measures of the amplitude of a seismic reflection from a thin reservoir. This new result is an improvement of a previously published equation (Lin and Phair, 1993), and it provides more accurate results for our case.

The goal of this modeling study is to detect the flow path of injected CO_2 inside the reservoirs and provide a prediction of how important geochemical reactions might be for seismic monitoring of CO_2 sequestration. The modeling results suggest that fast reactions such as phase equilibria, intra-aqueous reactions dominate at the early stage of injection. Slow reactions such as mineral reactions dominate after long time scale. The results suggest that the chemical processes cause relatively small changed in seismic amplitude after 1000 years, suggesting that the reduction in the bulk mod-

ulus of the fluid by mixing of the CO_2 with brine and oil will still cause the most significant changes in amplitude. However, significant changes in seismic properties at the boundaries of the CO_2 front can be used to detect the flow path of CO_2 inside the reservoirs.

1.2.3 Statistical and Stochastic Modeling of Fractured Reservoirs

Chapter IV presents an enhanced version of a modeling technique (Masihi and King, 2007) to simulate fractures in mechanical equilibrium to field observation using statistical mechanics and stochastic processes. This includes detailed derivation of pairwise the spatial correlation function integrating elastodynamics, statistical physics and vector field theory. This also includes development of a simulated annealing code using this correlation function as an energy objective function. Several models were generated and compared to understand the effect of medium parameters such as the Poisson ratio, and the effect of boundaries on generating these correlated fracture models in reservoirs. This motivated the incorporation of periodic boundary conditions into the simulated annealing code, as well as other modifications that accelerate computations. The quality and validity of the models is assessed by comparisons to DFN models, including calculations of fractal dimension measures that may help characterize natural fractured reservoirs. Finally, some seismic simulations were carried out using these new stochastic models.

CHAPTER II

SEISMIC CHARACTERIZATION OF FRACTURED RESERVOIR USING HUDSON'S EFFECTIVE MEDIUM THEORY INTEGRATING FLUID FLOW

2.1 Introduction

The accurate characterization of fractured reservoirs to obtain knowledge of fracture direction, intensity, and spatial distributions is of great importance for hydrocarbon production. These fractures control permeability by providing conductive flow paths which can have significant effect on hydrocarbon production especially in low permeable carbonate reservoirs. A great deal of interest exist in developing models relating fracture properties with seismic attributes.

The classical attempts to solve this problem (Schoenberg, 1980; Hudson, 1980; Hudson, 1981; Pointer et al., 2000) were attempted on the assumption of no fluid-exchange either between the fractures themselves or between fractures and matrix. But fluid exchange between different parts of pore spaces during seismic wave propagation has long been recognized (Gassmann, 1951; Mavko and Nur, 1975). Thomsen (1995) has proposed relevant ideas, based on perfect pressure equalization at low frequency, regarding seismic anisotropy due to fractures during transfer of fluid between fractures and 'equant porosity' in the rock matrix. Macbeth and Lynn (2000) used P-waves to detect fracture-induced azimuthal anisotropy. Their approach rely on the detection of amplitude variations in individual prestack common reflection point (CRP), common depth point (CDP), and Common midpoint (CMP) gathers. Beretta et al. (2002) used diffraction tomography theory to develop a linearized AVO and AVA inversion methodology in κ-ω domain that detects fracture density variation within a reservoir using P-wave reflection data. Pérez et.al (1999) used azimuthal variation of P-wave AVO responses to detect the fracture orientation in oil and gas reservoirs. Zhu et al. (2004) suggested two- step seismic inversion algorithm for inverting reservoir crack density from P-wave AVOA data.

Brown et al. (2003) observed that P- and S-wave anomalies are observable with the saturation changes in fractured media. P wave requires long wave offsets for

saturation changes whereas S-waves can increase or decrease while going from brine- to gas- saturation in the reservoirs. Also, the sign of S-wave anomaly associated with saturation changes depends upon fracture orientation and the magnitude of these anomalies depend upon the relative compliance of fractures and the saturating fluids. Angerer et al. (2003) provided an integrated approach of seismic processing, stratigraphic inversion and DFN modeling to complete seismic-to-simulator workflow.

Recently Hudson et al. (1996), Pointer et al. (2000), Tod (2001) and Chapman (2003) have attempted to develop theoretical models to relate fracturing with seismic properties. They proposed strong attenuation and dispersion of seismic waves due to the presence of fractures in seismic frequency range. However, so far fewer studies have worked on developing reservoir scale models for detecting fluids in fractures.

Our goal in this paper is to model randomly oriented fractured, isotropic reservoirs with a porous background matrix. This configuration is described as an *equant porosity model* (Pointer et al., 2000), in which fluid flows from cracks to background matrix. These models show strong attenuation and dispersion of seismic waves in the seismic frequency range. Our starting reference model of the reservoir, developed by petroleum engineering colleagues, is a discrete fracture network (DFN) dual porosity model for fluid flow simulations that has randomly oriented fractures in porous matrix (Al-Harbi et al., 2004). This is the reason we chose the isotropic fracture theory, even though many results suggests natural fracture distributions may be anisotropic.

Below we outline the basic theory used to describe the seismic properties of the reservoir and present some results illustrating the types of frequency dependence predicted for these properties. We then summarize how we create a seismic model from the DFN reference model and show predicted AVO parameters for this model.

2.2 Background Theory

Pointer et al. (2000) suggested an expression for the effective tensor of elastic constants $\mathbf{C}$ of cracked material in terms of perturbations to the moduli of the uncracked host rock. The perturbations are expressed in powers of crack density $\epsilon = \nu\mathbf{a^3}$, where ν is the number density of cracks. The cracks were assumed to be circular for simplified analytical expressions and the theories are valid for a low aspect ratio $\mathbf{c/a}$, where $\mathbf{a}$ is the crack radius and c is the crack half- thickness. The general expression for the

effective elastic constants of cracked material $\mathbf{C}$, accurate to second order in crack density ϵ, is given by Hudson (1986)

$$\mathbf{C} = \mathbf{C^0} + \epsilon\mathbf{C^1} + \epsilon^\mathbf{2}\mathbf{C^2}, \tag{2.1}$$

where $\mathbf{C}^0$ is the elastic tensor for the isotropic (possibly porous) matrix material, $\mathbf{C}^1$ represents the effective changes in moduli caused by first order scattering by cracks, and the second term $\mathbf{C}^2$ gives the crack-crack interactions. These theories also assume that crack distribution is dilute so that crack density ϵ is less than 0.1. The most challenging part is the calculation of $\mathbf{C}^1$, which can be expressed as function of compliances of a single crack,

$$\mathbf{C^1} = \mathbf{C^1}(\mathbf{U_{11}}, \mathbf{U_{33}}), \tag{2.2}$$

where $\mathbf{U}_{11}$ measures the response of the crack to shear traction, and $\mathbf{U}_{33}$ is the response to normal traction. The second-order term $\mathbf{C}^2$ can be written in terms of $\mathbf{C}^1$ as

$$C^2_{ijkl} = \frac{1}{\mu} C^1_{ijrs} \chi_{rstu} C^1_{tukl}, \tag{2.3}$$

where

$$\chi_{ijkl} = \{\delta_{ik}\delta_{jl}(4 + \beta^2/\alpha^2) - (\delta_{ij}\delta_{kl} + \delta_{il}\delta_{jk})(1 - \beta^2/\alpha^2)\}/15, \tag{2.4}$$

and α and β are the respective P- and S-wave speeds of the matrix material.

When the cracks are aligned with normals along the 3-axis, equation 2.2 can be written as

$$C^1_{ijkl} = -(1/\mu) C^0_{s3ij} C^0_{t3kl} U_{st}, \tag{2.5}$$

where

$$\{U_{st}\} = \mathrm{diag}\{U_{11}, U_{11}, U_{33}\} \tag{2.6}$$

Equation 2.5 & 2.6 can be used to calculate effective elastic constants of anisotropic, aligned cracks, cracked material.

Pointer et al. (2000) introduced three distinct mechanisms for wave-induced fluid flow within cracked solid: flow between connected cracks through seismically transparent pathways in almost non-porous material, flow within the partially saturated cracks due to differential pressure gradient, and diffusion from cracks to background porous matrix through mechanically invisible pathways which is also referred to as the *equant porosity model*.

The resulting parameters for this model are given by Hudson et al. (1996) as follows:

$$\begin{aligned} U_{11} &= \frac{16}{3}\frac{(\lambda+2\mu)}{(3\lambda+4\mu)}\Big/(1+M) \\ U_{33} &= \frac{4}{3}\frac{(\lambda+2\mu)}{(\lambda+\mu)}\Big/(1+K), \end{aligned} \tag{2.7}$$

where

$$\begin{aligned} M &= \frac{4a}{\pi c}\frac{i\omega\eta_f}{\mu}\frac{(\lambda+2\mu)}{(3\lambda+4\mu)} \\ K &= \frac{a}{\pi c}\frac{\kappa_f}{\mu}\frac{(\lambda+2\mu)}{(\lambda+\mu)}\Big(1+\frac{3(1-i)J}{2c}\Big)^{-1}. \end{aligned} \tag{2.8}$$

The parameter J is related to matrix and fluid by

$$J^2 = \phi_m \kappa_f K_m / 2\omega\eta_f, \tag{2.9}$$

and J must be positive. Appendix A gives the detail derivation of these parameters for equant porosity model.

The Lamé parameters for the solid background matrix are λ and μ, κ_f is the bulk modulus of the fluid and η_f its viscosity, c /a is the crack aspect ratio, ω is the angular frequency, and K_m is the permeability of the unfractured host rock. The quantity M measures the effect of viscosity of fluid in-fill in cracks response to shear whereas K measures the effect of the compressibility within the cracks.

The first order perturbations to the elastic moduli with respect to solid background matrix in the isotropic equant porosity model are (Equation 58, (Pointer et al., 2000))

$$\begin{aligned} \frac{\kappa^1}{\kappa} &= -\frac{\kappa}{\mu}U_{33} \\ \frac{\mu^1}{\mu} &= -\frac{2}{15}(2U_{33}+3U_{11}) \end{aligned} \tag{2.10}$$

Hence, the effective bulk and shear modulii for the rocks containing fractures upto first order of approximation is

$$\begin{aligned} \kappa_{eff} &= \kappa_0 + \epsilon\kappa^1 \\ \mu_{eff} &= \mu_0 + \epsilon\mu^1 \end{aligned} \tag{2.11}$$

where κ_0 and μ_0 is the saturated bulk and shear modulus of isotropic porous matrix. These saturated rock properties can be calculated using Gassmann equation (Equation 2.14).

The corresponding P- and S-wave velocities in such rocks are given by

$$\begin{aligned} V_p &= \sqrt{\frac{\kappa_{eff} + \frac{4}{3}\mu_{eff}}{\rho}} \\ V_s &= \sqrt{\frac{\mu_{eff}}{\rho}} \end{aligned} \tag{2.12}$$

The real and imaginary parts of these parameters can be used to determine $Q_p{}^{-1}$ and velocity dispersion for specific choices of parameters using following equations

$$\begin{aligned} Q_p^{-1} &= \frac{2Im\{V_p\}}{Re\{V_p\}} \\ Q_s^{-1} &= \frac{2Im\{V_s\}}{Re\{V_s\}} \end{aligned} \tag{2.13}$$

The expressions developed in this theory has the following assumptions (Peacock and Hudson, 1990):

- the radius of cracks a and the separation between cracks are assumed to be much less than the wavelength of seismic waves ($ka << 1$ where k is the wavenumber);
- the position of cracks are randomly distributed within the scale of seismic wavelength;
- the distribution of cracks are sparse and disconnected, and their total volume is a small fraction of the volume of the rock. In other words, crack distribution is diluted so that $\epsilon < 0.1$;
- the shape of the cracks are oblate spheroid with very small aspect ratio; and
- the material in cracks are much softer than matrix.

2.2.1 Seismic Rock Properties

The amplitude of seismic waves reflecting from a formation containing CO_2 or another fluid will depend on the properties of both the fluid itself and of the porous

rock matrix. Specifically, seismic compressional and shear wave velocities will change as fluid properties vary, and a common model describing these variations is the Gassmann equation (Gassmann, 1951). This solution assumes isostress conditions for an isotropic, homogenous, monominerallic rock at the low frequency limit. While the shear modulus μ of the rock is predicted to remain constant by this theory, the bulk modulus of the saturated rock depends on several properties of the fluid and solid components:

$$\kappa_{sat} = \kappa_{dry} + \frac{(1 - \frac{\kappa_{dry}}{\kappa_s})^2}{\phi(\frac{1}{\kappa_f} - \frac{1}{\kappa_s}) + \frac{1}{\kappa_s}(1 - \frac{\kappa_{dry}}{\kappa_s})} \tag{2.14}$$

Here κ_{dry} is the bulk modulus of the drained rock sample, κ_s is the mineral grain bulk modulus, κ_f is the fluid bulk modulus, and ϕ is the porosity.

In most cases, the formation will be partially saturated with brine, oil and another fluid such as CO_2 . In our time-lapse models, we can have all three fluids present and the bulk modulus of the mixture is given by Woods equation (Mavko et al., 2003) as

$$\frac{1}{\kappa_f} = \frac{S_1}{\kappa_1} + \frac{1 - S_1}{\kappa_2}, \tag{2.15}$$

where κ_i is the bulk modulus of fluid i, S_i is the saturation of that fluid. This is easily extended to three fluids. The bulk density of the formation is simply the volume average of the density of each component present in the fluid-saturated rock.

$$\begin{aligned} \rho_{bulk} &= (1 - \phi)\rho_{matrix} + \phi(\rho_{CO_2} S_{CO_2} + \\ &\quad \rho_{oil} S_{oil} + \rho_{water}(1 - S_{CO_2} - S_{oil})) \end{aligned} \tag{2.16}$$

2.2.2 Seismic AVO Attributes

The amplitude of a seismic reflection from a boundary between two materials is approximately a linear function of the squared sine of the angle of incidence i (Shuey, 1985):

$$R(i) \approx R(0) + Gsin^2 i \tag{2.17}$$

Appropriately processed prestack seismic data, when sorted into common reflection point, or common midpoint, gathers, provide a measure of this reflection coefficient. Typical amplitude variation with offset (AVO) analysis fits a line to these measured

reflection amplitudes to estimate the intercept R(0) and gradient G. The intercept is equal to the normal incidence reflection coefficient and can be considered an estimate of the seismic amplitude that would be observed in a typical seismic section. The values of these two parameters generated by hydrocarbon or CO_2 bearing formations are often significantly different from those of brine-saturated rock, providing a valuable tool for detecting fluids of interest.

In our model, however, the reservoir, with thickness b=20 m, is sufficiently thin that reflections from the top and bottom of the layer will interfere for seismic frequencies typical of surface seismic data (about 30 Hz) and so we cannot directly utilize the (Shuey, 1985) result. Lin and Phair et al. (1993) showed that composite reflection associated with this superposition or tuning still has the same general functional form, but the intercept and gradient of the line take the form:

$$R_t(0) = (4\pi bf)/V_g R(0) \tag{2.18}$$

$$G_t = ((4\pi bf)/V_g)(G - R(0)/2) \tag{2.19}$$

Here f is frequency, V_g is the interval velocity in the reservoir formation, and R(0) and G are the conventional AVO intercept and gradient respectively for the upper interface of the reservoir. By utilizing this tuned AVO solution, we obtain much faster results than we would with a simulation of the synthetic seismograms followed by processing.

2.3 Numerical Analysis

Table 2.1 lists parameters describing our model. The host rock in our model is drained carbonate rock saturated with three different fluids for our analysis. They are brine, liquid CO_2 (27°C and 7.5 MPa) and SCF CO_2 (77°C and 7.5 MPa). The critical temperature and pressure for carbon dioxide is 31°C and 7.4 MPa. Carbon dioxide exists in a supercritical fluid phase above the critical temperature and pressure, and this phase has lower viscosity, lower density and higher volume expansion than other phases of CO_2. Distinguishing phases may therefore be very useful.

Figure 2.1 shows attenuation in brine saturated and CO_2 saturated cracked media as a function of frequency. At high frequencies, the cracks behave as isolated cracks, as fluids do not move quickly enough into the porous medium to relax the stress field. This result in constant velocity and negligible attenuation at higher frequencies.

Table 2.1. Reservoir model parameters

Matrix Properties	V_p	4516 ms^{-1}
(Carbonate)	V_s	2631 ms^{-1}
	ρ	2400 kg/m^{-3}
	$K_{mineral}$	74.8 GPa
	ϕ_m	10 %
	K_m	10 mD
Fluid properties	K	2.25 GPa
(Brine)	ρ	1000 kg/m^{-3}
	η_f	$10^{-3}\ Pa-s$
Fluid properties	K	0.0983 GPa
(SCF CO_2)	ρ	150 kg/m^{-3}
	η_f	$2^{-5}\ Pa-s$
Fluid properties	K	0.739 GPa
(Liq. CO_2)	ρ	733.9 kg/m^{-3}
	η_f	$5^{-5}\ Pa-s$
Crack Properties	a	5 m
	c	1 mm
	ϵ	0.05

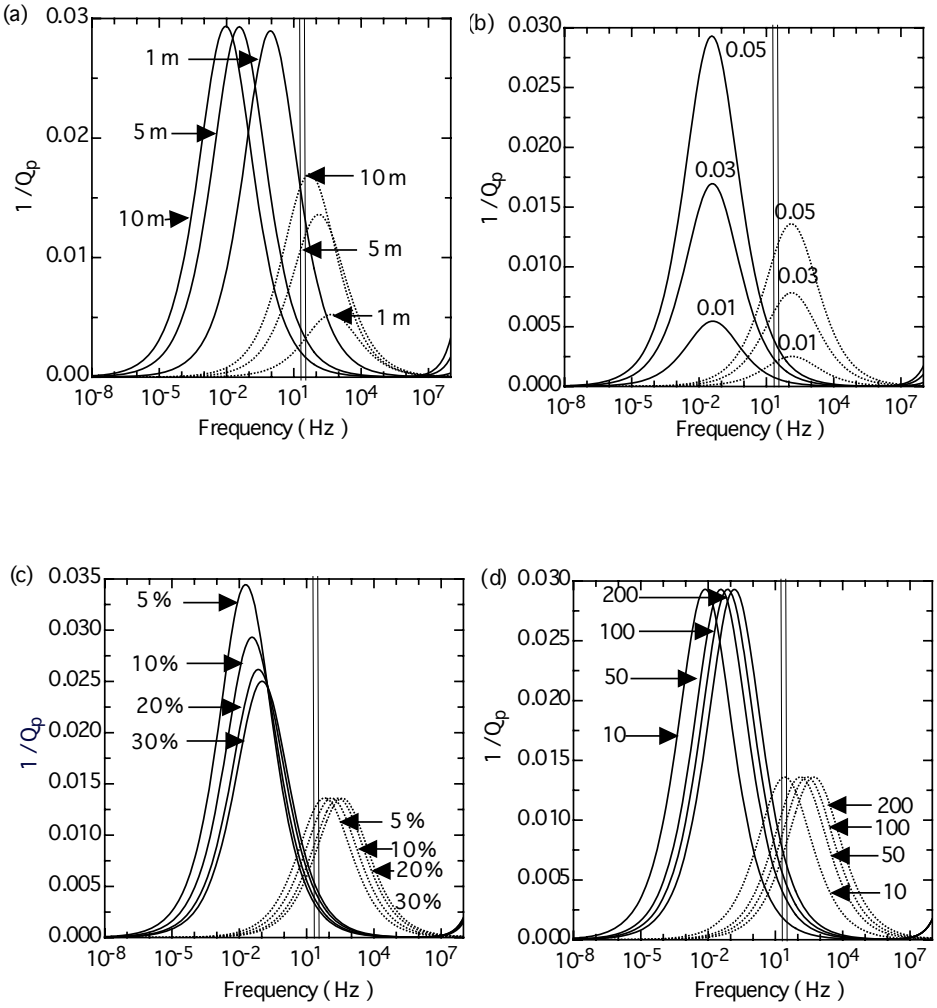

Fig. 2.1. Dependence of attenuation on (a) crack radius (b) crack density (c) matrix porosity and (d) matrix permeability in brine (solid line) and SCF CO_2 (dashed line). The vertical bars represents seismic frequency zone.

In mid-frequency ranges, SCF CO_2 and Liquid CO_2 show much higher attenuation than brine saturated cracks, which is caused by the higher incompressibility of brine in the saturated cracks. On the other hand, at low frequency the pressure in the fluids has sufficient time to equilibrate, and the rocks behave as drained rocks, or dry rocks, in which attenuation becomes negligible and velocity becomes constant with frequency (Pointer et al., 2000). Velocity dispersion is also greatest at the same frequencies where attenuation has maxima, so simulating and measuring its effects at seismic frequencies may also provide important information for reservoir studies.

These results show that the theory described by Hudson (1996) and Pointer et al. (2000) suggests a significant attenuation of seismic waves in frequencies of interest for hydrocarbon exploration. However, the complicated forms of the equations make it difficult to assess the sensitivity of properties to the various parameters. Thus Figure 2.1 compares results for changes in several important properties for brine (solid line) and SCF CO_2 (dashed line), suggesting that crack radius and permeability have the most significant effect on attenuation and dispersion. Figure 2.1(a) suggests that attenuation increases with increase in crack radius and also introduces attenuation at lower frequencies. This result is consistent with Chapman's (2003) argument that the presence of large fractures introduces significant attenuation and dispersion within seismic frequency band. This is because relaxation time for fluids in larger cracks is higher and hence, has lower squirt frequency for fluid migration. Attenuation also generally increases with increasing permeability, though the effect is small. However, the quantitative *difference* in attenuation between the two fluids near seismic frequency range decreases with increasing permeability. For seismic fluid detection in the exploration frequency range, the most important point is whether or not there is a significant difference in attenuation values between the two fluids, as measuring such a difference from field data might provide additional attributes to distinguish them in reservoirs. In this light, Figure 2.1(d) shows that the maximum difference in attenuation for two fluids occurs for comparatively small matrix permeabilities, suggesting that it will be most straightforward to use attenuation as a fluid indicator for lower permeability reservoirs.

2.4 Reservoir Modeling and AVO Study

The specification of the reservoir model begins with a discrete fracture network (DFN), in which fracture planes are mapped in 3D space using statistical properties of fracture swarms, fracture network geometry and streamline flow characteristics (Al-Harbi et al., 2004). This synthetic reservoir model is 920 m×920 m, discretized into smaller cells of 43.8 m×43.8 m for geocellular modeling . The stochastically generated fractures are randomly oriented either at 45^o or 135^o. This is also the starting model used for fluid flow simulations, and we therefore begin with the same reference model, an example of which is shown in Figure 2.2. The corresponding permeability model is also displayed in Figure 2.3, and it is used for streamline fluid flow simulations.

The fracture theory, however, requires a value of crack density in each cell in the model, requiring us to convert the DFN representation into a comparable crack density map. To derive this seismic model, we considered the cracks to be imperfections on fractures planes (Liu et al., 2000) and calculated the total area occupied by rectangular fractures in each cell. The basic assumption of such kind of models is that the mechanical response of a fracture with a complex structure remains approximately the same as fracture with circular cracks or welds with the same crack statistics (Liu et al., 2000). We then compute the number of circular cracks occupying the same area in the cell and use this to assign the number density required by the equivalent medium theory. We can express this as

$$\sum_{i=0}^{N} A_{rectangular} = \pi a^2 N, \tag{2.20}$$

where N is the total number of rectangular fractures in the cell and a is the effective crack radius of each cell. So, the crack density is then $\epsilon = \nu \mathrm{a}^3$ where $\nu = N/V$ and V= area of each cell× thickness of the reservoir layer which is assumed to be 20 m. The resulting crack density model shown in Figure 2.4.

Figure 2.5 compares attenuation and P-wave velocity variation in the presence of brine and SCF CO_2 in our seismic model. The brine saturated reservoir shows negligible attenuation in comparison to SCF CO_2, which is consistent with our previous analysis (Figure 2.1). In fact, SCF CO_2 saturated reservoir shows approximately ten times more attenuation than brine saturated reservoir. Similarly, P-wave velocity variation in SCF CO_2 saturated reservoir is much larger than brine saturated

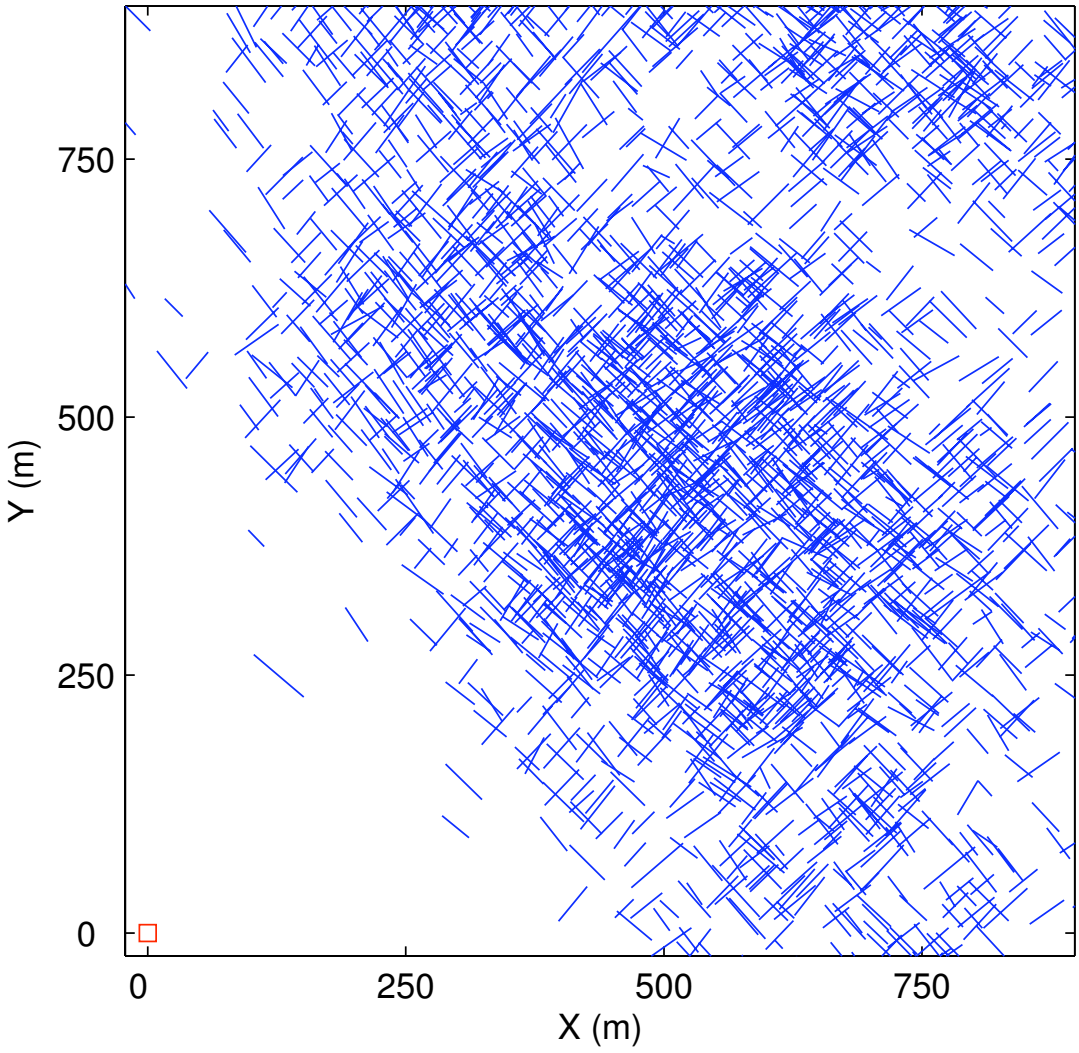

Fig. 2.2. Discrete Fracture Network (DFN) model generated by mapping 3-D fracture planes.

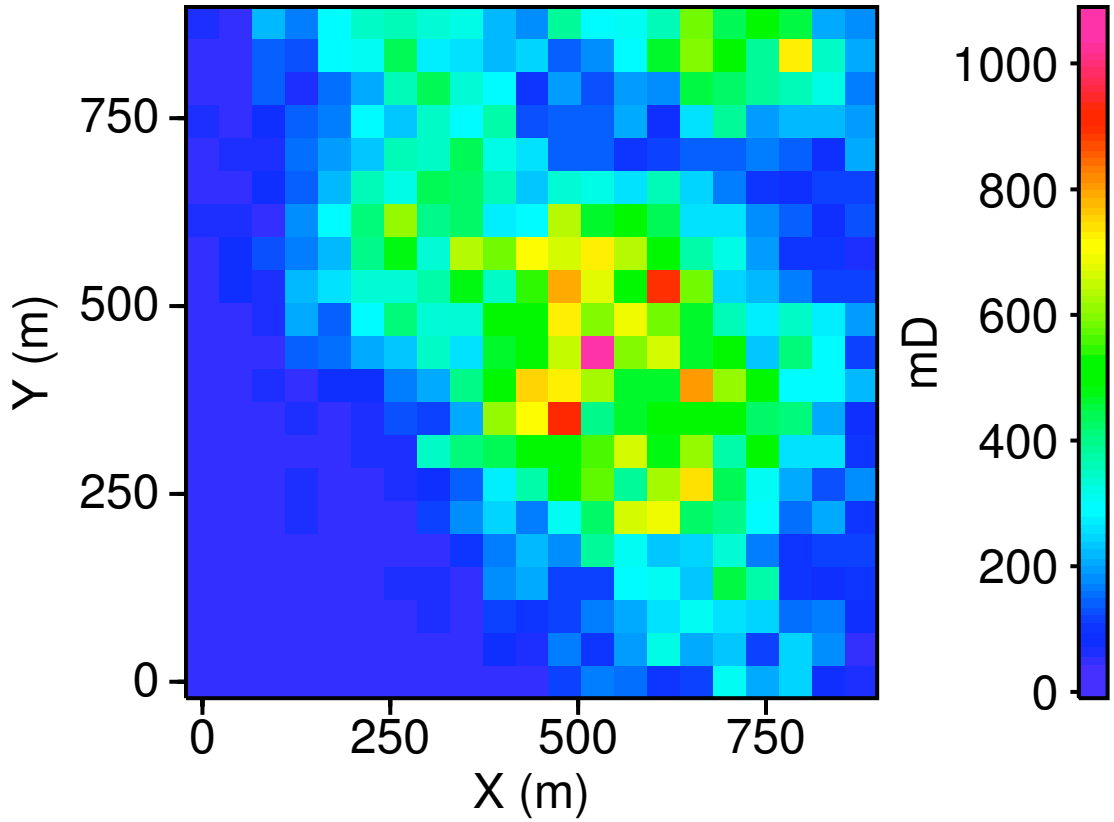

Fig. 2.3. Permeability model derived from the DFN model using empirical relationships.

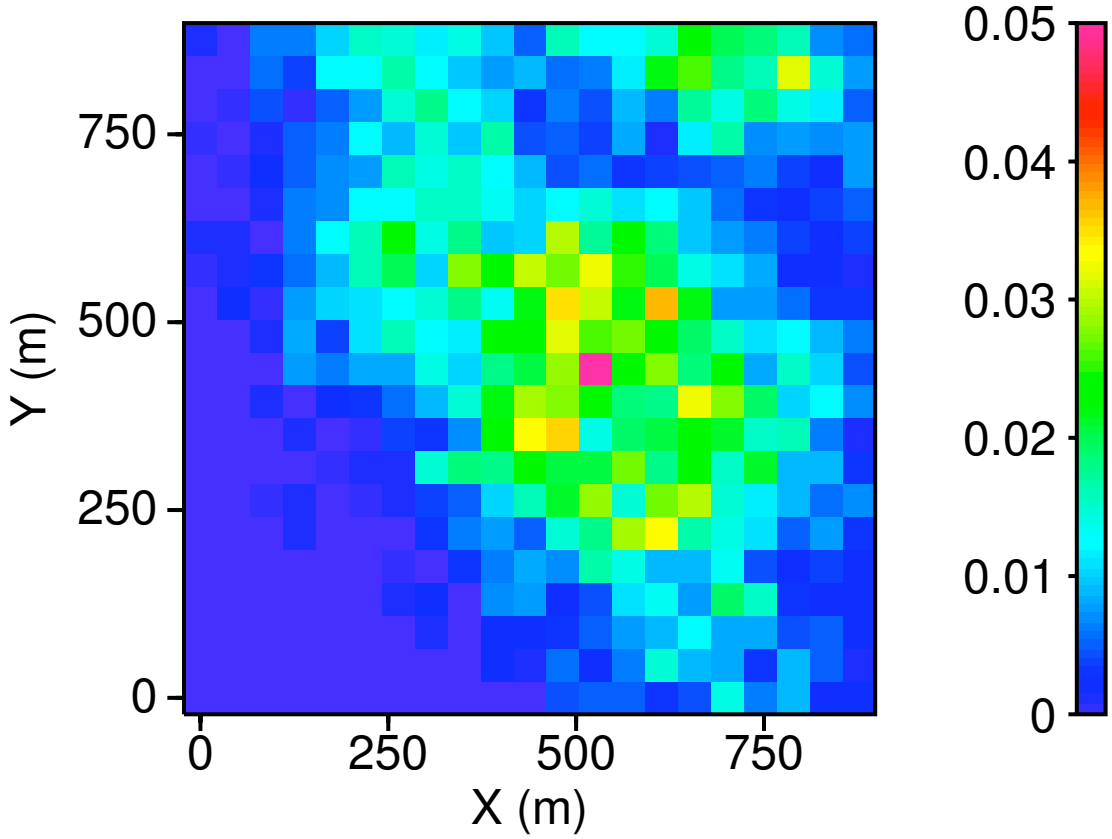

Fig. 2.4. Crack density model generated from the DFN model using procedures described in the text (see equation 2.20).

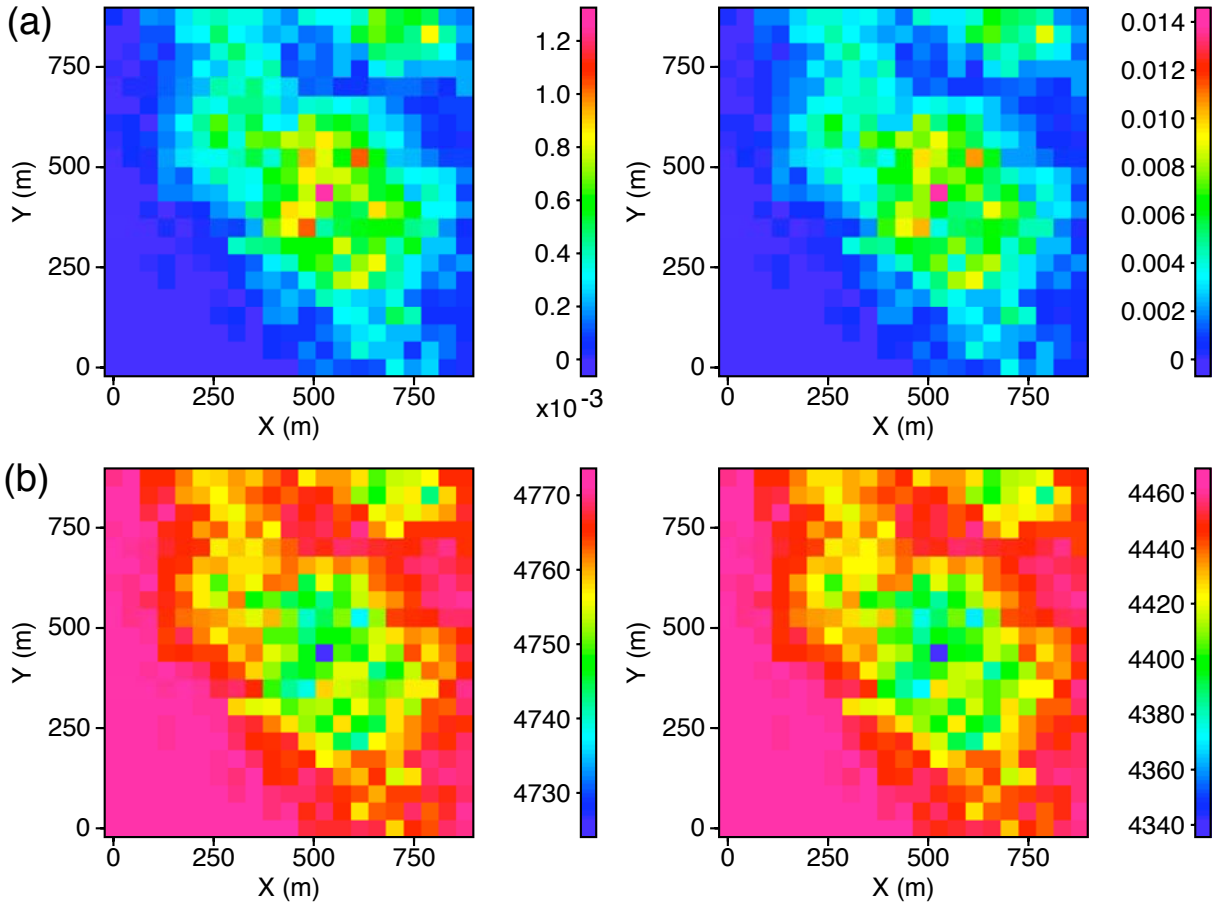

Fig. 2.5. (a) Attenuation in brine and SCF CO_2 (left and right, respectively) at 30 Hz. (b) Dispersion in brine and SCF CO_2 (left and right, respectively) at 30 Hz. SCF CO_2 saturated reservoir shows approximately ten times more attenuation than brine saturated.

reservoir.

To simulate AVO parameters, the fractured carbonate reservoir was assumed to be at a depth of 1000 m. AVO parameters were computed for this reservoir, which was assumed to be 20 m thick, and bounded by media with velocities V_p=4000 m/s, V_s=2309.6 m/s and ρ=2200 kg/m^3. This 20 m fractured reservoir was assigned 10% porosity and 10 mD permeability. The following equations were used to estimate intercept and gradient for our the tuned reflections from this reservoir layer (Lin and Phair, 1993):

$$R_t(0) = ((4\pi bf)/V_g)R(0) \quad (2.21)$$

$$G_t = ((4\pi bf)/V_g)(G - R(0)/2) \quad (2.22)$$

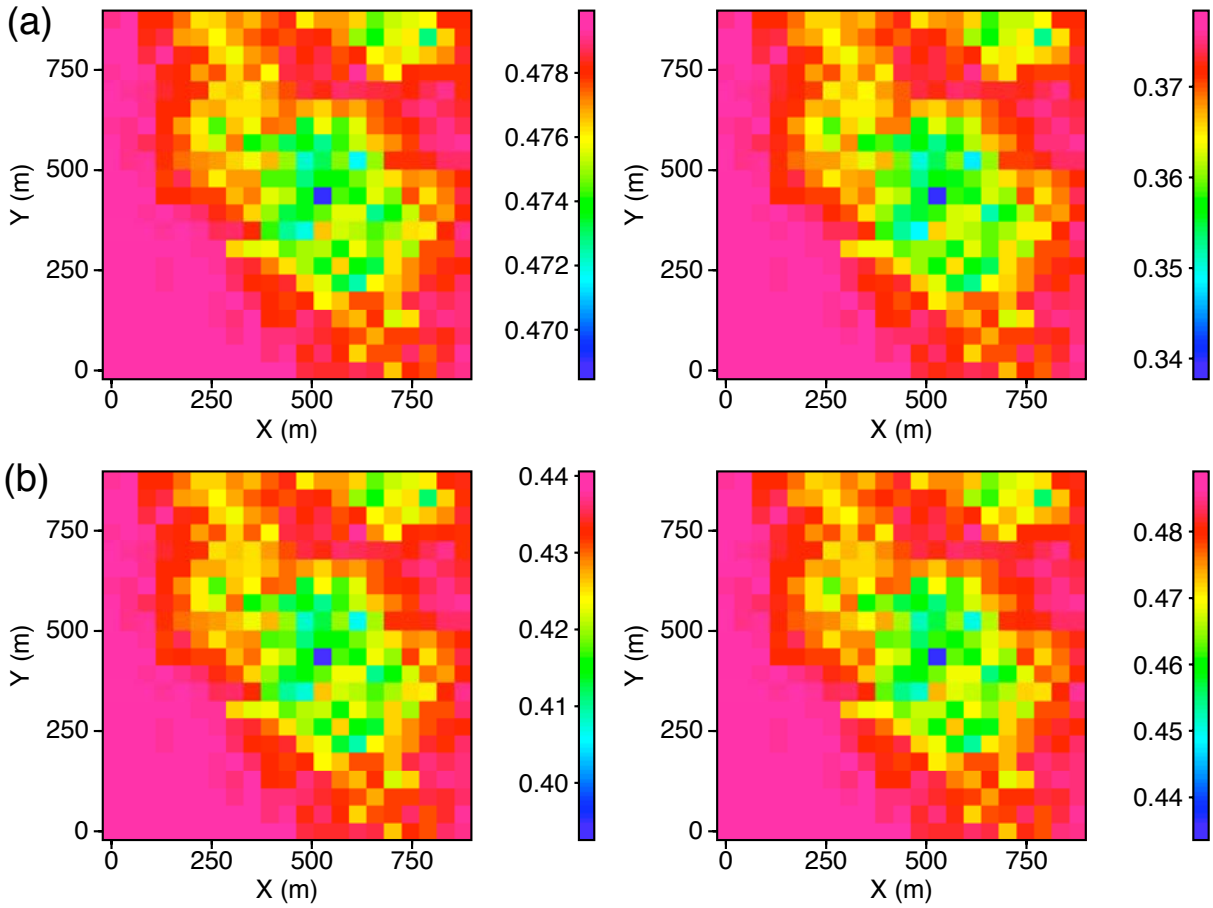

Fig. 2.6. (a) Tuned AVO intercept for brine and SCF CO_2 (left and right, respectively) (b)Tuned AVO gradient in brine and SCF CO_2 (left and right, respectively) in the thin reservoir layer model at 30 Hz. Brine results show about 1.3 times larger intercept values and approx. 1.2 times lower gradient values than SCF CO_2.

Here R_t and G_t represent the tuned intercept and gradient. V_g is the P-wave velocity within the thin layer reservoir, b is the thickness of reservoir and f is the frequency of measurement. $R(0)$ and G are the intercept and gradient, respectively, from the top interface of the thin layer model. V_g of this thin layer is calculated using Equation 2.10 in the thin fractured carbonate layer.

The AVO response from the thin layer model is shown in Figure 2.6 for a frequency of 30 Hz. This figure suggests that brine saturated reservoir has an intercept 1.3 times larger and approx. 1.2 times lower gradient than the SCF CO_2 saturated reservoir. Similar types of observation can be seen in for conventional AVO for a single interface. Also, SCF CO_2 saturated reservoir shows 13% increase in intercept values

with respect to background matrix in comparison to 4% increase in Brine saturated reservoirs. Similar quantification can be made for AVO gradient values in different cases. So, AVO attributes can be used primarily to distinguish fluids in a particular reservoir.

2.5 Complex Trace Attributes

There are other attributes including instantaneous amplitude, phase and frequency that may be applied to characterize attenuating fractured reservoirs. These instantaneous attributes are measured from analytic signal composed the seismic trace (real part) and its Hilbert transform (imaginary part) (Taner et al., 1979). In order to examine these attributes, a reservoir geometry was specified at a depth of 1 Km having crack density to be 0.05.The goal of this modeling study was to examine the effectiveness of instantaneous amplitude, phase and frequency for comparing attenuation in thin (20 m) and thick (240 m) reservoirs and compare fully brine and SCF CO_2 response in fractured reservoirs. Full waveform synthetic seismograms used for the modeling were computed with the discrete wavenumber method.

2.5.1 Tuning Effects

Figure 2.7 and Figure 2.8 shows synthetic seismograms and their associated instantaneous attributes for 20 m thin and 240 m thick fractured attenuating reservoir respectively. The reflections from the 20 m thin reservoir are fully tuned for the source frequency of 30 Hz. Increasing thickness to 240 m eliminates the effects of tuning and emphasizes the influence of attenuation (Figure 2.8).

2.5.2 Effects of Q on Attributes

To determine the influence of Q on both sets of seismograms, they were recomputed without Q effects and subtracted from the reservoir model results for SCF CO_2 saturated reservoirs. Though Q has negligible influence on the amplitudes for the thin reservoir (Figure 2.9), it does still change phase by approx. 15° at large offset, suggesting analysis of field data could search for this effect. Effects are more significant for the thick reservoir (Figure 2.10), which shows changes in all three attribute types.

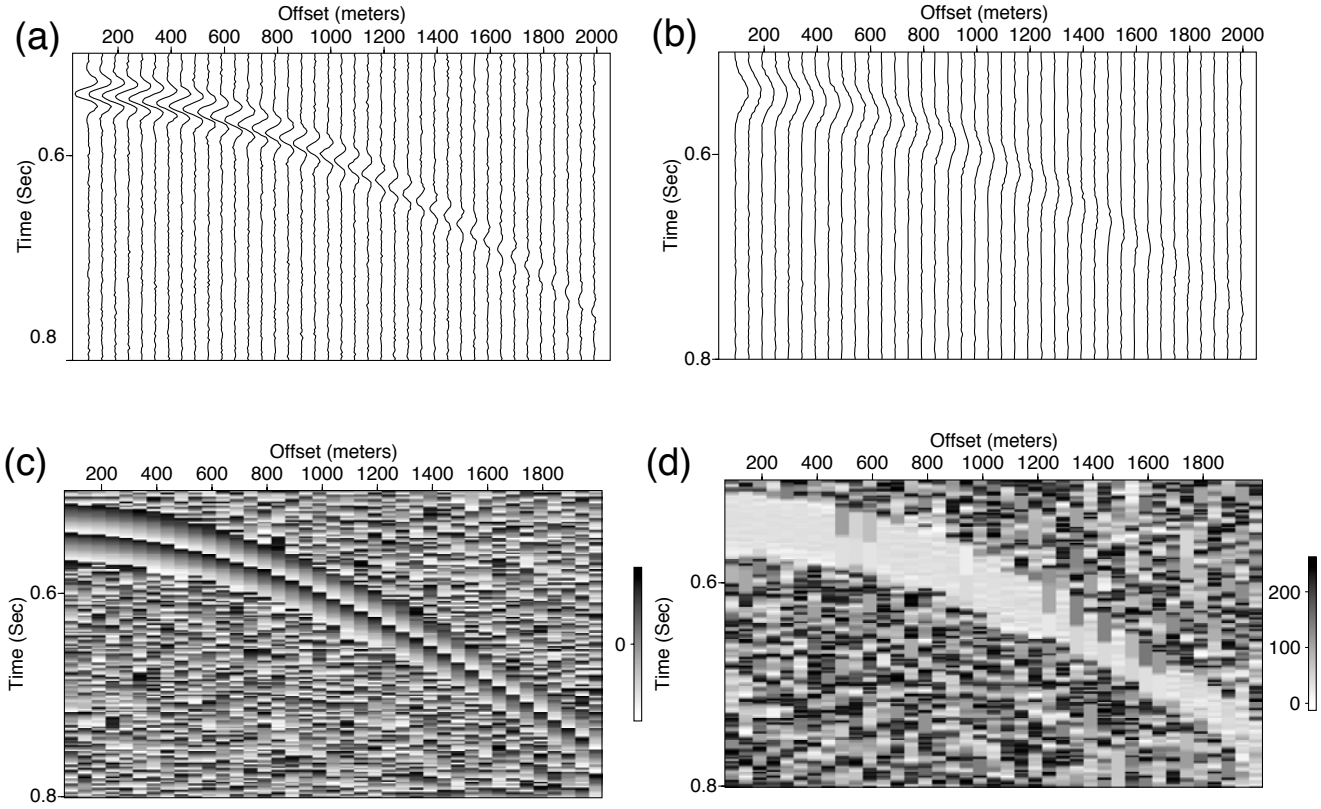

Fig. 2.7. Original synthetic seismograms and associated instantaneous attributes for a 20 m thin reservoir with SCF CO_2. Here, explosion is used as source and (a) is the vertical component of source (b) instantaneous amplitude (c) instantaneous phase and (d) instantaneous frequency.

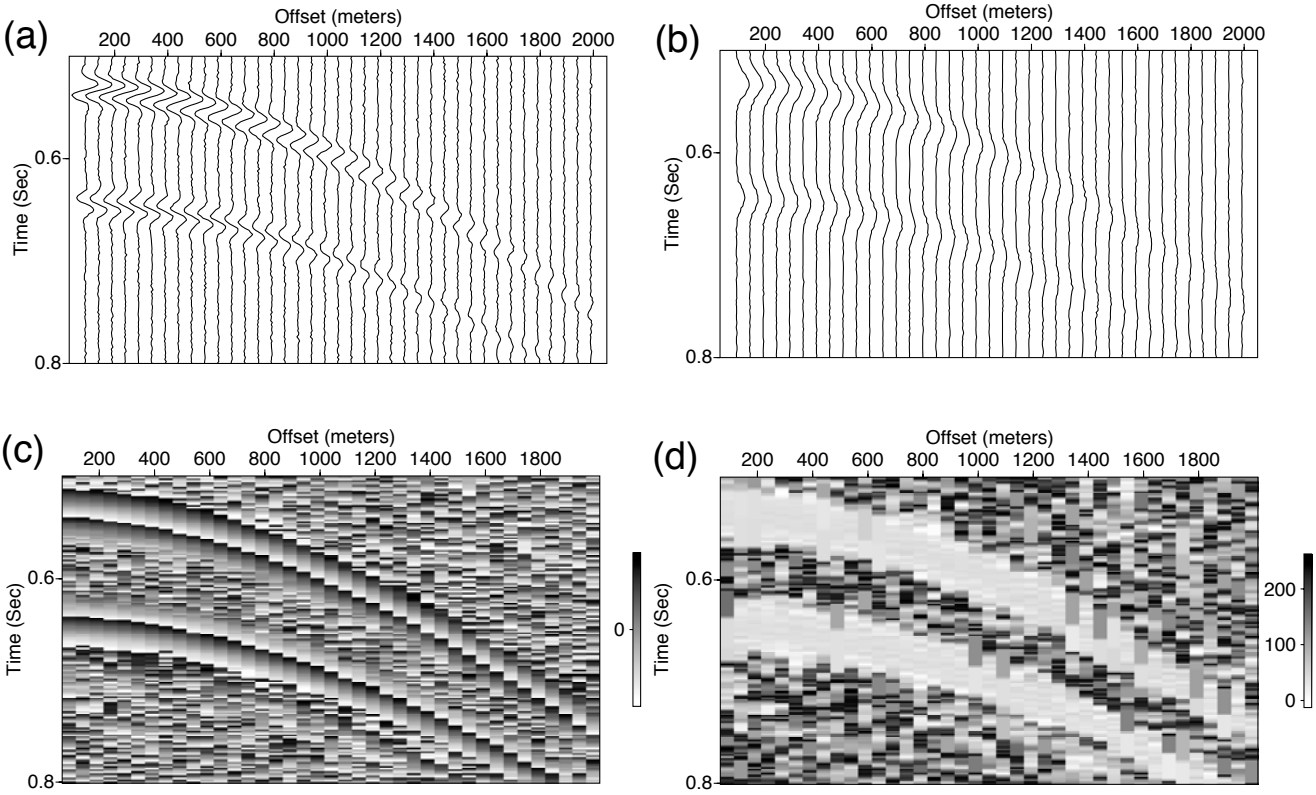

Fig. 2.8. Original synthetic seismograms and associated instantaneous attributes for a 240 m thick reservoir with SCF CO_2. Here source is explosion and (a) is the vertical component of source (b) instantaneous amplitude (c) instantaneous phase and (d) instantaneous frequency.

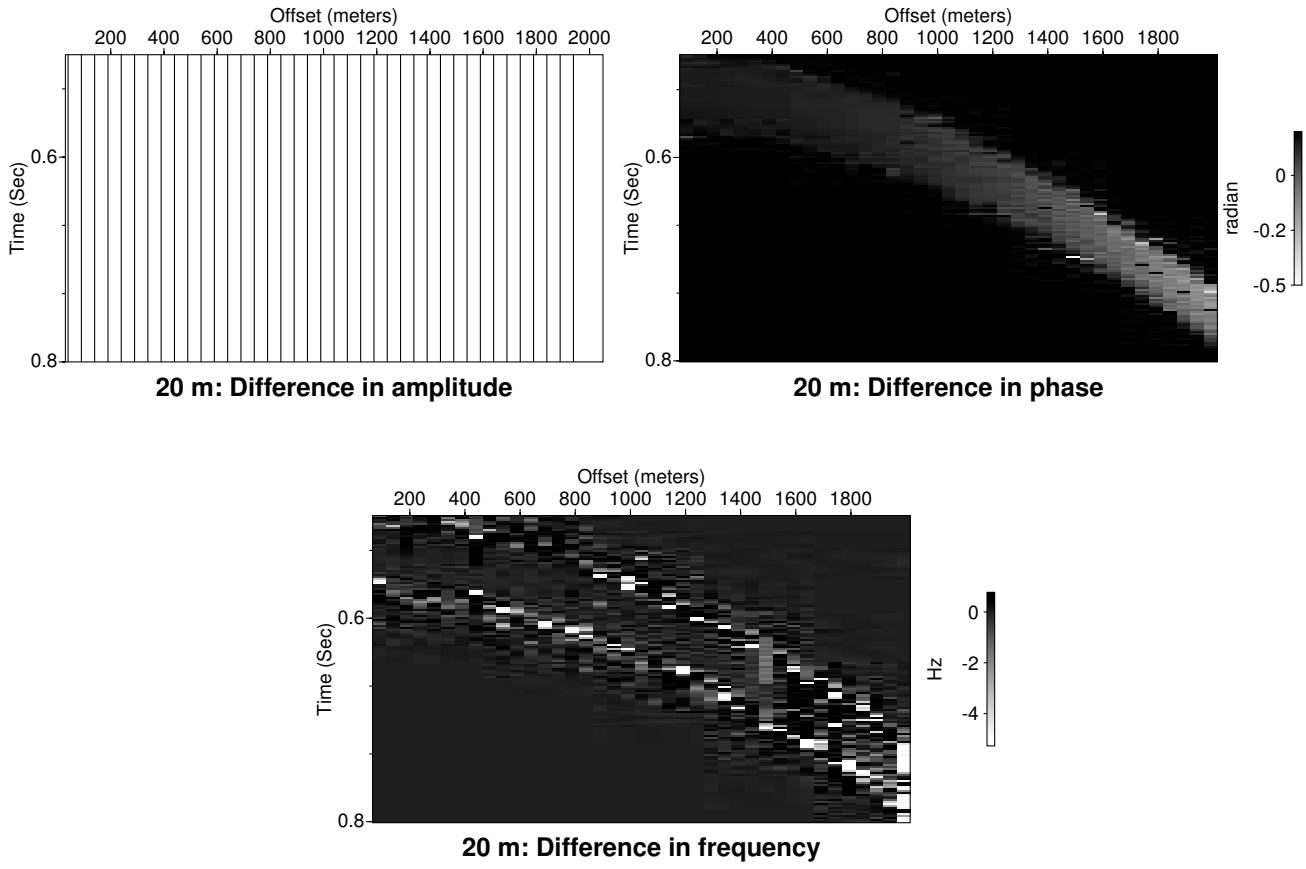

Fig. 2.9. Attribute changes computed by subtracting results for models with and without Q effects for a 20 m thin reservoir with SCF CO_2. Instantaneous phase changes by approx. 15° at large offset.

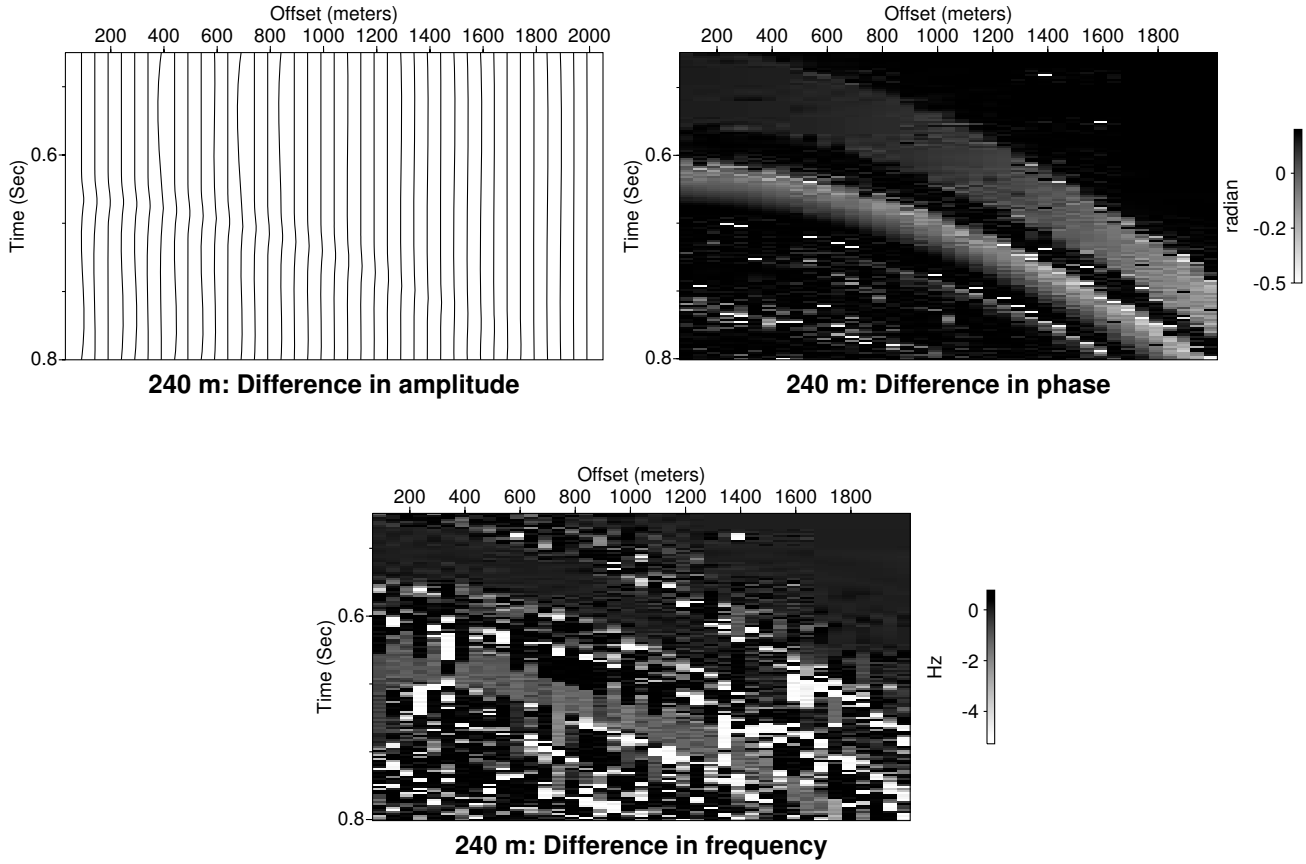

Fig. 2.10. Attribute changes computed by subtracting results for models with and without Q effects for a 240 m thin reservoir with SCF CO_2. Significant difference in amplitude and phase from bottom surface indicate the presence of gas saturated reservoir.

Significant visible difference in instantaneous amplitude and phase from bottom of the surface indicates the presence of gas saturated reservoir.

2.5.3 Distinguishing Fluids with Attributes

One of the goal of this modeling study was to use the seismograms to distinguish different fluids within the fractured reservoir, either in a single experiment or in multiple time-lapse expermients. Synthetic seismograms for brine and SCF CO_2 for the 20 m (Figure 2.11) and 240 m (Figure 2.12) thick reservoirs were computed and again subtracted to emphasize differences. The seismic amplitude plots are displayed with the same scales as the original synthetic seismograms. Figure 2.11 suggests signifi-

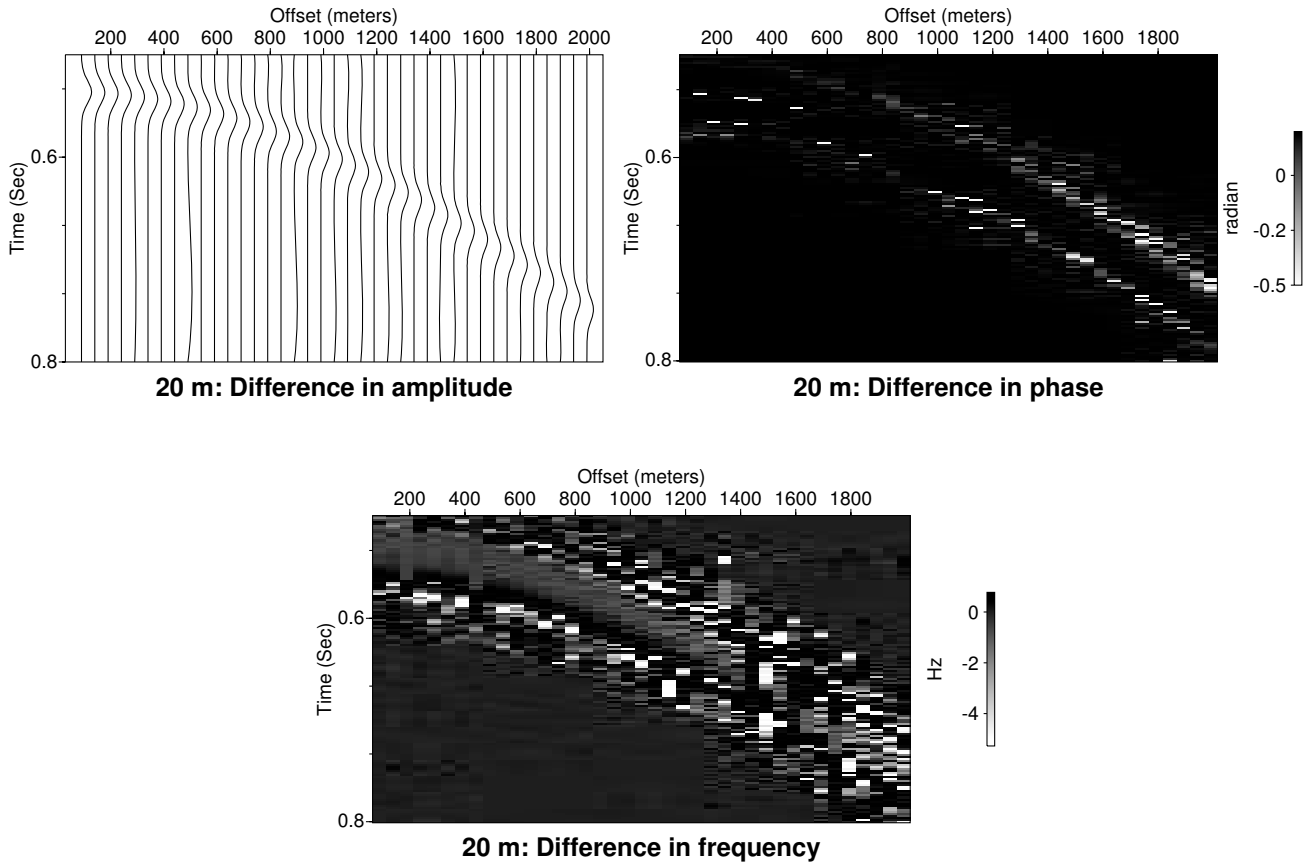

Fig. 2.11. Difference in attributes for brine and SCF CO_2 computed for the 20 m reservoir.

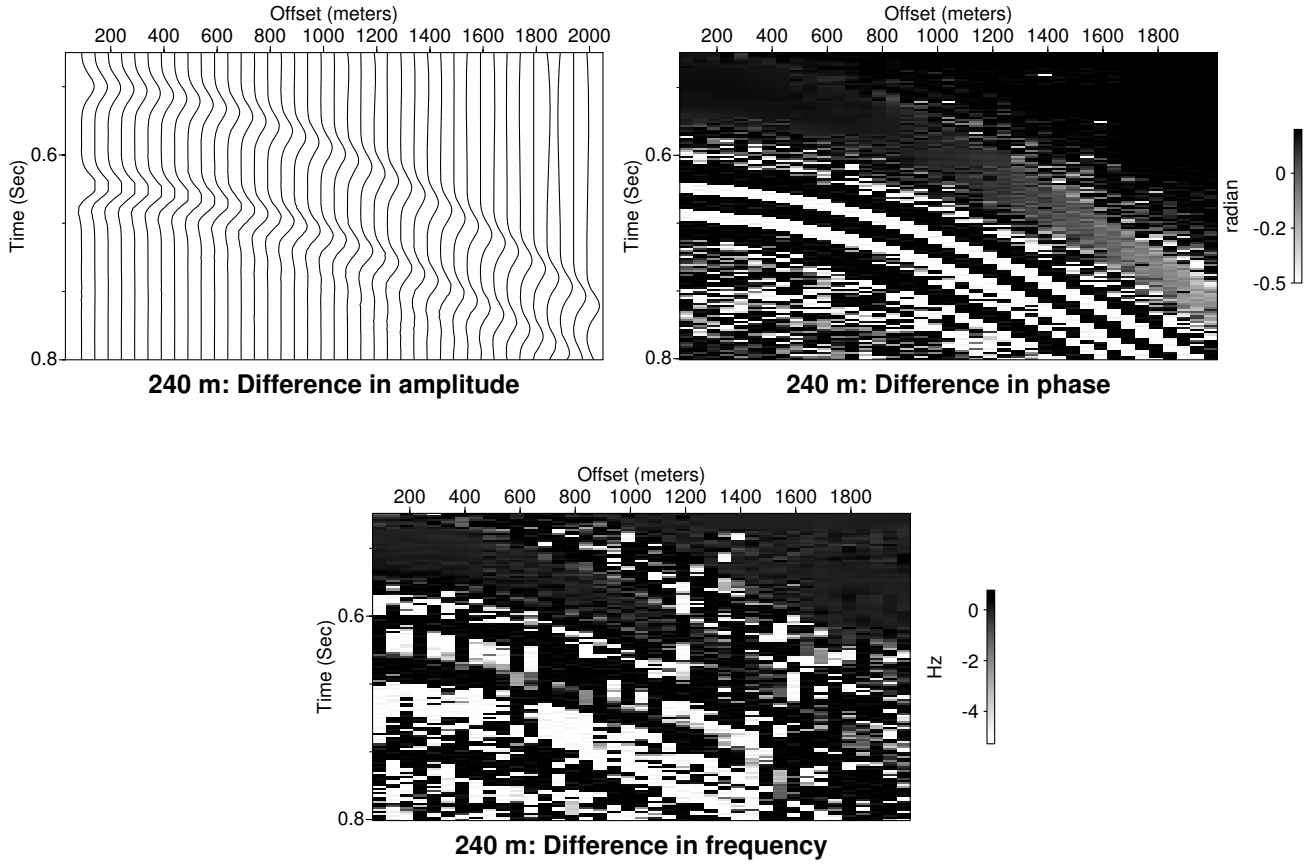

Fig. 2.12. Difference in attributes for brine and SCF CO_2 computed for the 240 m reservoir.

cant difference in amplitude to detect the types of fluid in thin reservoirs. However, Figure 2.12 shows significant difference in both amplitude as well as instantaneous phase (approx.15- 20°) especially from bottom interface to detect types of fluids in the thick fractured attenuating reservoir. In both the cases, the shift in lower frequency shadow indicates the presence of gas and attenuating fractured reservoir.

2.6 Flow Simulation Integration with AVO Attributes

Five-spot pattern was used for flow simulation study with injector at the center and producers at the four corners. Initially reservoir was assumed to be saturated with 80% oil and 20% brine. The reservoir models were tested separately for brine and SCF CO_2 injection. SCF CO_2 was injected at high injection pressure (11 MPa)

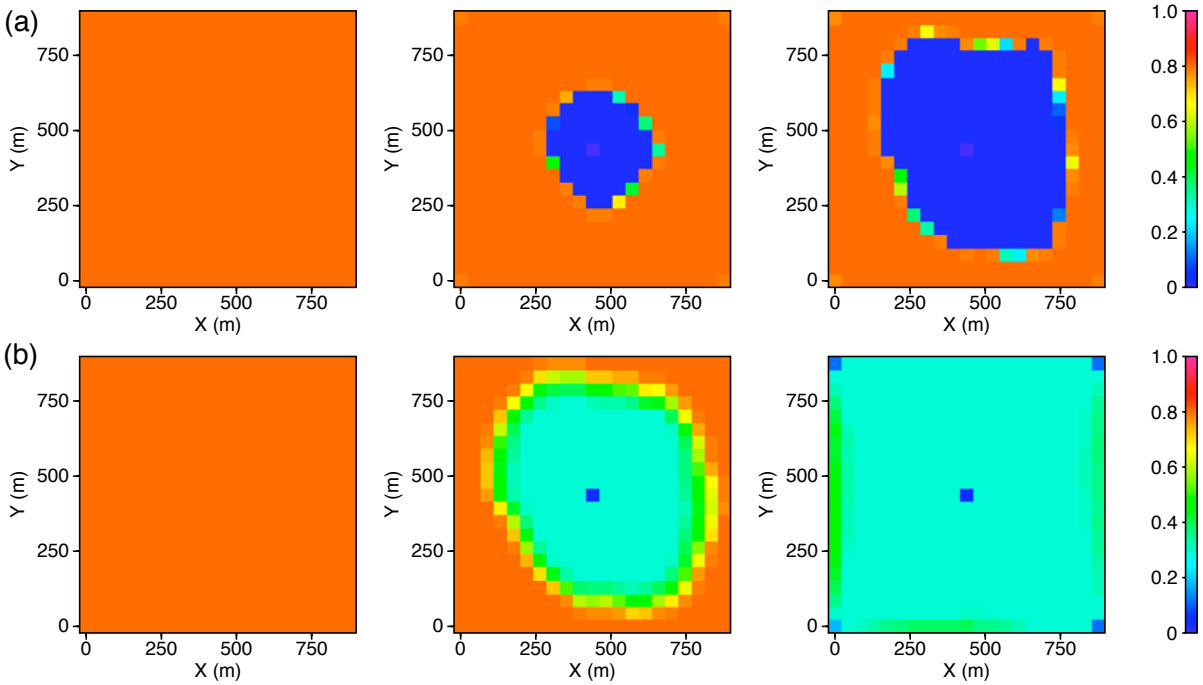

Fig. 2.13. Change in oil saturation during (a) SCF CO_2 injection and (b) brine injection at 0, 800 and 2400 days (left to right, respectively). SCF CO_2 sweeps lower area than brine because of high compressibility of SCF CO_2.

and temperature, having ρ=650 Kg/m^3 and viscosity=7×10^{-5} Pa-s. The time-lapse saturation of oil, gas and brine measured at 0, 800 and 2400 days are shown in Figure 2.13, Figure 2.14 and Figure 2.15 respectively. Because of high compressibility of SCF CO_2, it always shows less flooding than brine.

There were two major objectives of time-lapse study. First, to study the variation in Q_p, V_p and AVO attributes with fluid saturation and second, compare their effect on AVO attributes at different time scale. Figure 2.16 and Figure 2.17 shows time-lapse Q_p and V_p values for different fluids. SCF CO_2 saturated cracks are more compressible than brine saturated cracks causing around 8 times higher attenuation than brine saturated reservoir. These observations are consistent with our numerical analysis for 100% saturated reservoirs where SCF CO_2 saturated reservoirs show 10 times higher attenuation than brine saturated reservoirs. With respect to background medium, SCF CO_2 saturated reservoir shows around 4 times higher attenuation whereas brine shows 50% decrease in attenuation.

Similar study of AVO intercept in Figure 2.18 shows 1.2 times lower intercept for SCF CO_2 saturated reservoirs than brine saturated reservoirs, whereas 1.1 times

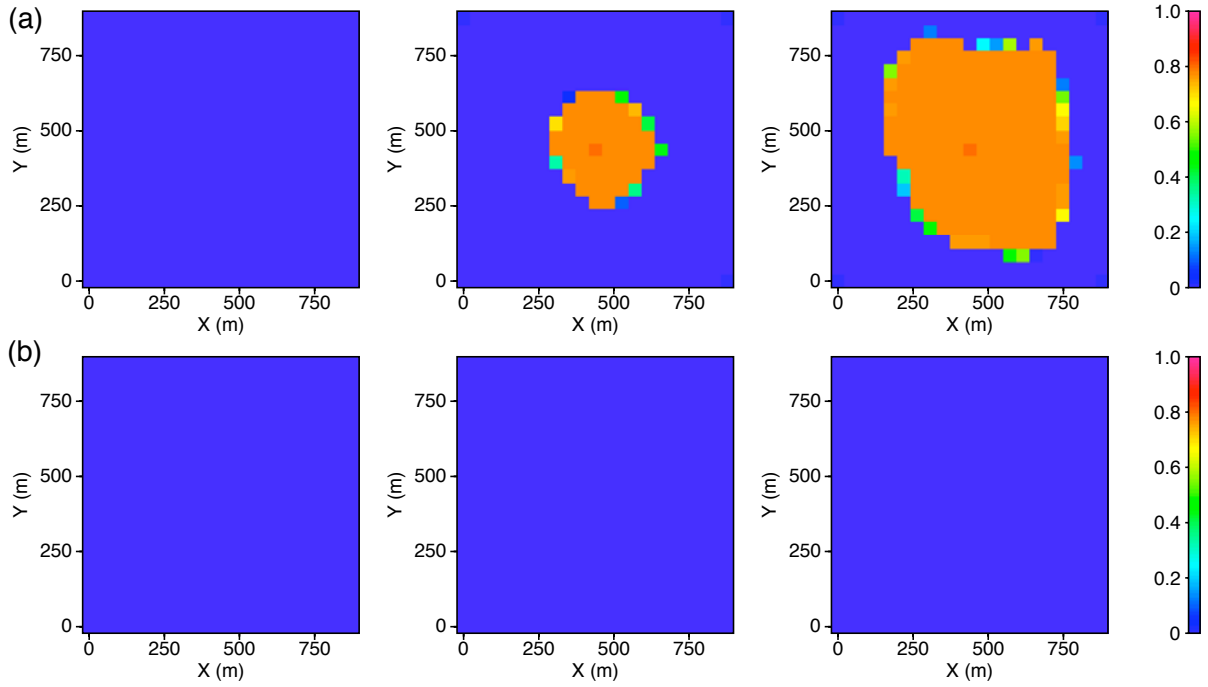

Fig. 2.14. Change in gas saturation during (a) SCF CO_2 injection and (b) brine injection at 0, 800 and 2400 days (left to right, respectively). Brine injection (b) case shows zero gas saturation as initial reservoir model was saturated with oil and brine only.

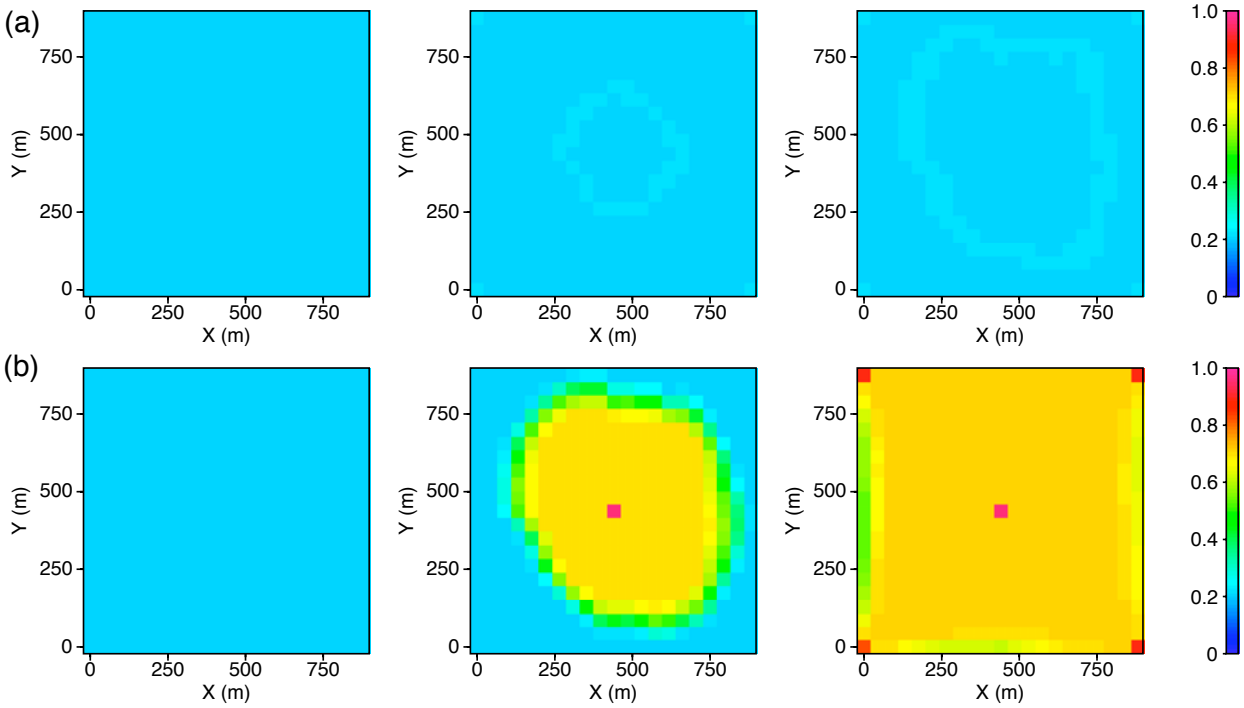

Fig. 2.15. Change in brine saturation during (a) SCF CO_2 injection and (b) brine injection at 0, 800 and 2400 days (left to right, respectively).

higher AVO gradient for SCF CO_2 saturated reservoirs than brine saturated reservoirs (Figure 2.19). With respect to background, SCF CO_2 saturated reservoir shows -10% to -12% AVO intercept change whereas Brine saturated reservoir shows +4% change. These results are also in accord with our numerical analysis for different fluids. These subtle variations in various parameters were further studied using their *difference* plots. Figure 2.20 and Figure 2.21 shows the attenuation and velocity difference between 800 and 2400 days with respect to 0 day. Difference plots show positive value for attenuation and negative values for velocity change for SCF CO_2 saturated reservoir. However, difference plots of attenuation and velocity for brine saturated reservoir shows opposite effect. This is because injection of more and more compressible fluids like SCF CO_2 causes increase in attenuation of seismic waves and decrease in background compressional velocity whereas less compressible fluid like brine injection shows opposite effect. Similar observations can be made for intercept and gradient in Figure 2.22 and Figure 2.23. The scale clearly shows opposite trend of intercept and gradient in different fluids due to compressibilty difference. SCF CO_2 saturated reservoir shows -0.05 to 0.0 whereas brine saturated reservoir shows 0 to

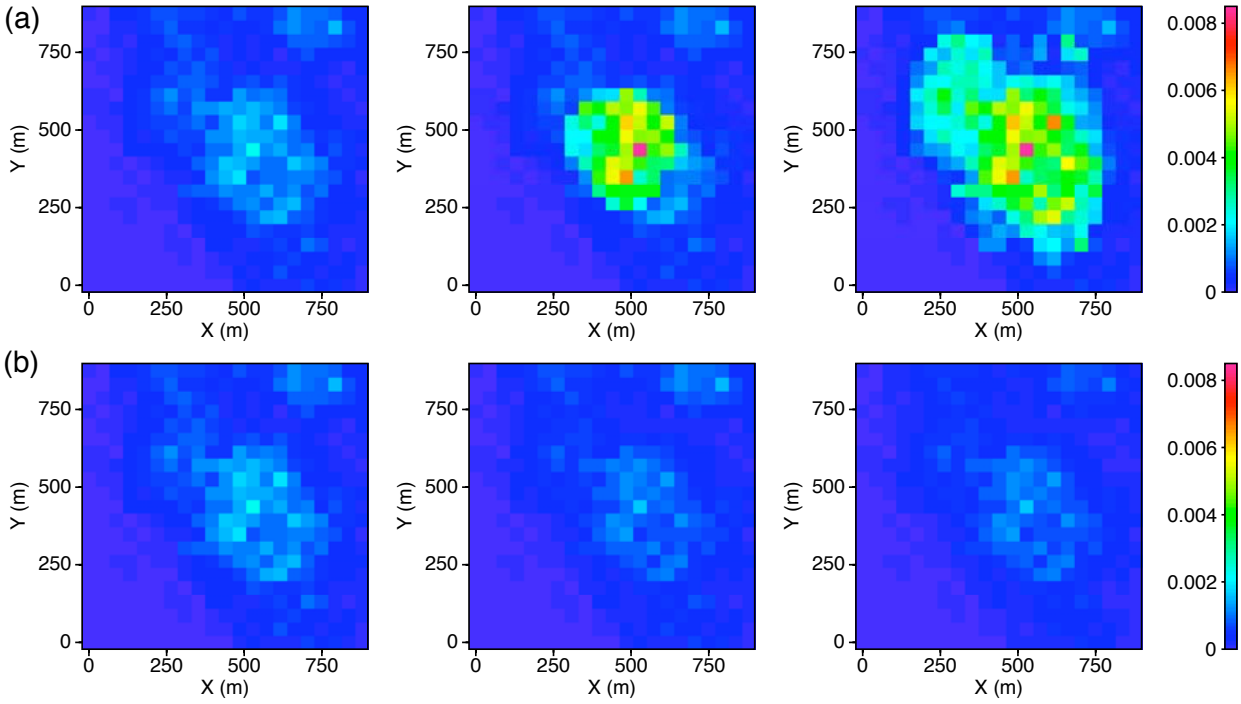

Fig. 2.16. Change in $Q_p{}^{-1}$ during (a) SCF CO_2 injection and (b) brine injection at 0, 800 and 2400 days (left to right, respectively).

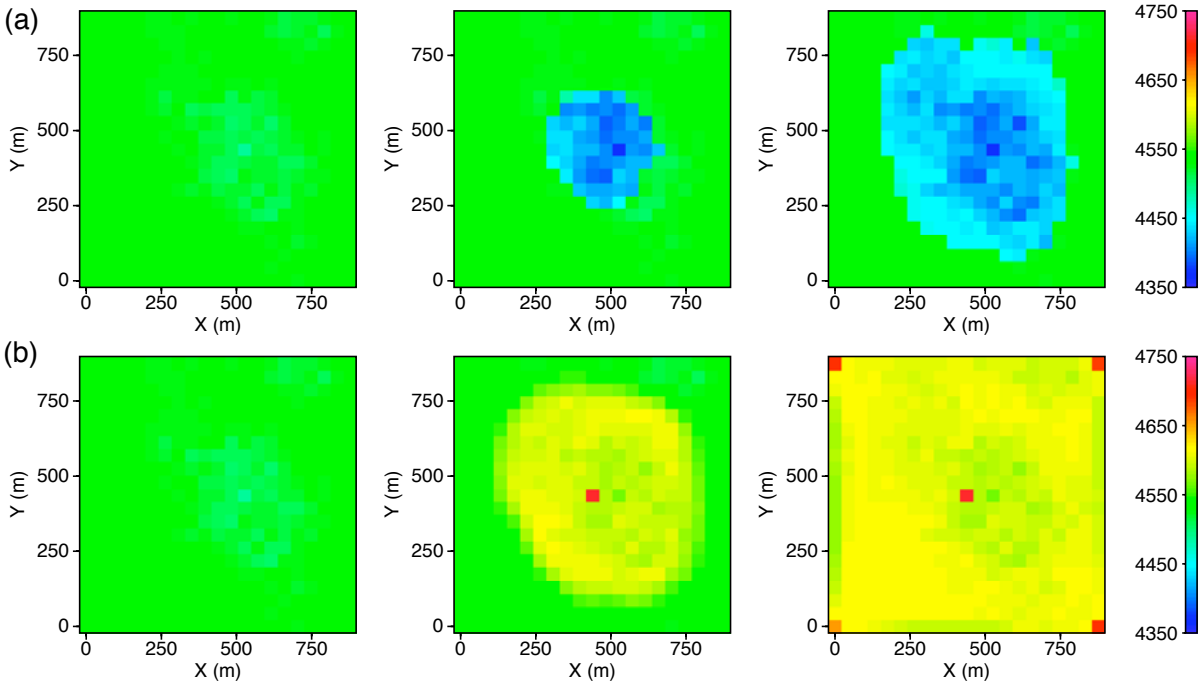

Fig. 2.17. Change in V_p during (a) SCF CO_2 injection and (b) brine injection at 0, 800 and 2400 days (left to right, respectively).

6.0 change in intercept. In order to compare the effect of brine and SCF CO_2 fluids on Q_p, V_p and AVO attributes, their corresponding results were subtracted and are shown in Figure 2.24, Figure 2.25, Figure 2.26, and Figure 2.27. SCF CO_2 saturation zone shows higher attenuation and lower velocity compares to brine saturated zone. The larger intercept and gradient of SCF CO_2 saturated zone compare to brine can be used to segregate types of fluids and their flow regime inside the reservoir.

2.7 Ray-Born Seismic Modeling

Our reservoir modeling study was further analyzed by computing 3D synthetic seismograms using ray-Born algorithm (Beydoun and Mendes, 1989; Gibson et al., 1993). This method estimates wave fields scattered by small perturbations in the properties of an elastic medium. In our study, velocities and density of overburden layers are assumed to be homogenous. Though this assumption is not valid for true earth but still can be acceptable for time-lapse seismic modeling as properties and geology of overburden layers change very little during hydrocarbon production. In our seismic

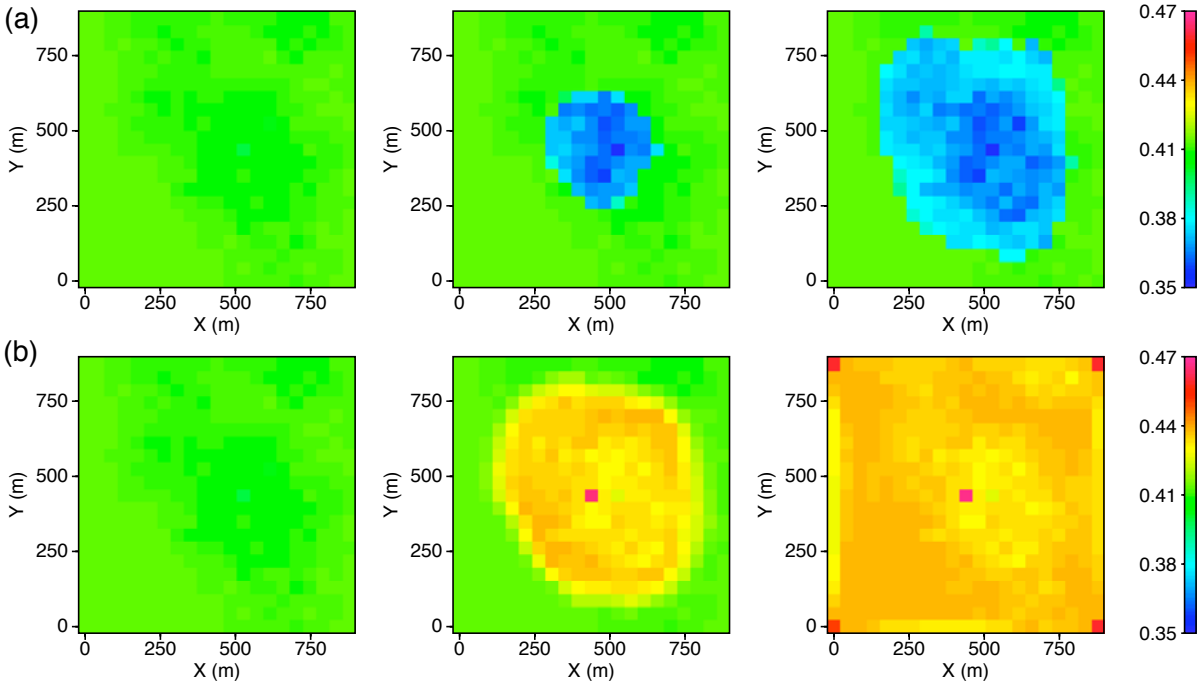

Fig. 2.18. Change in intercept during (a) SCF CO_2 injection and (b) brine injection at 0, 800 and 2400 days (left to right, respectively). SCF CO_2 saturated reservoir shows 1.2 times lower intercept than brine saturated reservoir.

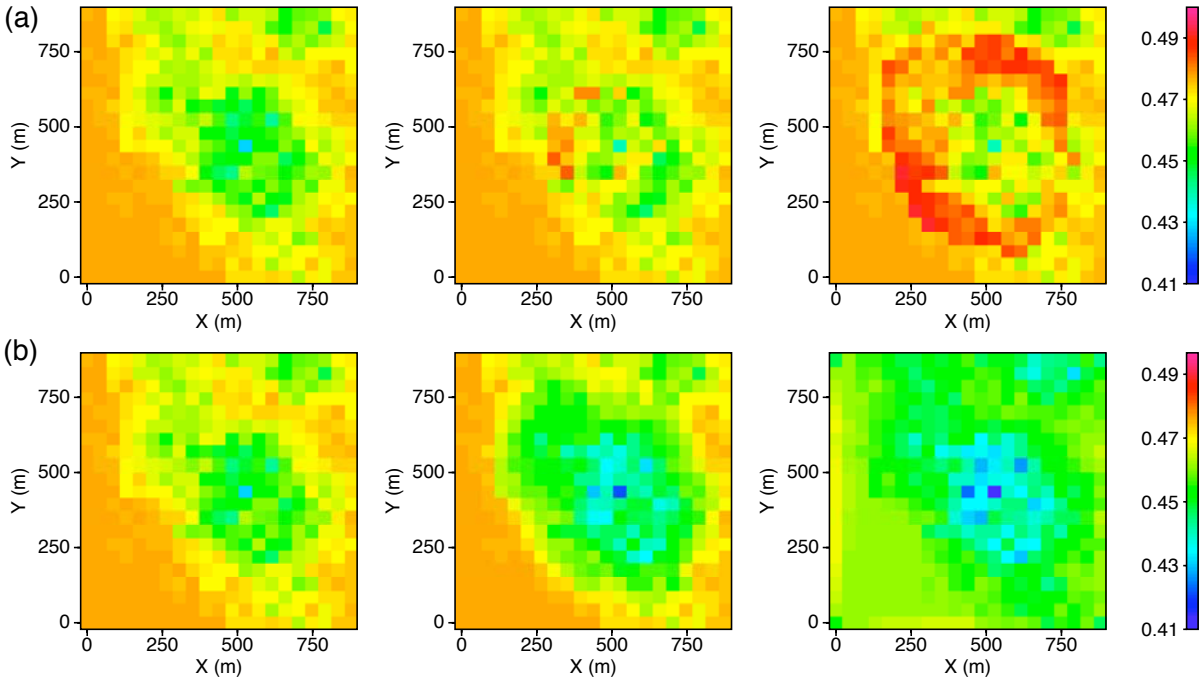

Fig. 2.19. Change in gradient during (a) SCF CO_2 injection and (b) brine injection at 0, 800 and 2400 days (left to right, respectively). SCF CO_2 saturated reservoir shows 1.1 times higher gradient than brine saturated reservoir.

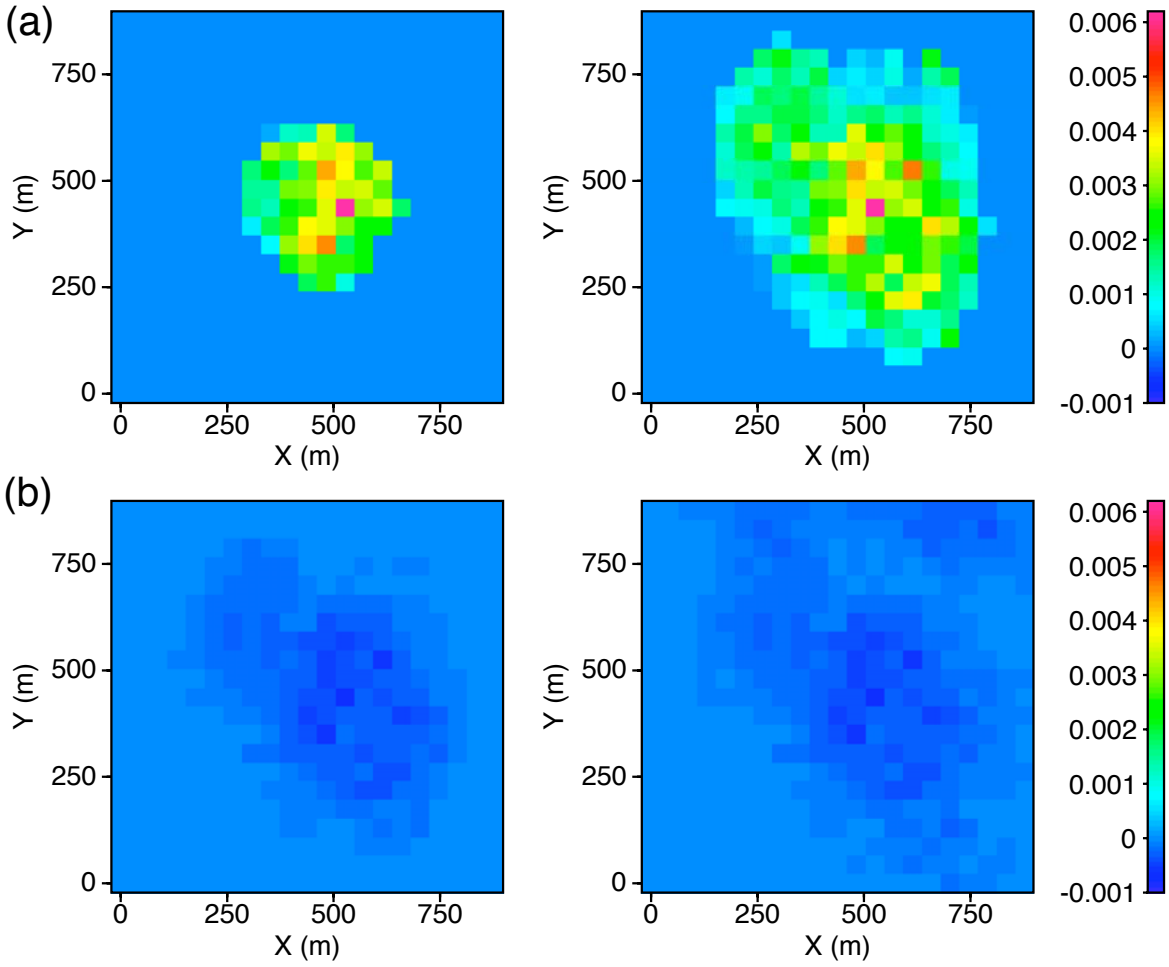

Fig. 2.20. Difference in attenuation during (a) SCF CO_2 injection and (b) brine injection between 800 and 0 day, 2400 and 0 day (left and right, respectively).

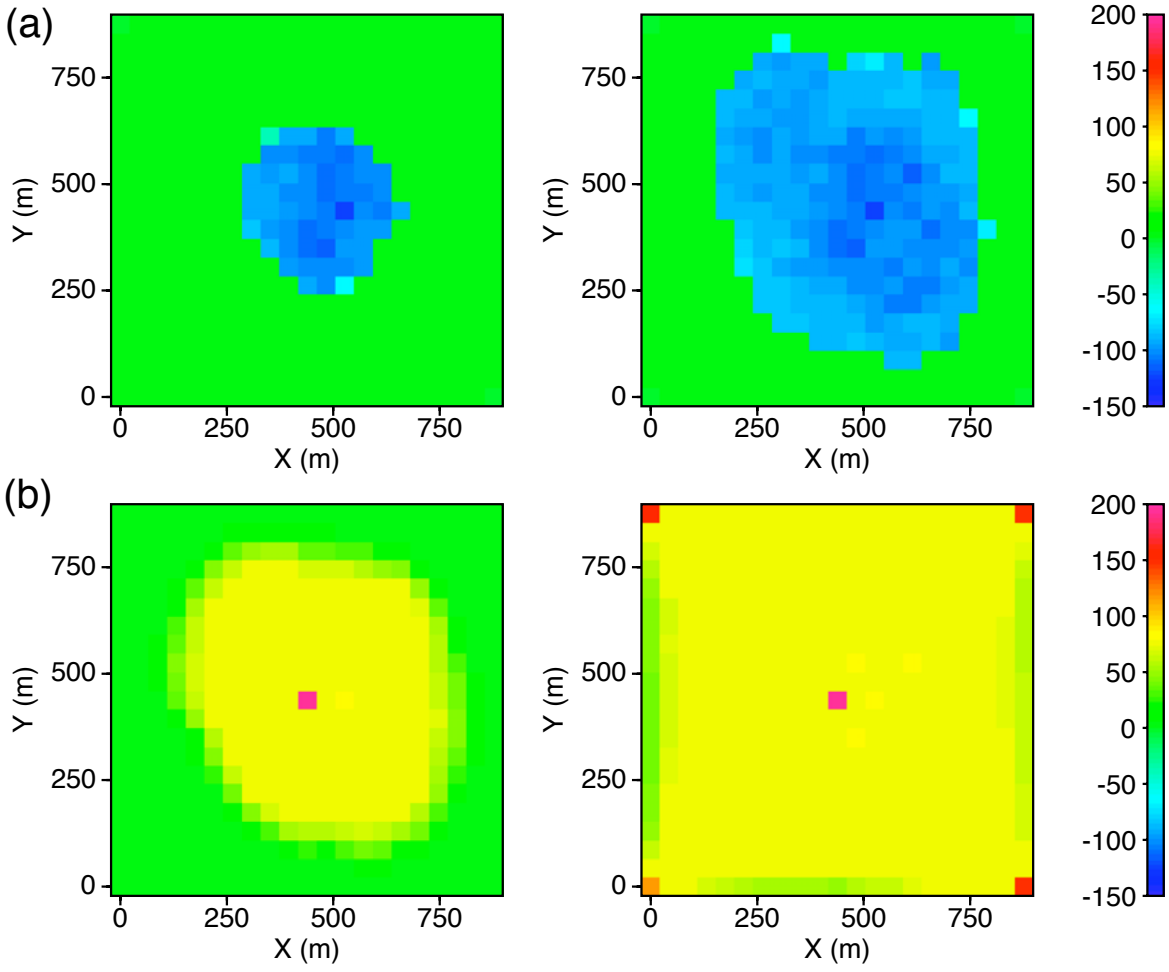

Fig. 2.21. Difference in velocity during (a) SCF CO_2 injection and (b) brine injection between 800 and 0 day, 2400 and 0 day (left and right, respectively).

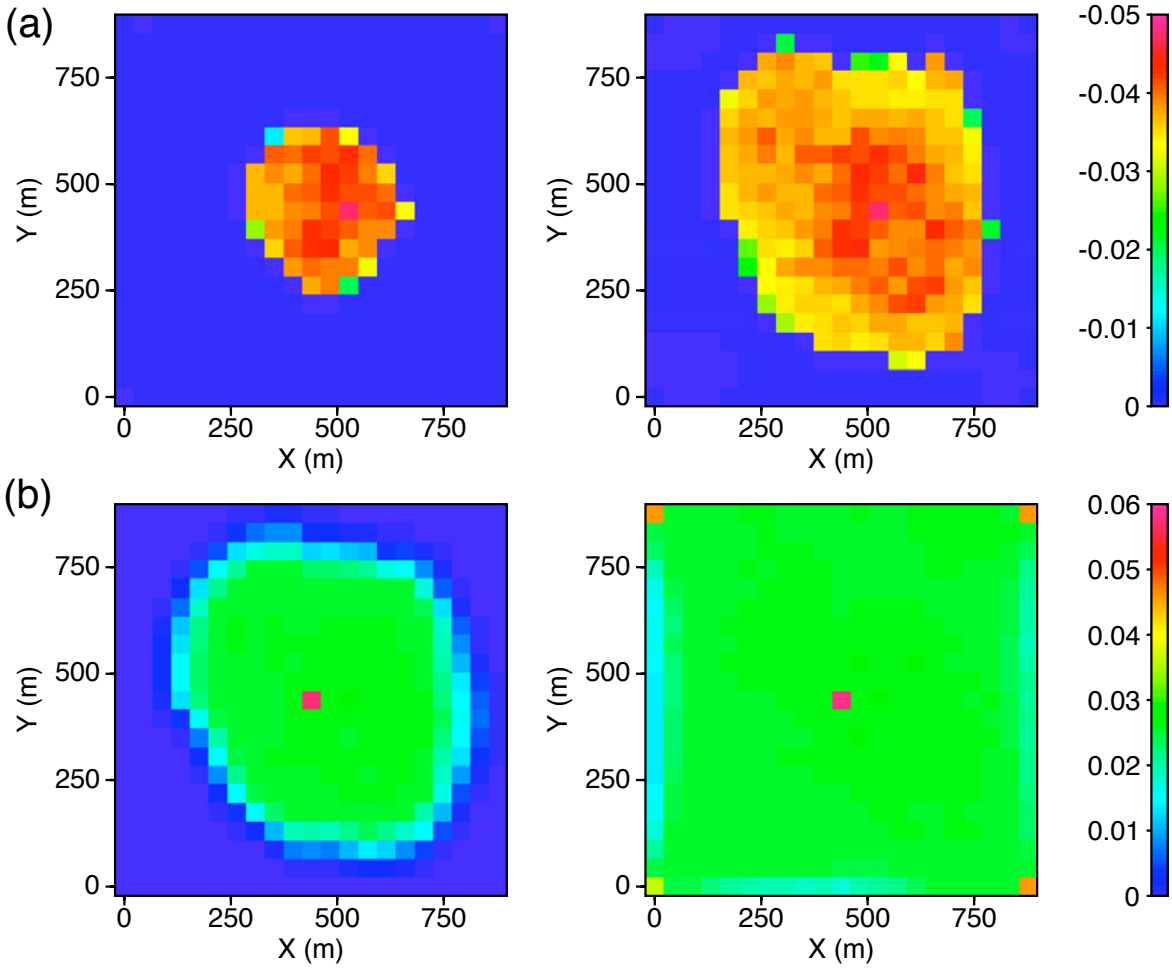

Fig. 2.22. Difference in intercept during (a) SCF CO_2 injection and (b) brine injection between 800 and 0 day, 2400 and 0 day (left and right, respectively).

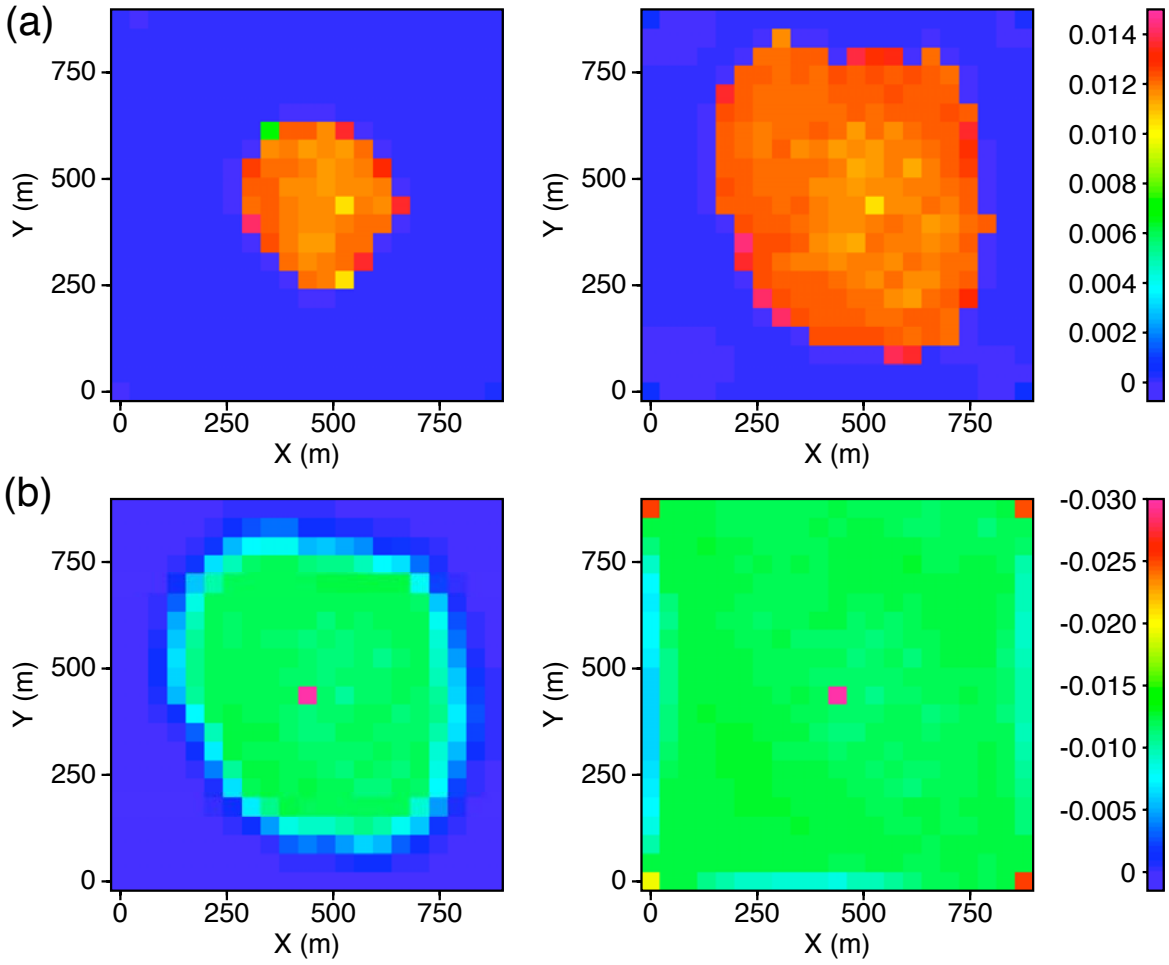

Fig. 2.23. Difference in gradient during (a) SCF CO_2 injection and (b) brine injection between 800 and 0 day, 2400 and 0 day (left and right, respectively).

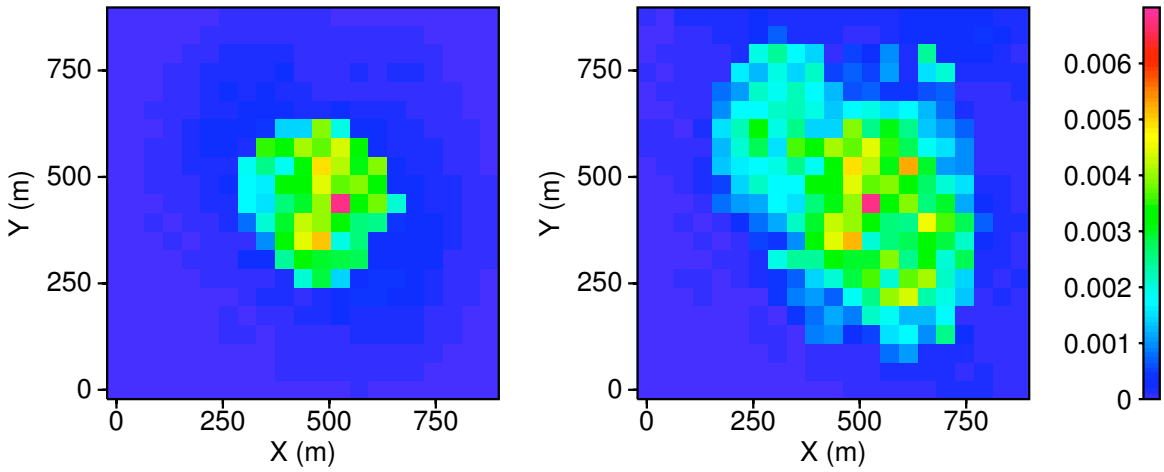

Fig. 2.24. Difference in attenuation between SCF CO_2 injection and brine injection at 800 days and 2400 days (left and right respectively).

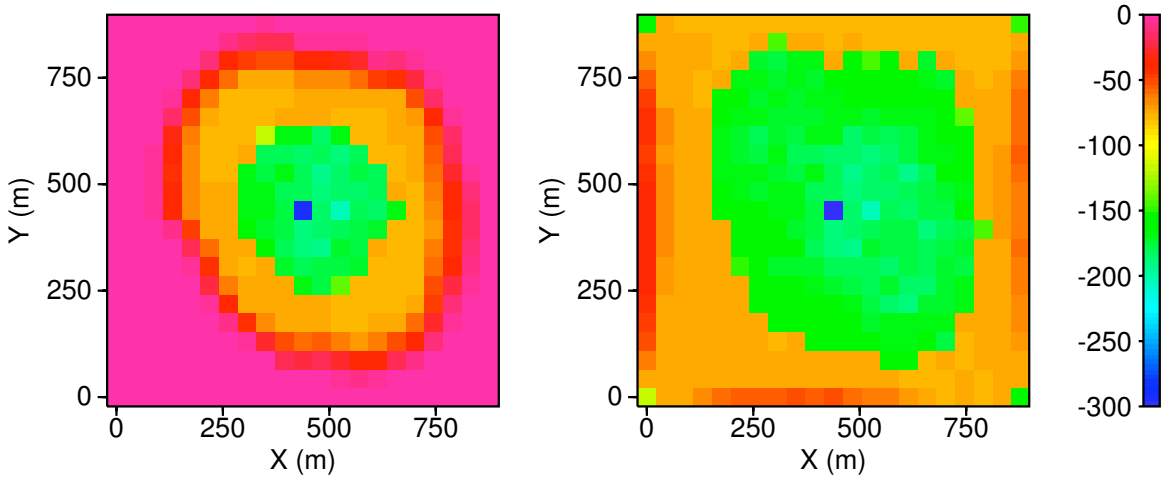

Fig. 2.25. Difference in velocity between SCF CO_2 injection and brine injection at 800 days and 2400 days (left and right respectively).

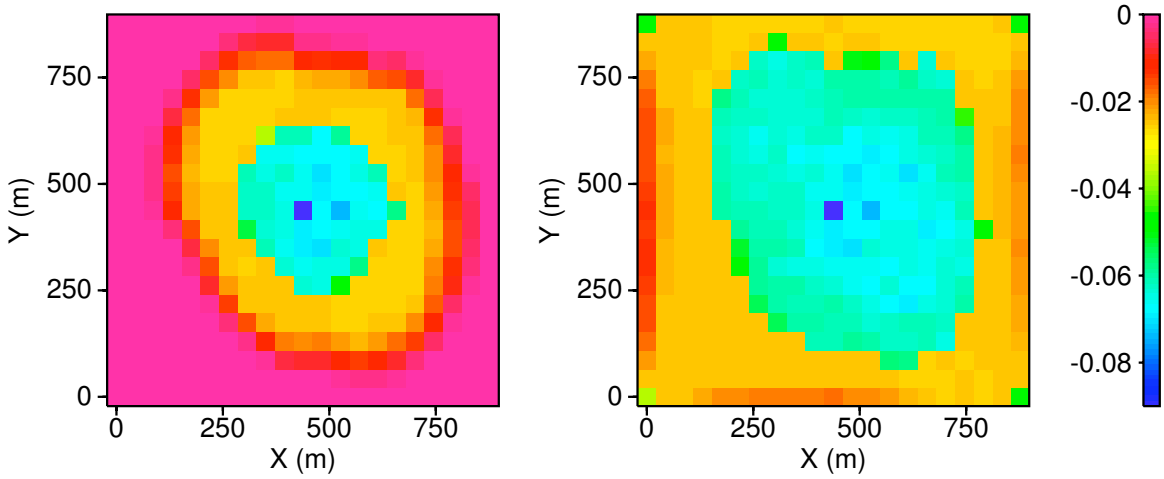

Fig. 2.26. Difference in intercept between SCF CO_2 injection and brine injection at 800 days and 2400 days (left and right, respectively).

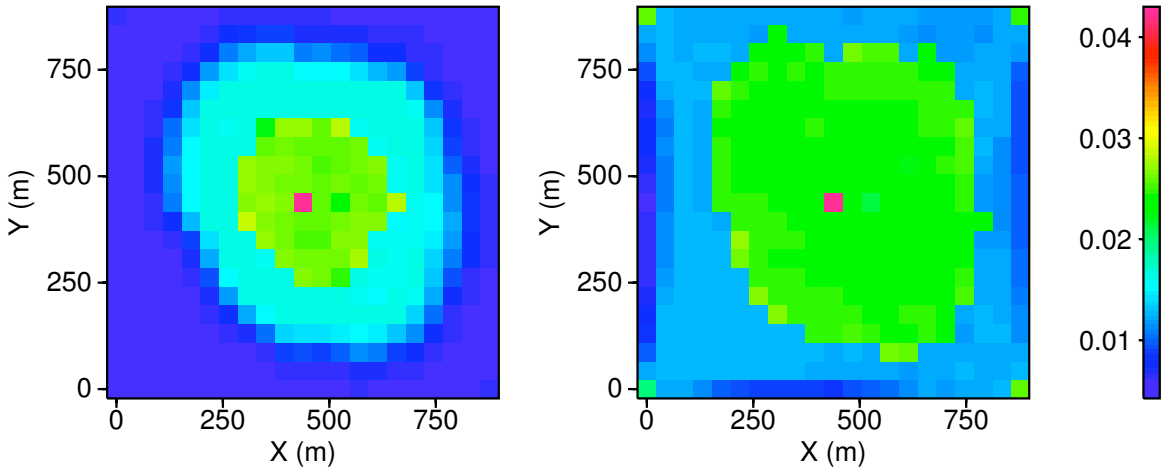

Fig. 2.27. Difference in gradient during (a) SCF CO_2 injection and (b) brine injection between 800 days and 2400 days (left and right, respectively).

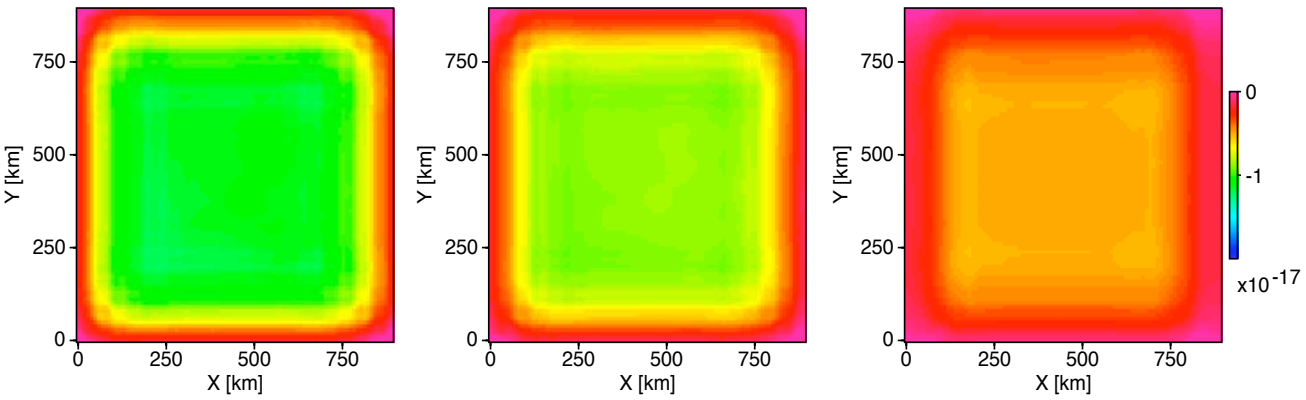

Fig. 2.28. Composite reflection amplitude before any injection from 20 m thin reservoir using ray-Born algorithm at zero, med-offset and far-offset (from left to right respectively).

modeling, there are 90 source-receiver pairs in inline and cross-line direction with 20 m spacing, covering 3D reservoir. We simulated zero-offset, medium offset and far-offset where the medium offset seismic arrays have 598 m source-geophone offset corresponding to 15° incident angle. The far-offset seismic arrays have 1136 m source-geophone offset corresponding to 30° incident angle. We also applied normal move out (NMO) and phase-shift migration to all the seismogram.

The composite reflection amplitude from 20 m thin reservoir before any injection is shown in Figure 2.28. The time-lapse amplitudes after 800 days and 2400 days are computed for zero-offset, medium offset and far-offset as shown in Figure 2.29 and Figure 2.30 The percentage change in relative amplitude after 800 days and 2400 days during injection of brine and CO_2 is shown in Figure 2.31 and Figure 2.32 In accordance with our previous analytical results, Figure 2.31(a) shows injection of SCF CO_2 causes decrease in amplitude from 20% (zero offset) to 45% (far-offset). However, Figure 2.31(b) shows brine injection causes in increase in amplitude from 15% (zero offset) to 25% (far-offset). The large percentage change in amplitude at far-offset becomes very useful in AVO analysis to detect types of fluids present in fractured reservoir.

In order to better understand the effect of injection of different fluids, we extracted one inline through the center of 3D reservoir model. Figure 2.33 compares the effect of different fluids on reflected seismic amplitude. The top of the figure refers to CO_2 injection whereas bottom refers to brine injection. As expected and in

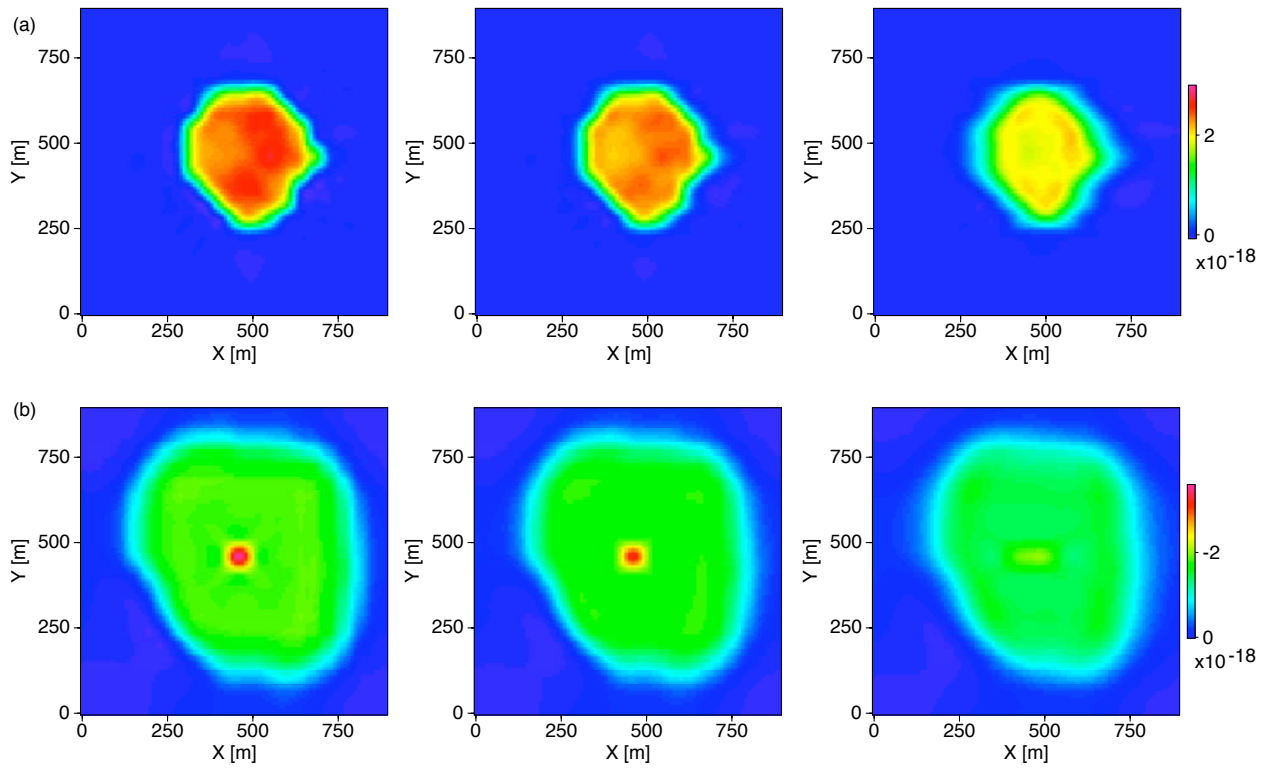

Fig. 2.29. Difference in reflection amplitude during (a) SCF CO_2 injection and (b) brine injection between 800 days and 0 day at zero, med-offset and far-offset (from left to right respectively).

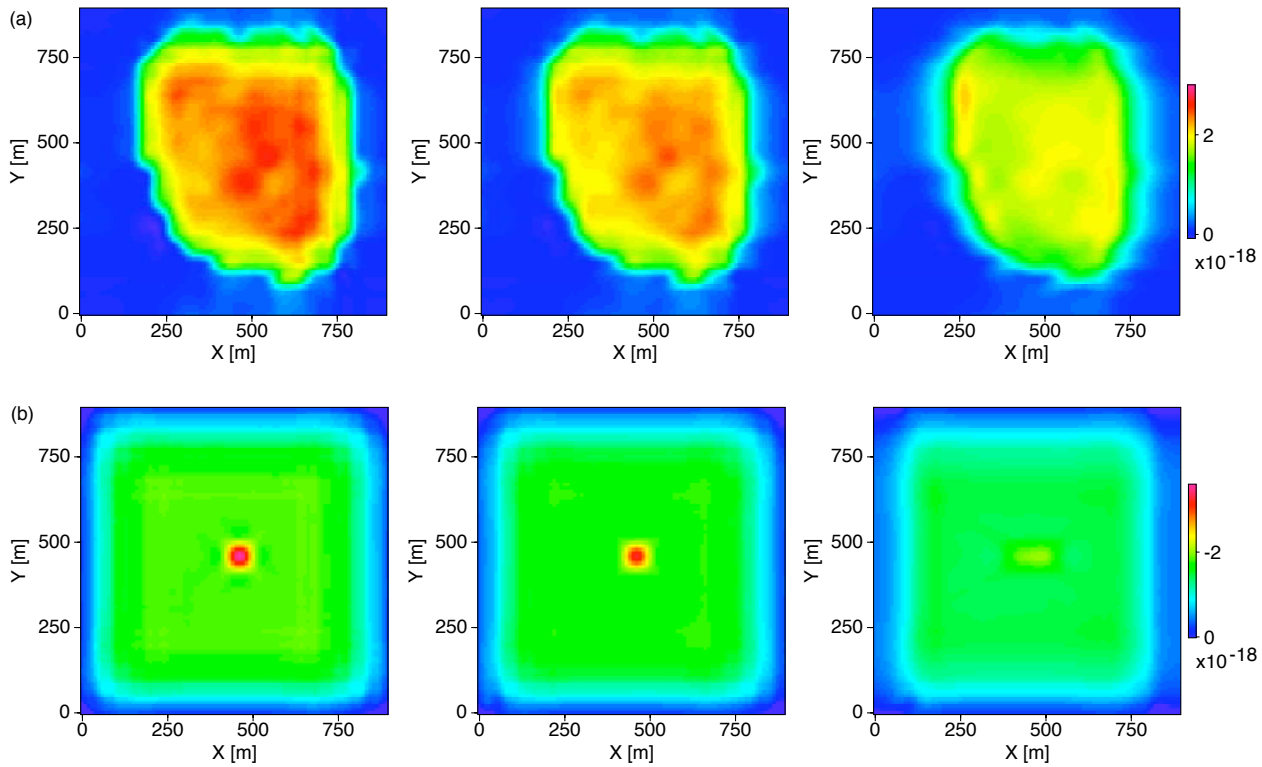

Fig. 2.30. Difference in reflection amplitude during (a) SCF CO_2 injection and (b) brine injection between 2400 days and 0 day at zero, med-offset and far-offset (from left to right respectively).

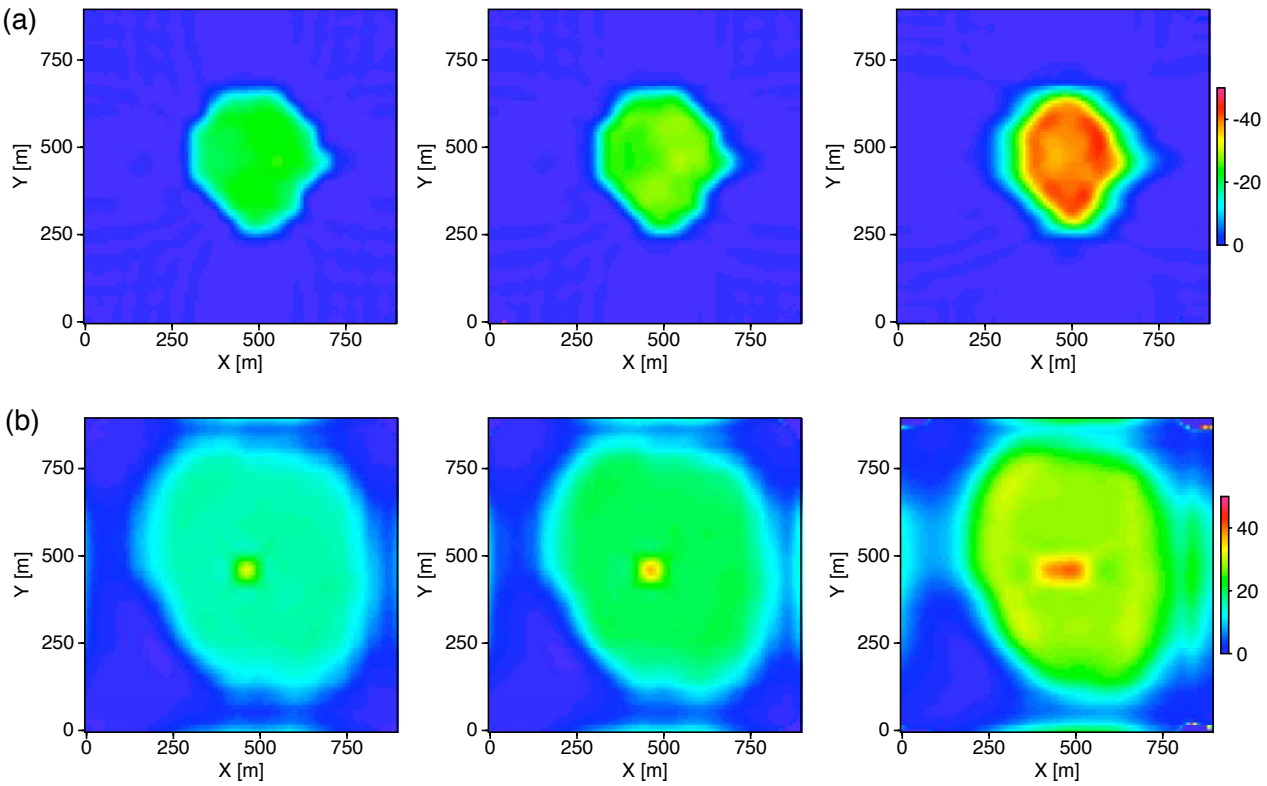

Fig. 2.31. Percentage change in reflection amplitude during (a) SCF CO_2 injection and (b) brine injection after 800 days at zero, med-offset and far-offset (from left to right respectively).

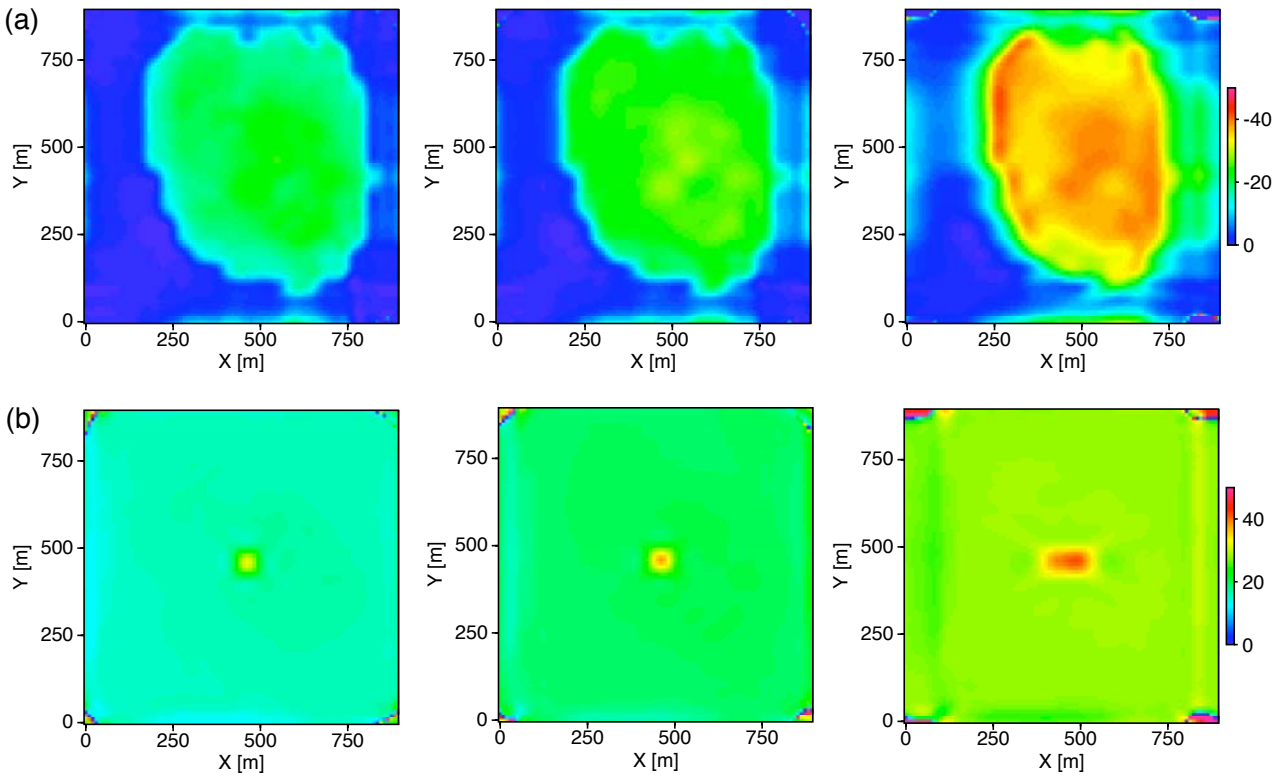

Fig. 2.32. Percentage change in reflection amplitude during (a) SCF CO_2 injection and (b) brine injection after 2400 days at zero, med-offset and far-offset (from left to right respectively).

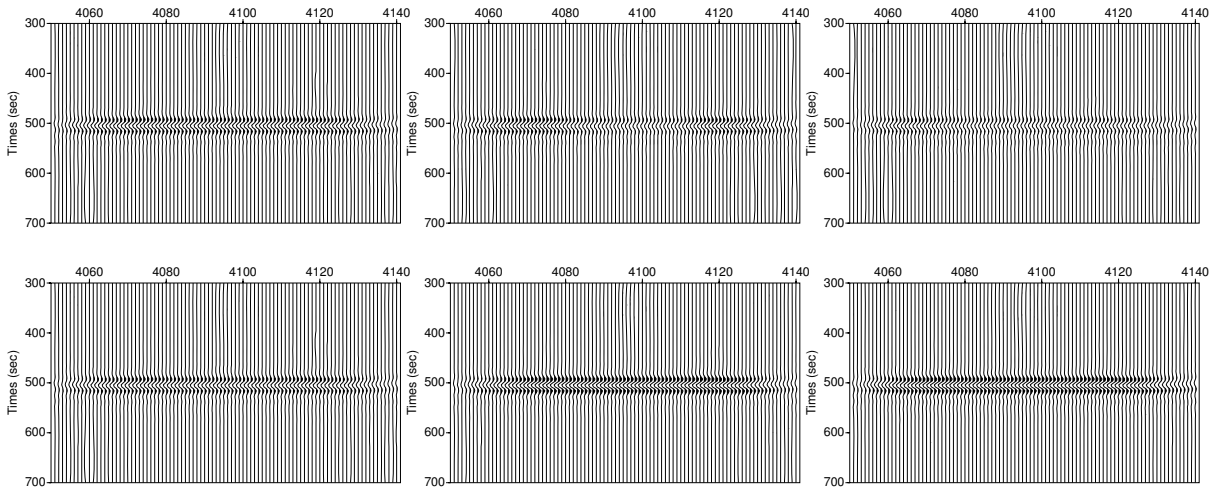

Fig. 2.33. Reflection amplitude (far-offset) at 0, 800, 2400 days (left to right respectively) during SCF CO_2 injection (top) and brine injection (bottom).

accord to our analytical modeling, CO_2 injection causes attenuation or decrease in reflection amplitude whereas brine injection causes increase in reflection amplitude at different offsets. Our further analysis suggests that at far-offset (30° incident angle), CO_2 injection causes 50% reduction in amplitude whereas brine injection cause 50% increase in the amplitude.

2.8 Conclusions

Numerical analysis shows that attenuation and dispersion of seismic waves strongly depend on crack size and permeability of host rock in the equant porosity model. We have developed methods for relating discrete fracture network models used by engineers to set up fluid flow simulations to models of crack density that can be used to predict seismic reflections from the fractured reservoir. This is an important first step in developing integrated tools for fractured reservoir characterization. AVO results for our example model predict that supercritical carbon dioxide is easier to detect than brine in the fractured reservoirs. The total modeling process is fast and comparatively simple, leading to a prediction of AVO results for comparison to field measurements. Our time-lapse study integrating flow simulation suggest significant, but not sure if measurable on seismic data, change in Q_p, V_p and AVO attributes with change in saturation. The 10% to 12% decrease of intercept with respect to background for SCF CO_2 saturated reservoir shows as potential attribute for detecting fluids in reservoirs. Also, the opposite trend of *differences* of various parameters can be useful in detecting the type of fluids present in the reservoir. Also, other methods such as instantaneous attributes study suggest Q can be affected even by thin layers and can distinguish fluids in thin and thick reservoirs. Our seismic modeling using ray-Born algorithm suggest significant relative change in amplitude at far-offset that can be useful for AVO analysis. We anticipate that this general procedure will have some important applications for reservoir monitoring studies.

CHAPTER III

SEISMIC MODELING OF COMPOSITIONAL AND GEOCHEMICAL EFFECTS IN CO_2 SEQUESTRATION

3.1 Introduction

Carbon dioxide sequestration is a viable approach for controlling the effects of greenhouse gases on global warming (Bachu, 2003). Sequestration is the process of storage of CO_2 into repositories such that it remains stored for long and doesn't release to the atmosphere. The good candidate geological formations for sequestration sites are depleted oil and gas reservoirs, unmineable coal seams, saline formations, shale and basalt formations. The motivation to use basalt formation is because of unique chemical properties of basalt that converts all injected CO_2 to a solid mineral form thus permanently storing into the formations (Energy, 2008). However, the most mature and effective technology still available for directly minimizing emissions is sequestration in existing or depleted hydrocarbon reservoirs (Hepple and Benson, 2005). Existing and depleted oil and gas reservoirs for CO_2 sequestration are more in demand compare to other formations because of two principal reasons. First, the economic benefits associated with enhanced oil and gas recovery are commercially proven and widely accepted by the industry. Second, oil and gas reservoirs provide abundance data sources such as porosity, permeability, seismic velocity etc. that can be used to design the sequestration sites. Challenges do remain, however, in the modeling, design and implementation of long time sequestration projects.

One of the major concerns in sequestration projects is the low density and viscosity of CO_2 under subsurface conditions, which may significantly increase the risk of its leakage from the sequestration site into overlying rock (Tsang et al., 2002). Furthermore, CO_2 interacts chemically with the host rock, potentially causing difficulties in understanding and predicting its behavior during sequestration. Leakage of CO_2 can lead to several other problems such as acidification of ground water. The development of adequate policies to govern sequestration therefore requires improved characterization of the media in which CO_2 is stored and the development of advanced methods for detecting its flow and movement. Existing laboratory data and

field experiments both suggest that the influence of CO_2 on seismic properties is sufficiently strong to be detectable at a given point in time. The injected CO_2 can exist in three separate phases, viz. supercritical fluid CO_2, gaseous CO_2 or dissolved in aqueous solutions, depending on the pore pressures and temperatures in the reservoir (Wang et al., 1998). Measurements on core samples have shown that the CO_2 can decrease the velocity of both compressional and shear waves by up to 10% (Wang et al., 1998). Crosswell experiments show that it can be detected successfully in the field (Harris et al., 1995). These results show that it should be possible to image the distribution of CO_2 injected into a formation because of the immediate changes in bulk fluid properties. However, the seismic response may also change because of geochemically influenced processes such as cementation, secondary porosity formation or compaction, and these are especially important for long-term sequestration efforts. In particular, when carbon-dioxide encounters formation brine, it forms carbonic acid, which reacts with the formation minerals and alters rock composition as well as brine salinity.

Therefore, this chapter presents results of detailed geochemical simulations combining fluid flow models with composition modeling that incorporates these phenomena. Our modeling study considers carbonate rich limestone rock, an end member of metacarbonates series, which is one of the most common reservoir rocks. The solutions provide a prediction of how important geochemical reactions might be for seismic monitoring of CO_2 sequestration. Below we first summarize the simulation of fluid flow, geochemical and seismic responses and then present results for changes in seismic reflection response. The results show that the chemical processes cause relatively small changes in seismic amplitudes after 1000 years, suggesting that reduction in the bulk modulus of the fluid by mixing of CO_2 with brine and oil will still cause the most significant changes in amplitude.

3.2 Geochemical Modeling

The two major components of the model study are compositional and geochemical modeling of fluid flow and the prediction of time-lapse seismic signals. We used the GEM simulator for the geochemical and composition modeling of CO_2 injection and subsequent fluid flow (Nghiem, 2002; Nghiem, 2003). GEM is a compositional simulator that incorporates phase and chemical equilibrium models and rate dependent

Table 3.1. Aqueous species and their initial concentrations

Species Name	**Initial Molality (Moles/Kg of Water)**
H^+	1E-07
Ca^{++}	9.118492E-05
Al^{+++}	2.317806E-11
SiO_2	2.345433E-08
Na^+	0.5
Cl^-	0.52
HCO_3^-	2.489299E-02
CO_3^{--}	1.170273E-05
OH^-	5.456322E-07

mineral dissolution and precipitation reactions.

The geochemical reactions taking place during sequestration alter rock composition and brine salinity, thus affecting the density and bulk modulus of reservoir rock and fluids. For example, CO_2 injection into the formation leads to the formation of carbonic acid, which in turn triggers other reactions (Stumn and Morgan, 1996). Our simulations considered the brine species in Table 3.1, minerals in Table 3.2 and we selected to include the set of reactions in Table 3.3, which model the basic dynamics of the chemical transformations during CO_2 injection. All of the brine species are actively involved in these reactions. The relative phase behavior of CO_2 and reservoir fluids controls the dissolution of CO_2 that affects different geochemical reactions. For chemical modeling, phase equilibria are calculated using the Peng-Robinson equation of state and the gas-brine equilibria (Li and Nghiem, 1986). Dissolution was assumed to be instantaneous, and the gas and aqueous phases are considered to be in thermodynamic equilibrium at which the fugacities of the gaseous and aqueous phases are

Table 3.2. Minerals and their initial volume fractions

Mineral	**Chemical Formula**	**Molecular Weight**	**Density** (**kg**/m^3)	**Initia Volume Fraction**
Calcite	$CaCO_3$	100.0869	2710	97
Kaolinite	$Al_2Si_2O_5(OH)_4$	258.1616	2410	0.0176
Anorthite	$CaAl_2Si_2O_8$	278.2082	2740	0.0088

Table 3.3. Geochemical reactions

Intra-aqueous reactions
CO_2 (aq)+ H_2O = H^++ $HCO_3{}^-$
$HCO_3{}^-$ = H^++ $CO_3{}^{--}$
H^++ OH^- = H_2O
Mineral equilibrium reactions
Calcite + H^+ = Ca^{++}+ $HCO_3{}^-$
Kaolinite + $6H^+$ = $5H_2O$ + $2Al^{+++}$ + $2SiO_2$ (aq)
Anorthite + $8H^+$ = $4H_2O$ + Ca^{++}+ $2Al^{+++}$ + $2SiO_2$ (aq)

equal as shown below,

$$f_{ig} - f_{iw} = 0, \qquad i = 1, 2, ..., n_g \tag{3.1}$$

where n_g is the total number of components in the gas phase, f_{ig} and f_{iw} represents the fugacities of component i in the gaseous and aqueous phase respectively. The Peng-Robinson equation of state is used to compute the fugacities of gas phase and Henry's law is used to compute the fugacities of the components in the aqueous phase as given below,

$$f_{iw} = y_{iw} H_i \tag{3.2}$$

where H_i is the Henrys law constant for component i and is a function of salinity (**?**).

The geochemical reactions include both fast intra-aqueous or slow mineral reactions, and the GEM simulator models intra-aqueous reactions (Table 3.3), such as the formation of carbonic acid, using chemical equilibrium conditions that require the forward and backward reaction rates to be same.In GEM, these reactions are modeled using the following equality conditions (Nghiem, 2002; Nghiem, 2003).

$$Q^a_\alpha - K^a_{eq,\alpha} = 0, \qquad \alpha = 1, ...R_{aq} \tag{3.3}$$

where Q^a_α is the activity product for the intra-aqueous reaction α given by,

$$Q^a_\alpha = \prod_{k=1}^{n_s} a_k^{\nu^a_{k\alpha}}, \qquad \alpha = 1, ...R_{aq} \tag{3.4}$$

where a_k is the activity coefficient for component k and R_{aq} is the number of aqueous reactions. Also, $K^a_{eq,\alpha}$ is the chemical equilibrium constant for the intra- aqueous reaction α and is given as follows,

$$K^a_{eq,\alpha} = exp[-\frac{1}{RT}\sum_{k=1}^{n_s} \nu^a_{k\alpha}(\Delta G^\circ_f)_k], \qquad \alpha = 1, ...R_{aq} \tag{3.5}$$

where R is the Gas constant, T is the temperature, and ΔG° is the standard-state Gibbs energy. Aqueous solutions are considered ideal, hence their activity coefficients are considered to be equal to their molalities (moles/kg of water). The activity coefficient for water and minerals are taken to be unity. The chemical equilibrium constants are modeled as fourth order polynomial of temperature whose coefficients

were taken from (Nghiem, 2003; Stumn and Morgan, 1996).

The mineral reactions (Table 3.3), which are typically slower than intra-aqueous reactions, are modeled as rate-dependent reactions based on their distance from equilibrium (Nghiem, 2002),

$$r_\beta = \hat{A}_\beta k_\beta \Big[1 - (\frac{Q_\beta}{K_{eq,\beta}})\Big] \tag{3.6}$$

where $\hat{A}_\beta$ is reactive surface area of mineral reaction β per unit bulk volume of porous medium, k_β is the rate constant of the mineral reaction, Q_β is the activity product of mineral dissolution/ precipitation reaction, $K_{eq,\beta}$ is the chemical equilibrium constant of mineral dissolution/precipitation reaction. Whether precipitation or dissolution takes places depends upon the activity product of associated mineral dissolution and precipitation reactions. These reactions significantly affect reservoir properties, especially porosity and permeability. In GEM, the porosity change is computed from changes in the reactive surface area from the relationship (Nghiem, 2002; Nghiem, 2003)

$$\frac{d\phi}{dt} = -\sum_{k=1}^{n_m} N_k 4\pi {r_k}^2 \frac{dr_k}{dt}, \tag{3.7}$$

where ϕ is the porosity, r_k is the mean grain size of the mineral, N_k is the number of mineral grains per unit volume, and r_k is the rate of dissolution of mineral k. Results show that porosity changes in our model are negligible, however. The more detail of geochemical modeling is discussed in Kumar et al. (2008).

3.3 Models for Time-Lapse Seismic Monitoring of CO_2

Seismic data have the potential to provide valuable insights into the success or failure of a CO_2 sequestration project. Previous experiments show the feasibility of detecting the motion of CO_2 in the subsurface (Harris et al., 1995; Nolen-Hoeksema et al., 1995), which will be very important for ensuring that leakage from the storage site is not taking place. However, the feasibility of long term storage is a more complex issue, because most studies are based on short term field efforts where chemical processes are likely of minimal importance. In this study, we therefore use conventional models, combined with the fluid flow and geochemical simulations, to demonstrate the potential of seismic data to monitor changes in a sequestration site over periods

as long as hundreds of years.

This simulation requires models for the changes in seismic properties that are caused by changes in fluid properties and chemical effects. Here we summarize the models used to predict changes in seismic velocity and formation density caused by changes in fluid properties and by changes in formation properties caused by chemical processes. These provide the essential parameters for simulating the seismic response of the reservoir. This response could be determined using a full simulation of seismic wave propagation, generating synthetic seismograms that would be processed for interpretation applications. In our case, we are primarily interested in applying amplitude variation with offset (AVO) processing, which is based on measurements of the change in seismic reflection amplitudes with angle of incidence, which is equivalent to changes in the offset between source and receiver in a common midpoint gather. Conventional processing fits a line to the amplitude measured as a function of the squared sine of the angle of incidence, reducing a large number of observations to a pair of seismic attributes, the intercept and slope, or gradient, of the line. Simple analytic solutions are available to compute these two attributes for a homogeneous reservoir, and they provide a much faster solution than trying to directly simulate the seismograms and process them for the equivalent results. We therefore outline the basic features of the solutions as well as the models for rock and reservoir properties.

3.3.1 Seismic Rock Properties

The amplitude of seismic waves reflecting from a formation containing CO_2 or another fluid will depend on the properties of both the fluid itself and of the porous rock matrix. Specifically, seismic compressional and shear wave velocities will change as fluid properties vary, and a common model describing these variations is the Gassmann equation (Gassmann, 1951). This solution assumes isostress conditions for an isotropic, homogenous, monominerallic rock at the low frequency limit. While the shear modulus μ of the rock is predicted to remain constant by this theory, the bulk modulus of the saturated rock depends on several properties of the fluid and solid components:

$$\kappa_{sat} = \kappa_{dry} + \frac{(1 - \frac{\kappa_{dry}}{\kappa_s})^2}{\phi(\frac{1}{\kappa_f} - \frac{1}{\kappa_s}) + \frac{1}{\kappa_s}(1 - \frac{\kappa_{dry}}{\kappa_s})}. \tag{3.8}$$

Here κ_{dry} is the bulk modulus of the drained rock sample, κ_s is the mineral grain bulk modulus, κ_f is the fluid bulk modulus, and ϕ is the porosity.

In most cases, the formation will be partially saturated with brine, oil and another fluid such as CO_2 . In our models, we can have all three fluids present and the bulk modulus of the mixture is given by Woods equation (Mavko et al., 2003) as

$$\frac{1}{\kappa_f} = \frac{S_1}{\kappa_1} + \frac{1 - S_1}{\kappa_2}, \tag{3.9}$$

where κ_i is the bulk modulus of fluid i, S_i is the saturation of that fluid. This is easily extended to three fluids. The bulk density of the formation is simply the volume average of the density of each component present in the fluid-saturated rock.

$$\begin{aligned} \rho_{bulk} &= (1-\phi)\rho_{matrix} + \phi(\rho_{CO_2} S_{CO_2} + \\ &\quad \rho_{oil} S_{oil} + \rho_{water}(1 - S_{CO_2} - S_{oil})) \end{aligned} \tag{3.10}$$

Using bulk and shear moduli and the density of the CO_2 bearing formation, the compressional and shear wave velocities can be calculated.

$$V_p = \sqrt{\frac{\kappa + \frac{4}{3}\mu}{\rho}} \tag{3.11}$$

$$V_s = \sqrt{\frac{\mu}{\rho}} \tag{3.12}$$

The S-wave velocity is comparatively weakly dependent on the fluid properties, because only density changes affect it. However, the change in the P-wave velocity is more significant because of its dependence on the bulk modulus.

In a general case, seismic properties will change with pore pressure as well. However, in our simulations the changes in pore pressure are comparatively small, on the order of several MPa, especially after CO_2 injection stops. Test calculations show that pressure effects cause much smaller changes in seismic velocity than saturation and other effects, so we ignore them in this study.

3.3.2 Acoustic Properties of Reservoir Fluids

While the Gassmann and Woods equations provide models for changes in seismic properties with changes in fluid saturations, integration of seismic and fluid flow

simulations also requires relationships to quantify the effects of changing temperature, salinity and pore pressure. The density of brine, which depends upon salinity, pore-pressure and temperature, was taken directly from the simulation results, but the P-wave velocity changes for the relevant fluids require additional models. Here we summarize the models used for the fluids of interest, viz. brine, oil and supercritical fluid CO_2.

Brine: Batzle and Wang et.al (1992) provide empirical realationships for changes in brine P- wave velocity as

$$\begin{aligned} V_p &= V_w + S(11709.6T + 0.055T^2 - 8.5 \times 10^{-5}T^3 \\ &+2.6P - 0.0029TP - 0.0476P^2 + S^{1.5}(78010P \\ &+0.16P^2)1820S^2 \end{aligned} \tag{3.13}$$

Here pressure P is in MPa, temperature T is in degree Celsius, salinity S is in parts per million divided by 10^6. The acoustic velocity in pure water, V_w, in m/s is (Batzle and Wang, 1992)

$$V_w = \sum_{i=0}^{4}\sum_{j=0}^{3} w_{ij}T^iP^j, \tag{3.14}$$

and the coefficients w_{ij} are as provided by (Batzle and Wang, 1992). The acoustic velocity and density can be used to calculate the bulk modulii of brine using ${V_p}^2 = K/\rho$.

Oil: The acoustic velocity in dead oil, oil with minimal gas present, depends upon pore-pressure and temperature as (Batzle and Wang, 1992)

$$\begin{aligned} V_p(m/s) &= 2096(\tfrac{\rho_r}{2.6-\rho_r})^{1/2} - 3.7T + 4.64P \\ &+0.0115[4.12(1.08{\rho_r}^{-1} - 1)^{1/2} - 1]TP \end{aligned} \tag{3.15}$$

where ρ_r is reference standard density. The density of dead Oil is directly taken from simulation results.

Supercritical Carbon dioxide (SCF CO_2): The density of Supercritical CO_2 is directly obtained from simulation results, while the bulk modulus of supercritical

CO_2 can be calculated from the following relationship (Vargaftik, 1975),

$$\begin{aligned} K_{CO_2} &= 4.2911\times10^{-2} - 8.3309\times10^{-3}P \\ &+5.8377\times10^{-4}P^2 - 4.3896\times10^{-3} \end{aligned} \tag{3.16}$$

3.3.3 Seismic AVO Attributes

The amplitude of a seismic reflection from a boundary between two materials is approximately a linear function of the squared sine of the angle of incidence i (Shuey, 1985):

$$R(i) \approx R(0) + Gsin^2 i \tag{3.17}$$

Appropriately processed prestack seismic data, when sorted into common reflection point, or common midpoint, gathers, provide a measure of this reflection coefficient. Typical amplitude variation with offset (AVO) analysis fits a line to these measured reflection amplitudes to estimate the intercept R(0) and gradient G. The intercept is equal to the normal incidence reflection coefficient and can be considered an estimate of the seismic amplitude that would be observed in a typical seismic section. The values of these two parameters generated by hydrocarbon or CO_2 bearing formations are often significantly different from those of brine-saturated rock, providing a valuable tool for detecting fluids of interest.

In our model, however, the reservoir, with thickness b=20 m, is sufficiently thin that reflections from the top and bottom of the layer will interfere for seismic frequencies typical of surface seismic data (about 30 Hz) and so we cannot directly utilize the (Shuey, 1985) result. Lin and Phair et al. (1993) showed that composite reflection associated with this superposition or tuning still has the same general functional form, but the intercept and gradient of the line take the form:

$$R_t(0) = (4\pi bf)/V_g R(0) \tag{3.18}$$

$$G_t = ((4\pi bf)/V_g)(G - R(0)/2) \tag{3.19}$$

Here f is frequency, V_g is the interval velocity in the reservoir formation, and R(0) and G are the conventional AVO intercept and gradient respectively for the upper interface of the reservoir. By utilizing this tuned AVO solution, we obtain much faster results than we would with a simulation of the synthetic seismograms followed

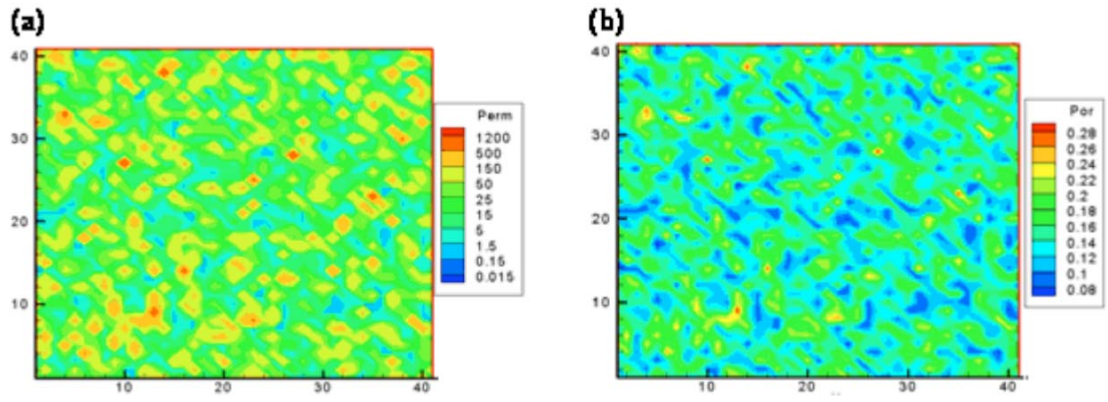

Fig. 3.1. (a) Porosity and (b) permeability in the weakly correlated reservoir model.

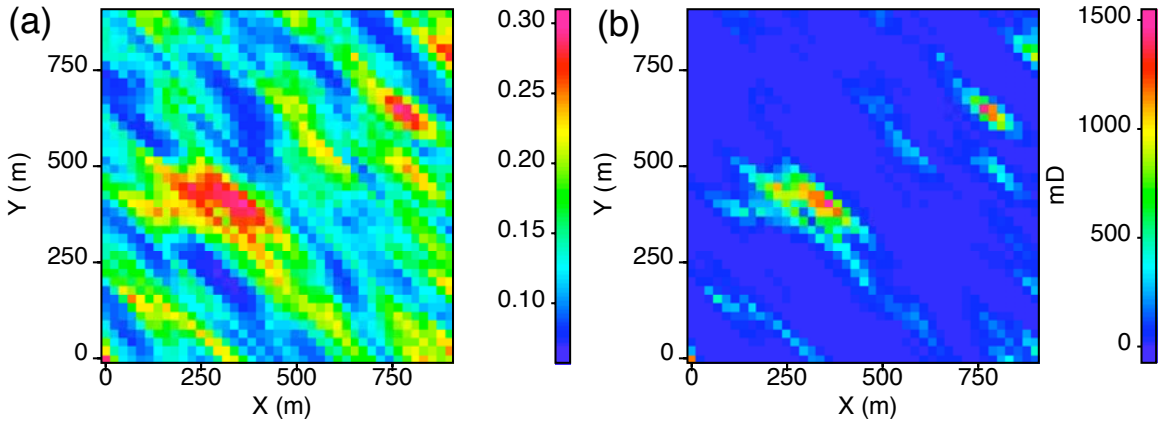

Fig. 3.2. (a) Porosity and (b) permeability in the strongly correlated reservoir model.

by processing.

3.4 Model Results and Discussion

For our modeling, we used a 2D model of a carbonate reservoir as shown in Table 3.4 with two different permeability distributions. The first case has a low spatial correlation ($\lambda_D \sim 0.01$) that causes a random distribution of permeability as shown in Figure 3.1. The second case has a high spatial correlation ($\lambda_D \sim 0.3$) leading to distinct flow channels as shown in Figure 3.2. A porosity-permeability relationship representative of a carbonate reservoir was used in this study (Jennings and Lucia, 2003).

Table 3.4. Reservoir model

Grid	41×41×1
Grid Size (m)	
$\Delta x = \Delta y$	22.43
Δz	20
Heterogenity	
Case I	Weakly coorelated
Case II	Strongly coorelated
Reservoir Compressibility	1.0e-08
Reference Pressure	1 MPa
Initial reservoir pressure	19.58 MPa
Initial water saturation	0.6

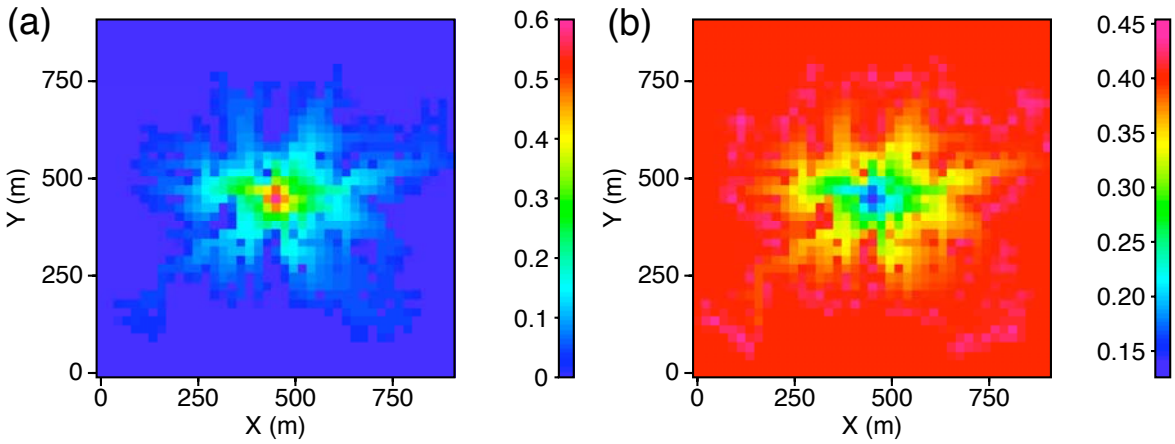

Fig. 3.3. (a) Gas Saturation, and (b) oil Saturation at 6 years (end of gas injection) for weakly correlated reservoir model.

Our modeling study was performed for CO_2 sequestration under post-waterflood conditions, having initial water saturation of 60%. We used a five spot pattern with a injector in the center and producers at the four corners of the model. The model is simulated with CO_2 injection for six years and then the wells are shut down. We measure results at 6 years (end of gas injection), 10 years, 100 years and 1000 years to model the seismic response corresponding to the reservoir conditions.

This section discusses modeling results associated with geochemical reactions during CO_2 injection and its impact on seismic response. Overall the primary objective is to examine the feasibility of seismic monitoring of CO_2 during CO_2 sequestration. For case 1, the host rock was considered to correspond to properties of 'vuggy' carbonate whereas for case 2, the host rock was considered to represent 'marly' limestone. Mean properties for these rocks were taken from measurements presented by Brown (2002).

3.4.1 Case 1 : Weakly Correlated Reservoir Model

Figure 3.1 shows the permeability distribution for the weakly correlated reservoir model case that has a low spatial correlation ranging from 0.1 md to 2200 md. CO_2 is injected for first 6 years and then all the wells were shut down. We monitored the reservoir conditions at 10 years, 100 years and 1000 years. Figure 3.3 show the gas (primarily supercritical CO_2) and oil saturation in the reservoir at the end of 6 years. The corresponding pressure change and the dissolution of CO_2 in brine are

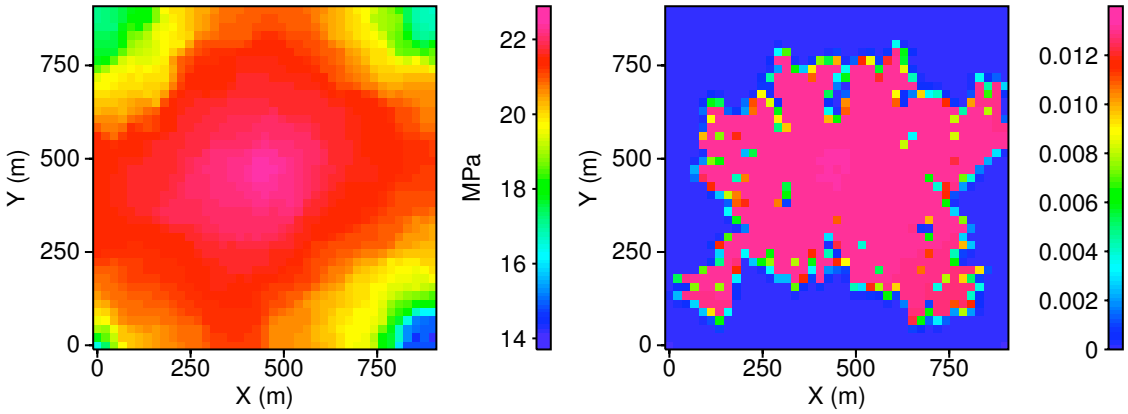

Fig. 3.4. (a) Pressure, and (b) CO_2 concentration in brine at 6 years (end of gas injection) for weakly correlated reservoir model.

shown in Figure 3.4. Since the wells are shut down after 6 years, the reservoir reaches equilibrium around 10 years with reservoir pressure around 24 MPa. The decrease in pressure is mainly due to the formation of bicarbonate ions due to the mixing of CO_2 and brine. This reduces the amount of gas present in the reservoir and thus reduces the reservoir pressure. The mixing of CO_2 into the reservoir brine changes the brine density and pH due to chemical interactions. The distribution of salinity and brine densities are shown in Figure 3.5. After 6 years, the brine salinity changes (calculated as TDS) by 10%, thus changing the density of the brine. As the gas-aqueous system reaches equilibrium (around 10 years), the salinity changes become very slow at later times. This can be attributed to fact that fast aqueous reactions are predominant only during the first few years while gas is being injected, and after that only slow mineral reactions shift the equilibrium.

CO_2 also mixes with oil, changing their oil density but the effect is opposite compare to mixing of CO_2 in brine as shown in Figure 3.6(a), and the corresponding gas density distribution is shown in Figure 3.6(b). The lowering of pH during CO_2 injection triggers several geochemical reactions that lead to precipitation of minerals such as Calcite and Kaolinite, and dissolution of Anorthite. Figure 3.7, Figure 3.8, Figure 3.9 show the mineral precipitation/dissolution profiles for Calcite, Kaolinite, and Anorthite respectively at 100 and 1000 years. The positive values indicate mineral precipitation (Calcite and Kaolinite). while negative values indicate dissolution

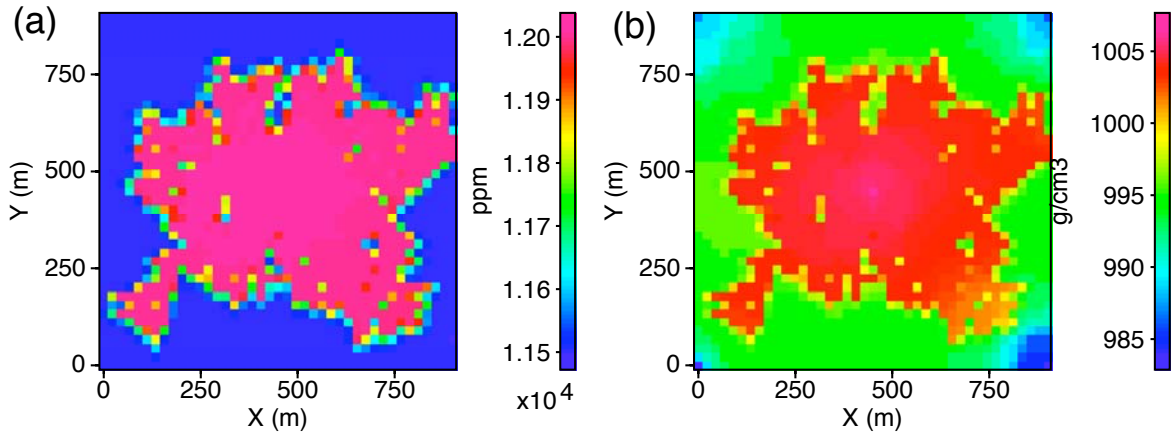

Fig. 3.5. (a) Salinity, and (b) brine density at 6 years (end of gas injection) for weakly correlated reservoir model.

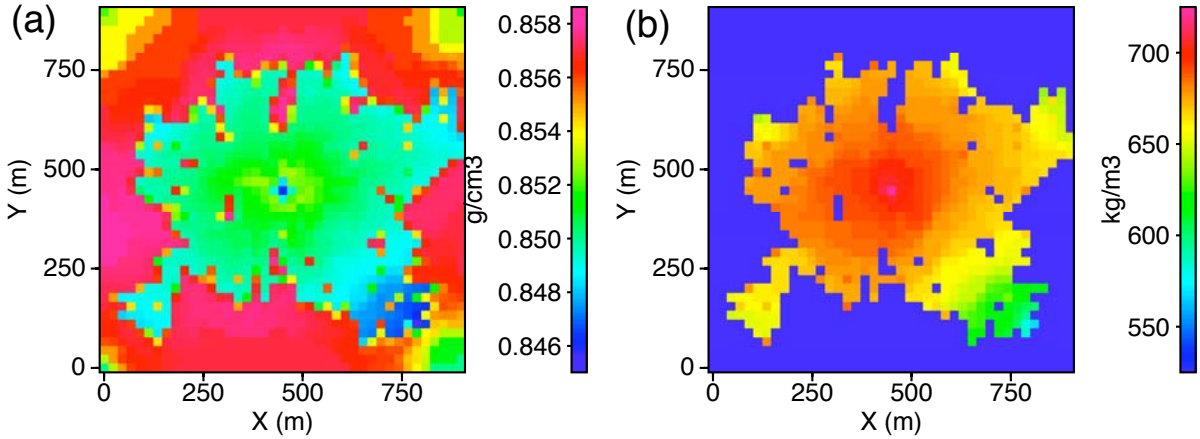

Fig. 3.6. (a) Oil density, and (b) gas Density at 6 years (end of gas injection) for weakly correlated reservoir model.

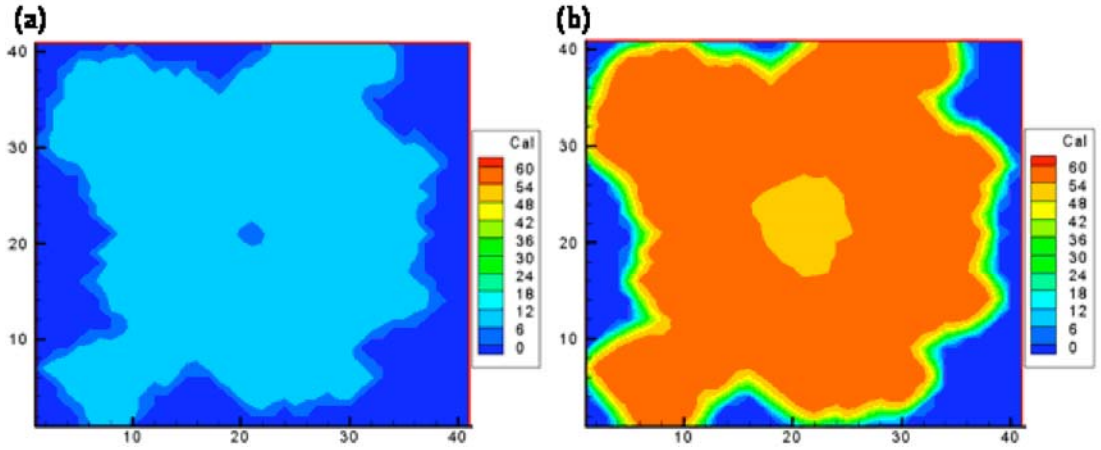

Fig. 3.7. Moles of calcite precipitated at (a) 100 years, and (b)1000 years for weakly correlated reservoir model.

(Anorthite). The calcium cations require for calcium precipitation is provided by the dissolution of anorthite. Thus, the calcite precipitation is symmetric with the anorthite dissolution. Porosity changes due to these mineral reactions are of order of 0.15%, and 1.5% are observed at times 100 years, and 1000 years respectively (Kumar et al., 2008).

We used Gassmann equation to compute the changes in seismic properties. For this model, the reservoir is assumed to be located at a depth of 2 Km, overlain by an isotropic and homogenous medium of = 4.5 Km/s, =2.5 Km/s and density= 2.2 g/cc. Figure 3.10 shows changes in compressional velocity, V_p, at t = 6, 10, 100 and 1000 years. These changes are computed with respect to the initial conditions at t = 0. Because of CO_2 injection and the mineral precipitation/ dissolution with accompanying porosity changes, the velocity decreases by 2.73%, 2.75%, 2.765% and 2.87% at t = 6, 10, 100 and 1000 years respectively. The AVO intercept and gradient parameters provide important insights into the seismic detectability of the CO_2 front. The intercept parameter, R(0) , which undergoes a decrease of 13.63%, 14.14%, 13.85% and 11.6% at the monitoring times, t = 6, 10, 100 and 1000 years, and the corresponding changes in gradient are 5.02%, 5.07%, 5.09% and 5.45% respectively (Figure 3.11). However, as we know the mineral reactions are slow reactions and their effects are dominated after the reservoir reaches pressure equilibrium. In order to understand their effect on seismic properties, we subtracted the results of t = 1000 years with t = 6 years (Figure 3.12). Figure 3.12 clearly shows that the maximum change in the

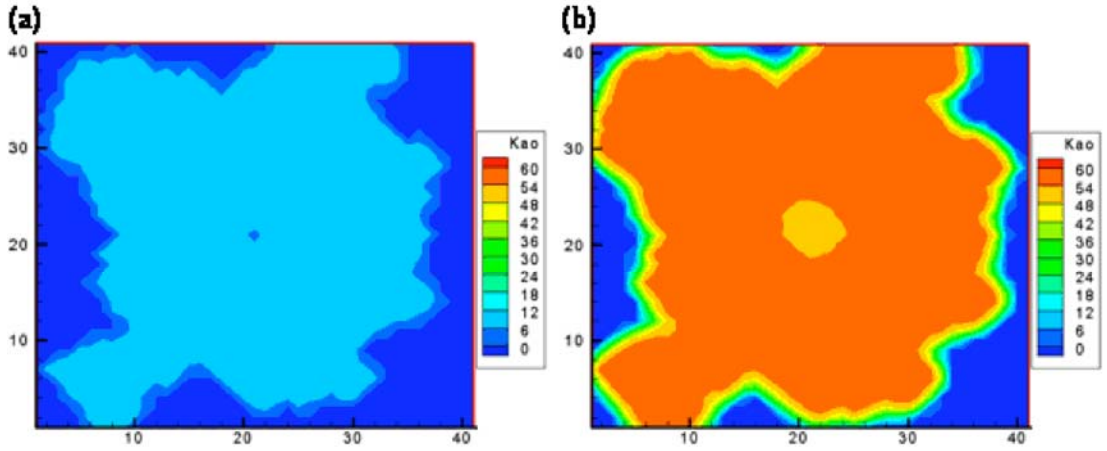

Fig. 3.8. Moles of kaolinite precipitated at (a) 100 years, and (b)1000 years for heterogenous field with small correlation length.

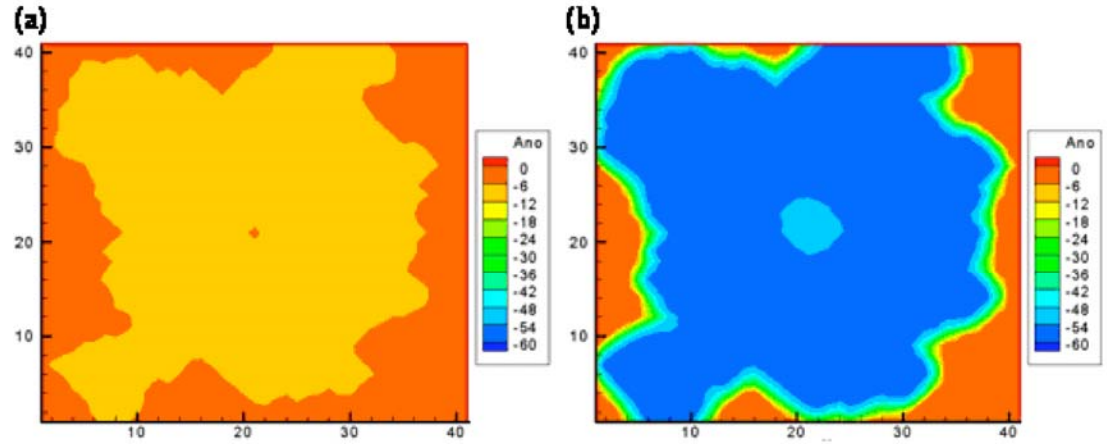

Fig. 3.9. Moles of anorthite precipitated at (a) 100 years, and (b)1000 years for heterogenous field with small correlation length.

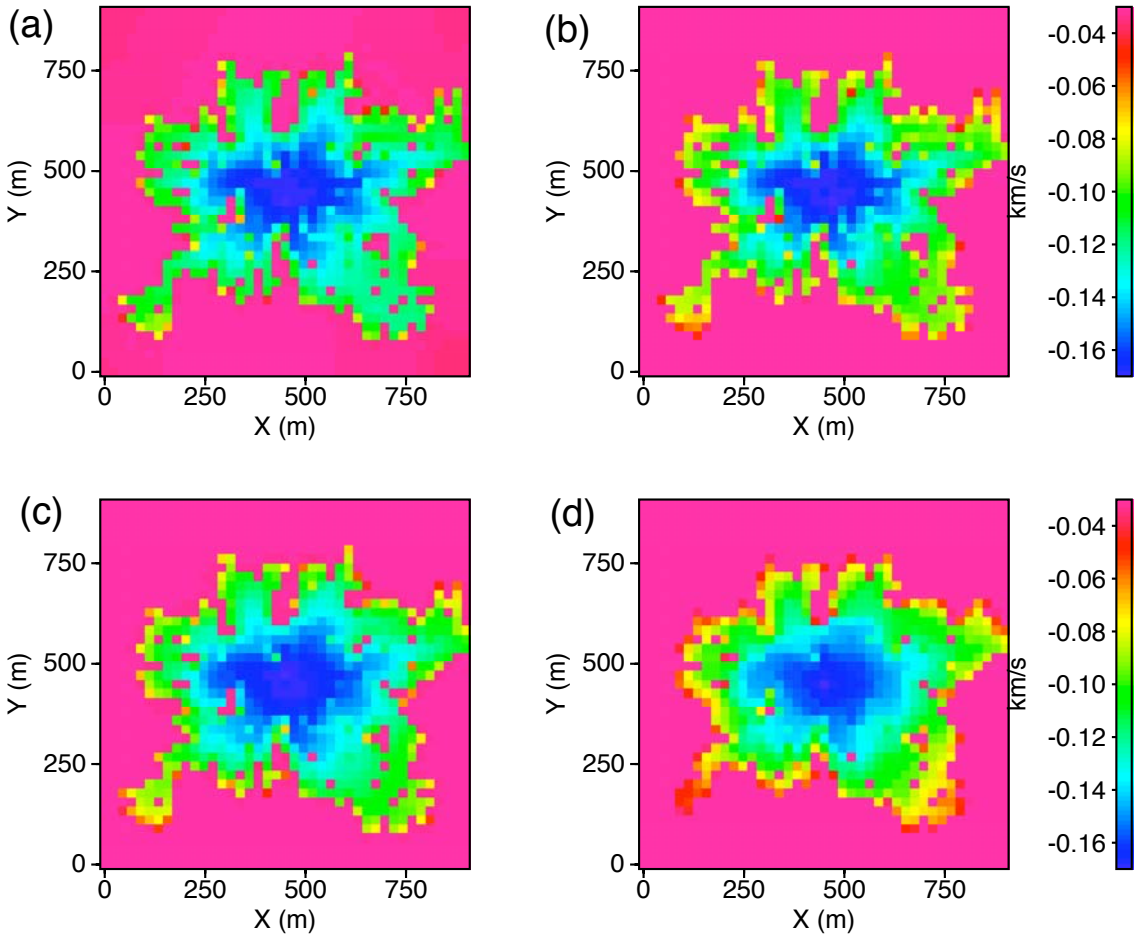

Fig. 3.10. Difference of V_p between (a) $t = 6$ years (b) $t = 10$ years (c) $t = 100$ years and (d) $t = 1000$ years with $t = 0$ year respectively for weakly correlated reservoir model.

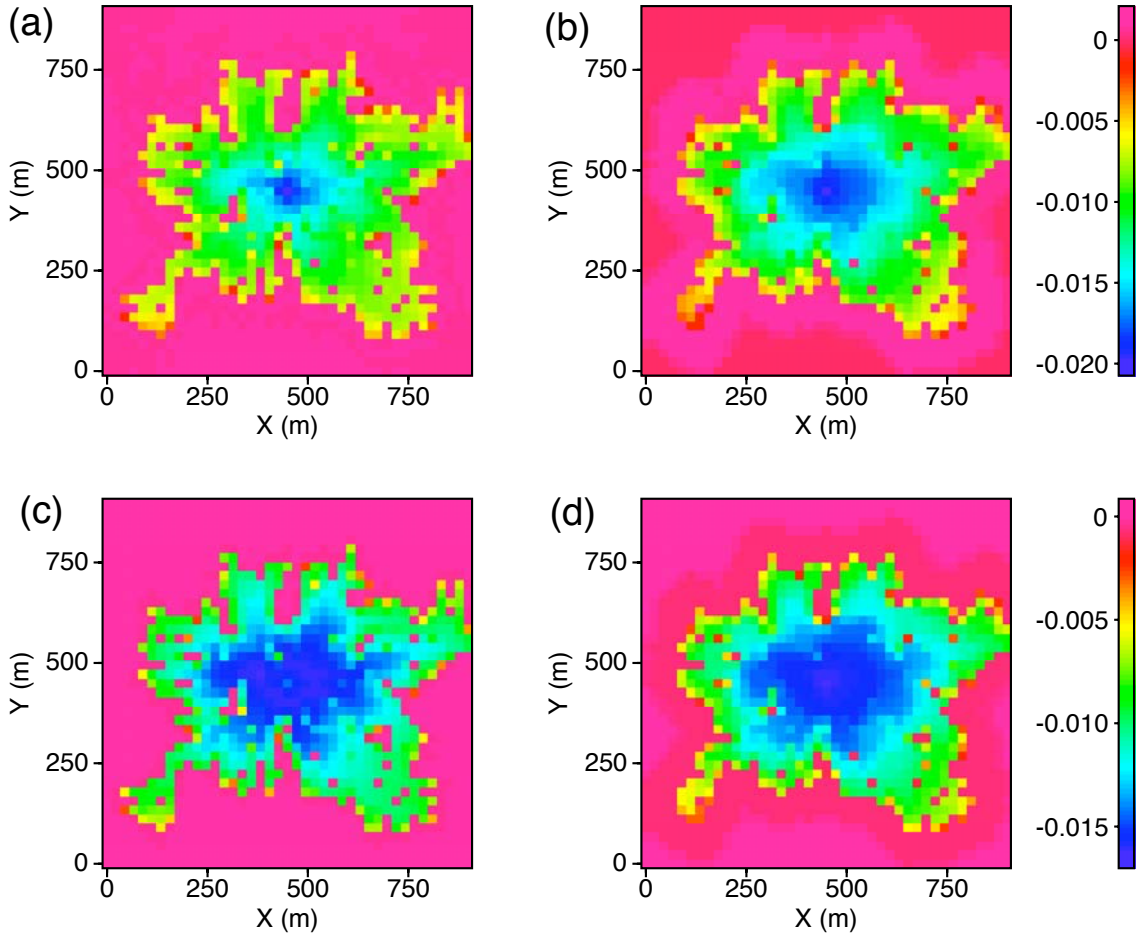

Fig. 3.11. Difference of intercept between (a) t =10 years and (b) t = 1000 years with t = 0 year respectively for weakly correlated reservoir model. (c) and (d) represent same profile for gradient.

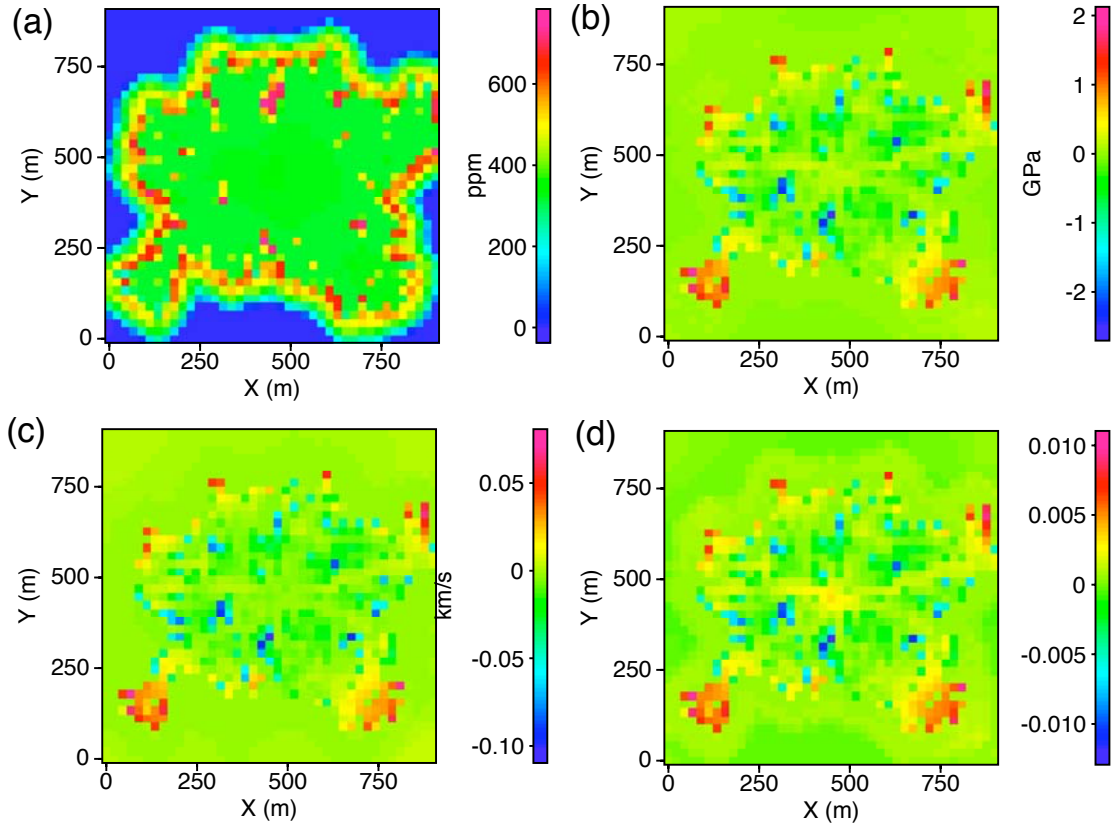

Fig. 3.12. Difference of (a) salinity (b) reservoir bulk modulus (c) compressional velocity (d) intercept between (a) t =1000 years and (b) t = 6 years respectively for weakly correlated reservoir model.

intercept occurs at the boundary of the CO_2 front that can be useful in detecting the flow of CO_2 inside the reservoirs. The maximum change in various seismic properties at the boundaries is because of the continuous chemical activities between acidified reservoir fluids and host rock at the boundary.

In order to better understand the individual effects of these processes, we constrained our study for one particular grid cell (516 m, 448 m) that shows significant changes. For first 6 years, out of the total injected CO_2 partially dissolved into brine, some leads to formation of carbonic acid whereas rest enhances oil production. The formation of carbonic acid triggers a variety of geochemical reactions that can alter rock composition and brine salinity whereas dissolution increases brine density, changing bulk properties of reservoir fluids, as shown in (a), (b) and (c) respectively in Figure 3.13. The reservoir reaches pressure equilibrium by 10 years, thus reducing the rates of fast reactions. After 10 years, the mineral reactions that are slower becomes more active than the faster intra-aqueous reactions. During mineral reactions, some of the brine species start interacting with host rock minerals, decreasing the density of brine. The low rate of change of seismic properties and amplitudes at times after 10 years is due to the slow rate of mineral reactions. Most of the effect of these geochemical reactions is discernible by 100 years but then also, their overall affect on seismic velocity, thus seismic amplitudes, is not more than 2%., that may be difficult to detect on noisy seismic data (Figure 3.13(d)). However, the significant change in the seismic properties at the boundary of the CO_2 front can be used to detect the flow path of CO_2 inside these reservoirs.

3.4.2 Case 2: Strongly Correlated Reservoir Model

The permeability distribution for this case shows strong anisotropy and long range spatial correlation as shown in Figure 3.2. Here, also we injected CO_2 using five-spot pattern with injector in the center and producers at the four corners. Due to permeability anisotropy, the movement of CO_2 front is channelized, preferential to south-east direction. Figure 3.14 shows the gas saturation and gas density at the end of 6 years of CO_2 injection. The reservoir pressure distribution and brine densities at the end of 6 years are shown in Figure 3.15.

For seismic modeling, the reservoir is assumed to be overlain by an isotropic and homogenous medium having Vp = 3.55 Km/s, Vs=2.8 Km/s and density = 1.6 g/cc.

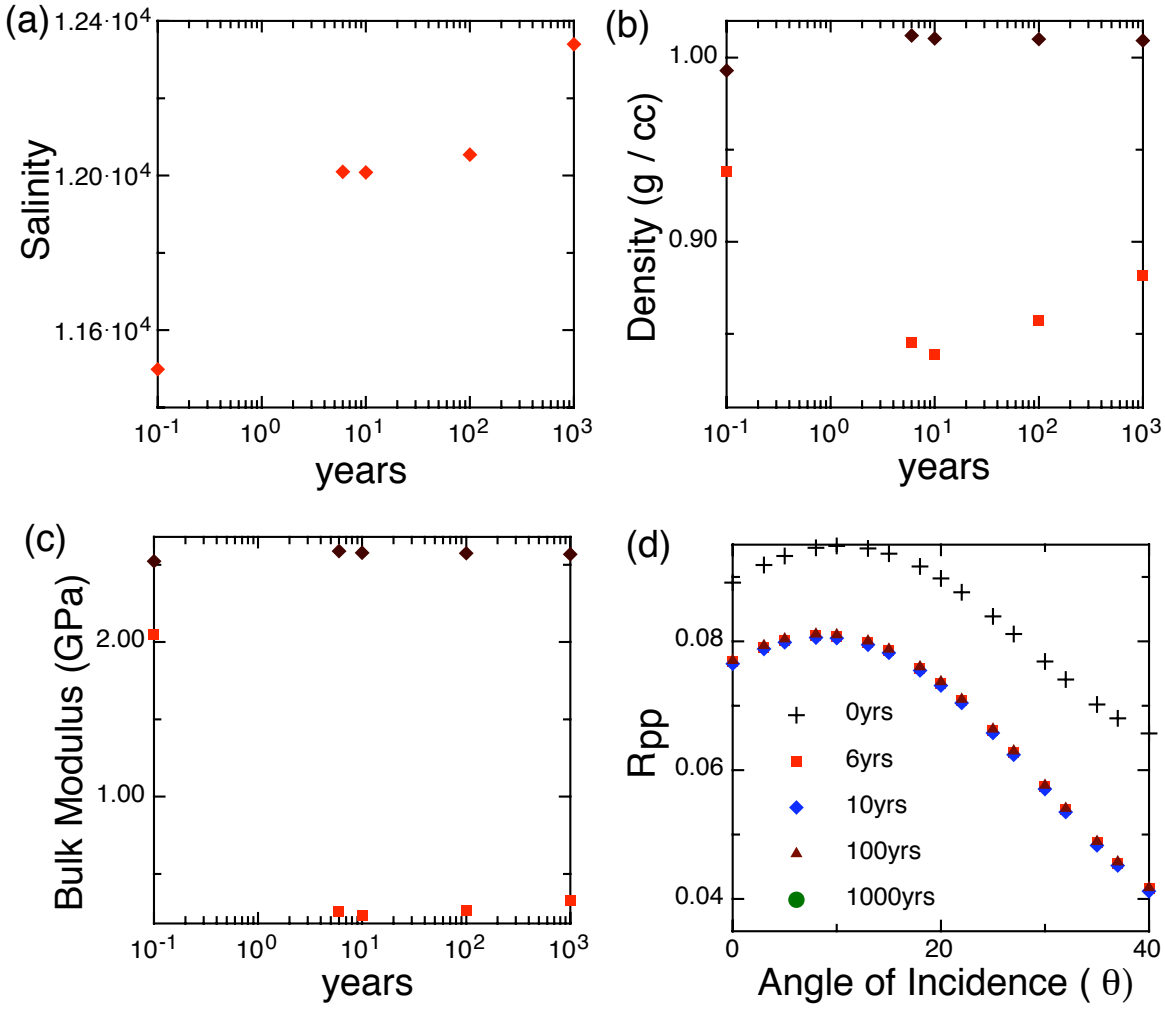

Fig. 3.13. Change of (a) salinity (b) brine (brown) and bulk reservoir fluid (red) densities (c) brine bulk modulus (brown) and reservoir fluid bulk modulus (red) with time (d) Reflection coefficient as a function of angle of incidence.

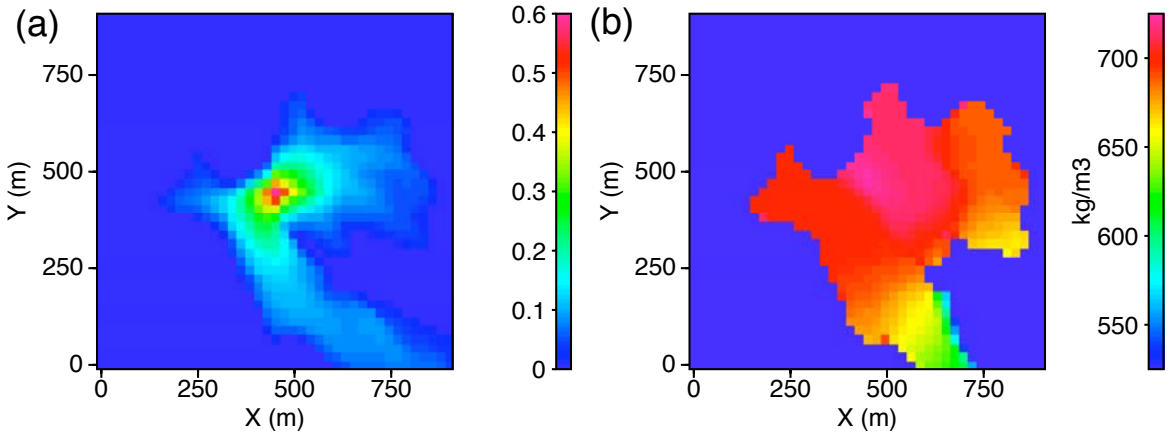

Fig. 3.14. (a) Gas saturation, and (b) gas density at 6 years (end of gas injection) for strongly correlated reservoir model.

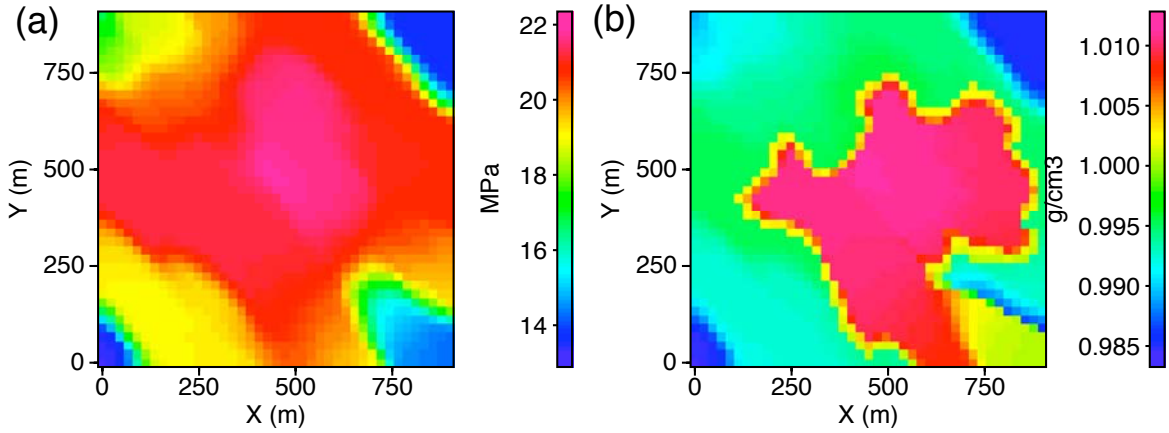

Fig. 3.15. (a) Pressure, and (b) brine density at 6 years (end of gas injection) for strongly correlated reservoir model.

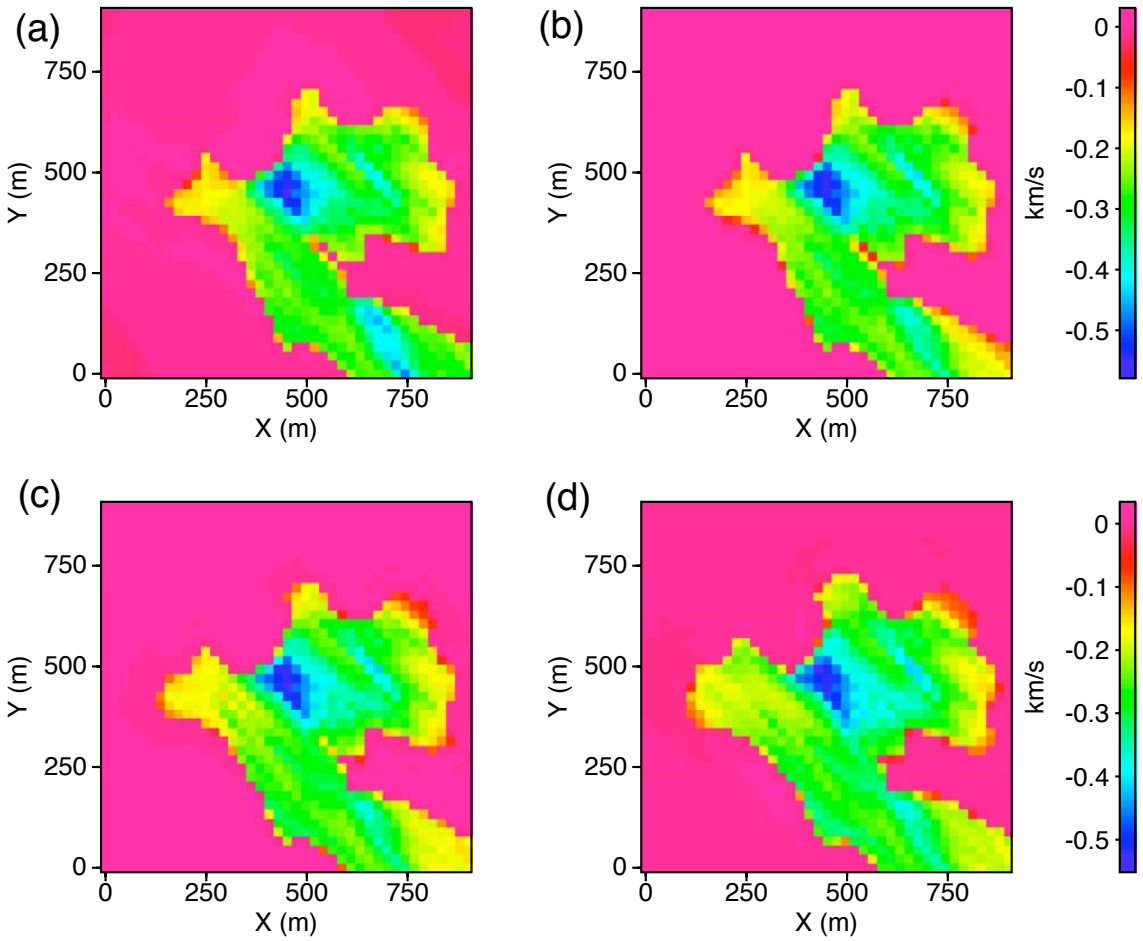

Fig. 3.16. Difference of V_p between (a) $t = 6$ years (b) $t = 10$ years (c) $t = 100$ years and (d)$t = 1000$ years with $t = 0$ year respectively for strongly correlated reservoir model.

Figure 3.16 shows the change in Vp at $t = 6$, 10, 100 and 1000 years with respect to the at time $t = 0$. Figure 3.17 shows change in the intercept and the gradient at $t =$ 10 and 1000 years respectively with respect to $t = 0$ years.

Figure 3.18 shows some of the more important chemical and seismic modeling results for the model. The CO_2 saturation is largest near the injection site, and the salinity and calcite precipitation are distributed in patterns controlled by the heterogeneous permeability field. Figure 3.18 also shows that the decrease in compressional velocity after t=1000 years is 10-15%. The potential causes for the velocity decrease are the reduction of the fluid bulk modulus when CO_2 enters the pore space, intra-aqueous reactions, and the geochemical reactions between CO_2 reservoir fluids and the minerals in the formation. However, as we know the mineral reactions are slow

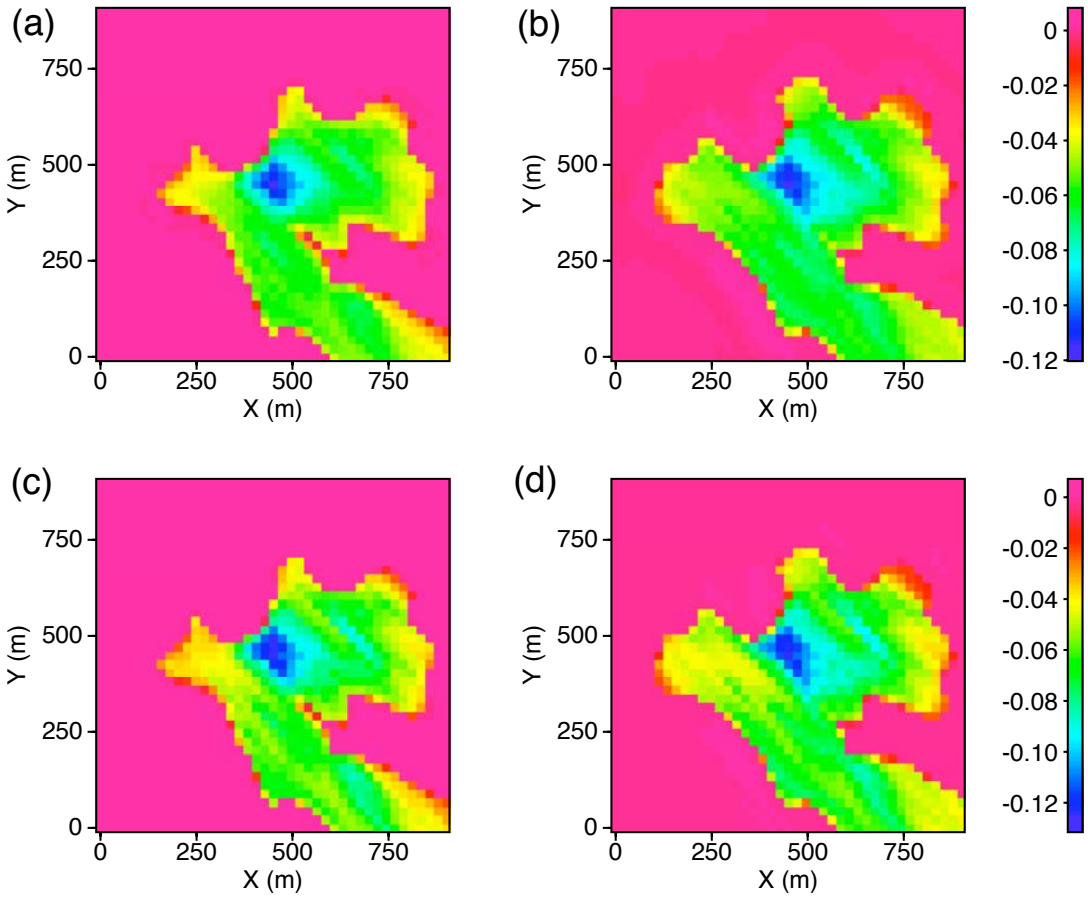

Fig. 3.17. Difference of intercept between (a) t =10 years and (b) t = 1000 years with t = 0 year respectively for strongly correlated reservoir model. (c) and (d) represent same profile for gradient.

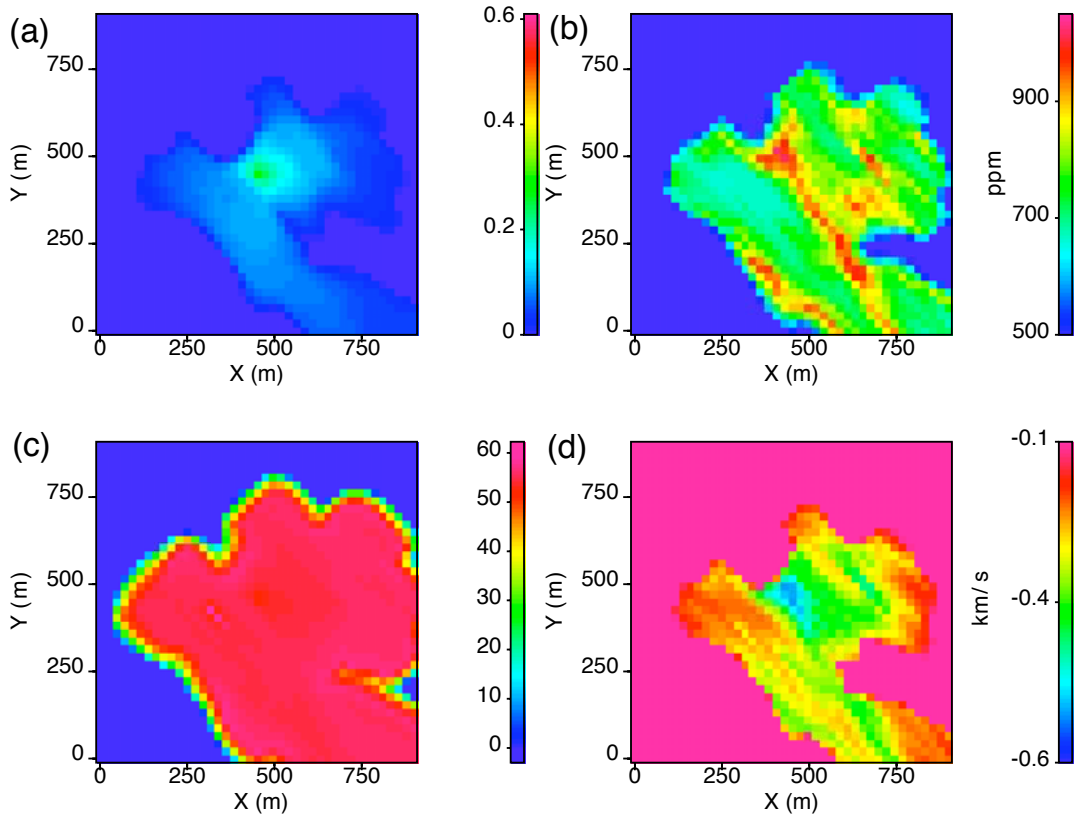

Fig. 3.18. Change in (a) CO_2 saturation, (b) salinity, (c)moles of calcite precipitation, and (d) compressional velocity from t=0 to t=1000 years.

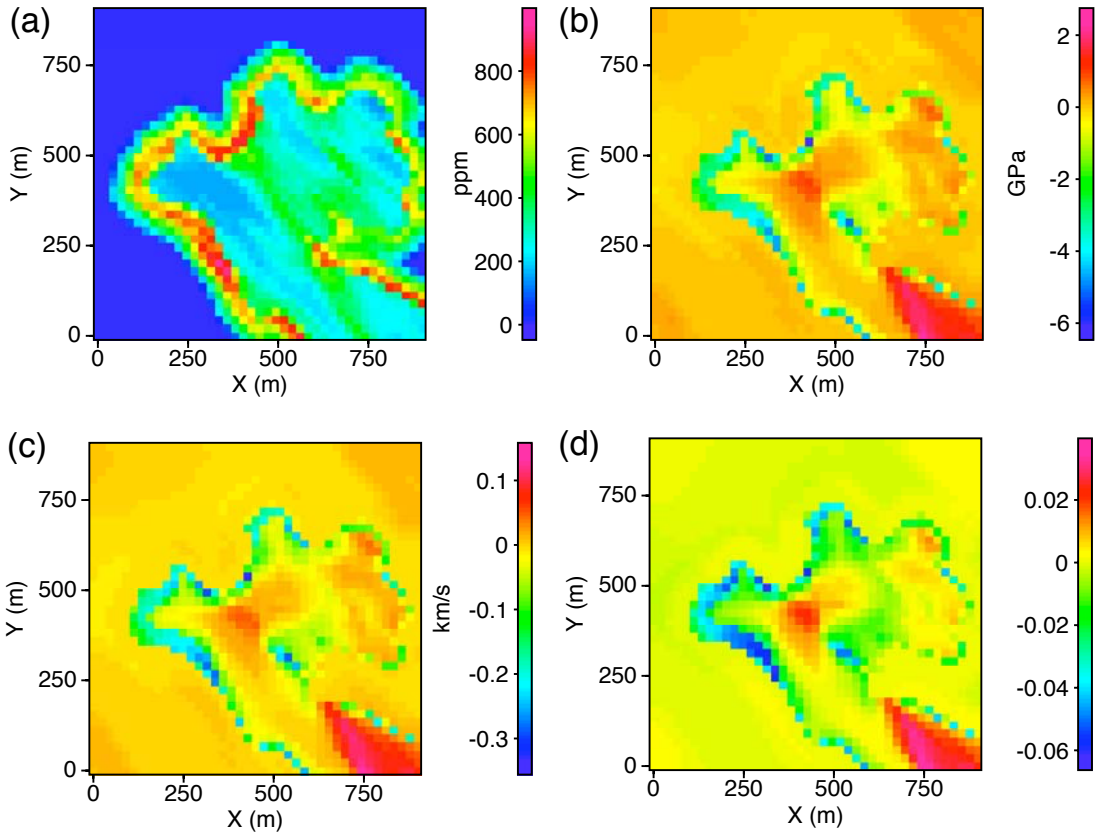

Fig. 3.19. Change in (a) salinity, (b) reservoir bulk modulus, (c) compressional velocity, and (d) intercept from t=6 to t=1000 years.

reactions and their effects are dominated after the reservoir reaches pressure equilibrium, hence we subtracted the results from $t = 1000$ years to $t = 6$ years when all the wells were shut down. Figure 3.19 is used to show the influence of mineral reactions on rock properties. This figure clearly suggests that the slow mineral reactions have very small effect on the wave velocity of the host rock, thus very small change in intercept. However, the maximum change occurs at the boundary of the CO_2 front that can be used to detect the flow of CO_2 in the reservoirs. The maximum change at the boundary is because of sharp change in the properties between background matrix and CO_2 saturated rock due to continuous geochemical reactions. The more detail analysis of this model case is discussed below.

During the six years of CO_2 injection, the reservoir is not in pressure equilibrium, which enhances the faster intra-aqueous reactions. Part of the injected CO_2

is partially dissolved into brine, and some forms carbonic acid. The dissolution of CO_2 increases brine density, while the formation of carbonic acid triggers a variety of geochemical reactions that can alter rock composition and brine salinity. After the injection period, when all the wells were shut down, the reservoir eventually reaches pressure equilibrium, thus reducing the importance of fast reactions and emphasizing the slower mineral reactions. This equilibrium is achieved at about $t = 10$ years in the simulation. In order to clarify the relative importance of chemical and fluid substitution effects on fluid properties, we consider one particular grid cell in more detail. This cell, located at (516 m, 448 m), was selected because it showed large changes in seismic velocities. While the brine properties have relatively little change, the total fluid and bulk properties of the porous reservoir rock show significant variability during the period of injection only (Figure 3.20). The changes in properties after injection, at least for density, are not negligible, but the biggest changes are during injection. Dramatic decreases in bulk modulus and density must therefore be caused by injection CO_2 and not by subsequent chemical reactions. Gassmann equation calculations support this conclusion by showing that compressional velocity decreases by 10-14% after six years (Figure 3.20d). Furthermore, comparisons of compositional modeling with and without chemical reactions suggest that the contribution of intra-aqueous reactions is less than 2% change in velocities. Figure 3.21 shows that the change in AVO attributes in models with and without chemical reactions is negligible at a time point of 10 years. Thus, the majority of decrease in this early stage must be attributed to the injection of a fluid, CO_2 with a low bulk modulus, thus reducing the bulk modulus of the reservoir. Once the reservoir is in pressure equilibrium, the chemical reactions will be the only cause of time-lapse seismic signals. Since these reactions are comparatively slow, the changes in seismic amplitude are small (Figure 3.22). During mineral reactions, some of the brine species interact with host rock minerals, decreasing the brine density. The simulation results also show that these reactions cause an increase in porosity of about 0.15% and 1.5% after t=100 and t=1000 years. respectively, though this has negligible influence on seismic properties. In general, most of the effect of the geochemical reactions is discernible in the seismic amplitudes by 100 years but even then their overall affect on seismic velocity, and thus seismic amplitudes, is not more than 2-5% (Figure 3.22). However, the significant change in the seismic properties at the boundary of the CO_2 front can be used to detect the flow path of CO_2 inside these reservoirs.

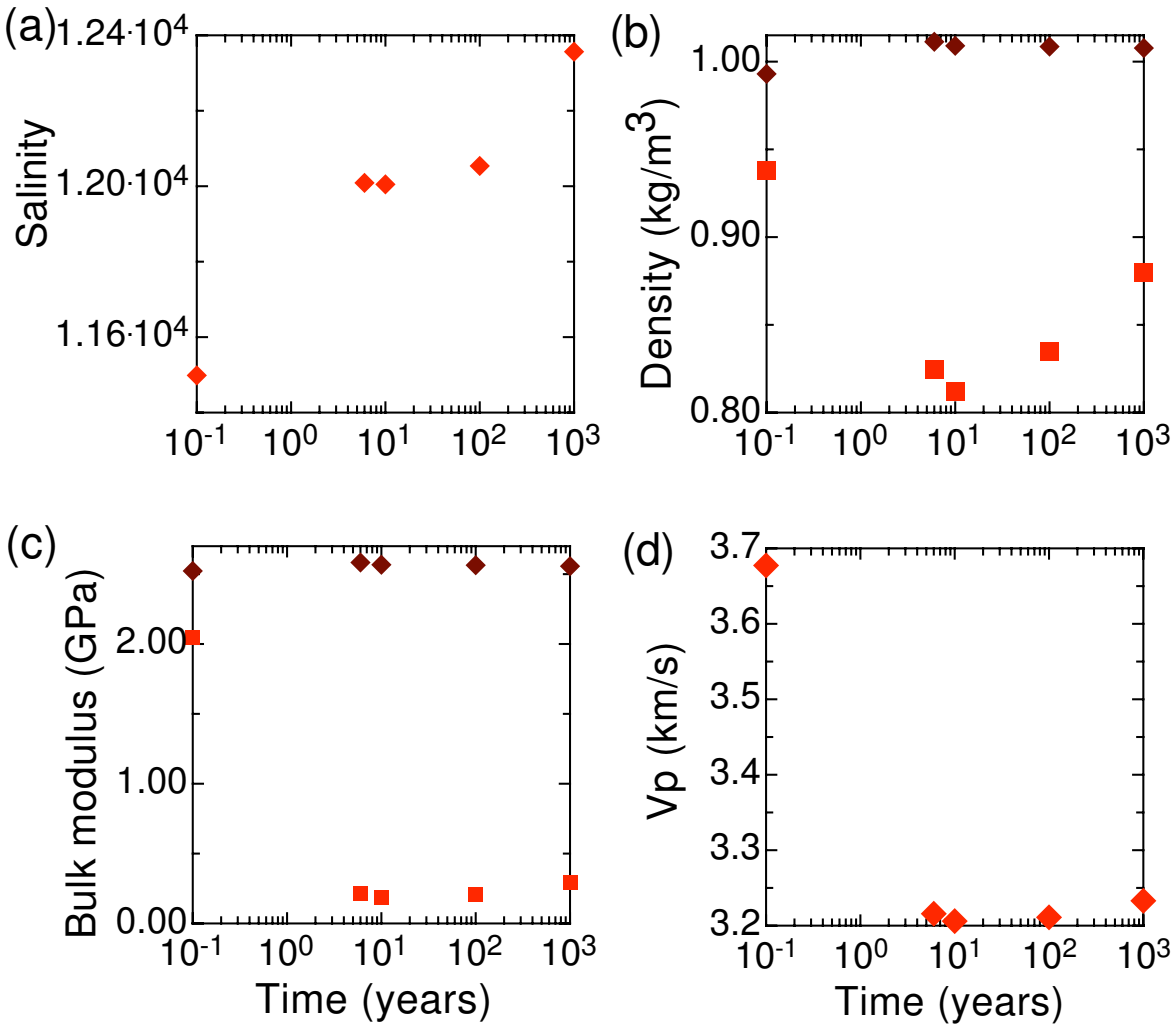

Fig. 3.20. Values of model properties as a function of time in the grid cell at (516 m, 448 m). (a) salinity, (b) brine (brown) and bulk reservoir fluid (red) densities, (c) brine bulk modulus (brown) and reservoir fluid bulk modulus (red), (d) bulk compressional velocity.

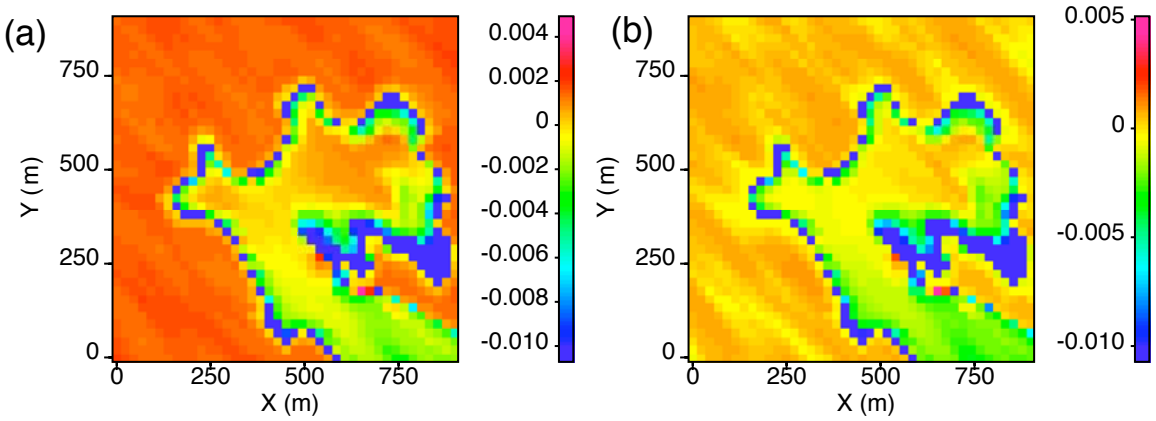

Fig. 3.21. Relative change in AVO parameters (a) intercept and (b) gradient when chemical reactions are neglected. The values are the relative change compared to the complete model results that do include geochemical reactions.

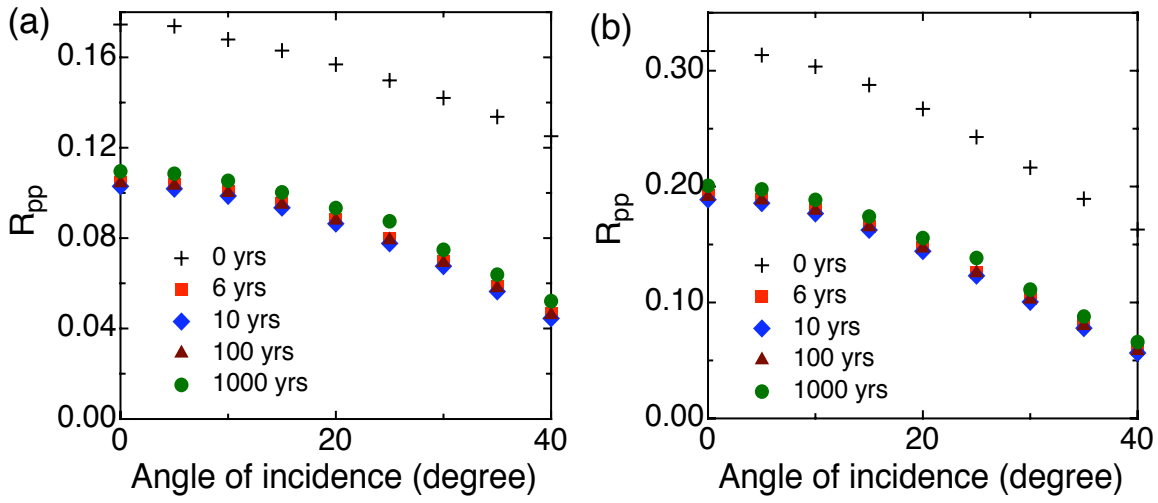

Fig. 3.22. Reflection coefficient versus angle of incidence for (a) two half space model and (b) thin layer embedded in isotropic medium in one grid cell at (516 m, 448 m).

3.5 Conclusions

Our modeling combines comprehensive flow simulation, including chemical processes, with seismic simulations to model the CO_2 injection that includes all the accompanying phase behavior and geochemical effects. The CO_2 dissolution and the acidification triggers a variety of geochemical reactions that can significantly alter the rock-fluid properties. Our modeling shows that intra-aqueous reactions are more significant during injection of CO_2, while slower mineral reactions dominate after pressure equilibrium is achieved. Overall both types of geochemical reactions, intra-aqueous and mineral reactions, cause a change in reflection coefficient of 2 to 5%, which can be generally very difficult to detect in noisy field data. So, even though geochemical reactions affect seismic data during CO_2 injection, the seismic signals are dominated by reductions in bulk modulus associated with fluid substitution effects modeled using the Gassmann equation. However, the significant change in the seismic properties at the boundary of the CO_2 front can be used to detect the flow path of CO_2 inside the reservoirs.

CHAPTER IV

CORRELATED FRACTURE NETWORK MODELING USING STATISTICAL AND STOCHASTIC PROCESSES

4.1 Introduction

The quantification of the spatial distribution of fractures in low permeability rocks is essential as they control the nature of fluid flow in those rocks. Generally, these spatially distributed fractures form complex networks that can either act as fluid carriers or barriers depending upon fracture connectivity. Therefore, understanding the connectivity pattern, at least for areas of high and low fracture density zones, becomes crucial for estimating flow characterization inside the earth. To date most research has considered the effect of geometrical properties of fractures such as length (Berkowitz, 1995; Bour and Davy, 1997) and orientation (Robinson, 1984; Balberg et al., 1984; Masihi et al., 2005) on the scaling laws of the connectivity of fractures. The scaling law of connectivity is the power law equation like in percolation theory that determines the span of the cluster of connected fractures. However, very few studies have been performed on the spatial correlation such as length, orientation and position of fractures, though some of the studies were mainly concentrated on long-range density correlations using fractal geometry (Berkowitz et al., 2000; Darcel et al., 2003b). The knowledge of spatial correlation parameters are important as they determine the connectivity of fractures. For example, orthogonal sets of fracture cluster has higher connectivity compare to parallel set of fractures. Bour and Davy (1999) have studied the correlation between the position and the length of the fracture. However, still one of the major concern in industry as well as academia is to determine parameters affecting connectivity of fractures that can improve the prediction of fluid flow inside the earth.

A more thorough understanding of the correlations of fracture locations and properties provides better insights into flow properties of fracture network models utilized for numerical modeling of fluid flow. A common approach is to applied discrete fracture network (DFN) methods, which produces a list of locations, sizes, and orientations of individual fractures. Generally DFN models require specification of

the statistical distributions of several parameters such as fracture density, orientation, location, size, aperture, connectivity etc. to generate several realizations for production estimation, reservoir planning such as to target drilling wells at dominantly connected fractures. The first chapter of this dissertation outlines an integrated approach of modeling fractures using Discrete fracture network and seismics. Here, we implement and extend a new model of the spatial distribution of fractures using physics of fracturing process (Masihi and King, 2007), which is not explicitly considered in DFN modeling. The idea for modeling is based on the fact that the elastic free energy associated with the fracture density follows Boltzmann distribution. The expression that determines the spatial correlation function for the displacement of fractures, discussed in detail later, is used as an objective function to generate several realizations for fracture distributions using simulated annealing algorithm that minimizes the objective function. The basic assumption for this method is that the reference rock sample used for study is already fractured and the rock sample has already achieved mechanical equilibrium. This equilibrium assumption allows us to use entropy arguments and statistical mechanics for modeling fractures. The goal of our study is to extend the stochastic modeling technique of fracture distributions into real field observations. The stochastic models generated with this concept were also compared with DFN models, followed by their integration with seismic study.

4.2 Correlation in the Elastic Displacement of Fractures

This section discusses important steps involve in the derivation of the expression for the spatial correlation of the elastic displacement of fractures. The complete derivation is given in Appendix C. We write the displacement within the fractured rock volume as $\mathbf{u}(\mathbf{x}) = \mathbf{x} - \mathbf{x}^{'}$, noting that the particle at $\mathbf{x}$ has moved to $\mathbf{x}^{'}$. Using the theory suggested by Landau and Lifshitz ((1982b), Chapter IV) that describes relation of elastic deformations in the presence of dislocations, Masihi et al. (2007) suggests that a fracture in the rock sample is defined as discontinuity in the displacement vector in the elastic medium. So, any displacement vector is assumed to have continous part (elastic displacement $\mathbf{u^e}$) and a discontinous part (the inelastic displacement $\mathbf{u^i}$) that can act as a source for inelastic strain. Similarly, the strain and

stress can be decomposed into elastic and inelastic parts,

$$e_{ij} = e^e_{ij} + E_{ij} \text{ and } \sigma_{ij} = \sigma^e_{ij} + S_{ij} \tag{4.1}$$

If the system is in mechanical equilibrium i.e. in the absence of any external body forces, the equation of continuity becomes,

$$\partial_j \sigma_{ij} = \partial_j \sigma^e_{ij} + \partial_j S_{ij} = 0 \text{ or } \partial_j \sigma^e_{ij} = -\partial_j S_{ij} \tag{4.2}$$

where the inelastic part of stress, internal sources of stress, becomes the fictitious body force that gives rise to displacement and fracturing and also keeps fractures open. From Heffer and King et al. (2006), the total elastic energy per unit volume required to keep fractures open is the work done by elastic forces on the total strain. This total elastic energy is given as

$$E = \frac{1}{2}\sigma^e_{ij}\epsilon^e_{ji} \tag{4.3}$$

Using Fourier transforms of stress and strain and contracting above terms together leads to an expression for the elastic energy,

$$\begin{aligned} E(\mathbf{k}) &= \frac{1}{2}[(\lambda+\mu)k_k k_l + \mu k^2 \delta_{kl}]u^e_k(\mathbf{k})u^e_l(-\mathbf{k}) = \frac{1}{2}\mu[k^2\delta_{kl} + \frac{1}{1-2\nu}k_k k_l] \\ &= \frac{\mu}{2}L_{kl}(\mathbf{k})u^e_k(\mathbf{k})u^e_l(-\mathbf{k}), \end{aligned} \tag{4.4}$$

where L_{kl} is the usual linear operator of isotropic elasticity and is the inverse of the Green's function, $L_{kl}G_{lm} = \delta_{km}$. Applying the assumption that the frequency distribution, $p(E)$, of strain energy due to the displacements/dislocations or fractures follows Boltzmann Law,

$$p(E) \propto exp(-E/ < E >), \tag{4.5}$$

implies that the dislocations or fractures adopt a configuration that maximizes the entropy of the system subject to mean strain energy, $< E >$, being fixed. This assumption leads to the following expression for the spatial correlation between the

elastic displacements or fractures in real space,

$$\begin{aligned} C_{kl}(\mathbf{r}) &= \frac{< E >}{\mu} G_{kl}(\mathbf{r}) \\ &= \frac{< E >}{16\pi\mu(1-\nu)} \Big(\frac{(3-4\nu)\delta_{kl}}{r} + \frac{\mathbf{r_k}\mathbf{r_l}}{r^3} \Big) \end{aligned} \tag{4.6}$$

where the terms $< E >$, μ, ν are the average strain energy, the shear modulus of elasticity and the Poisson ratio of the rock sample. The random functions simulated with this covariance relationship will satisfy Equation 4.2, which can be used to determine both σ^e_{ij} and ϵ^e_{ji}. From the Appendix C, it can be clearly shown that the energy function for the above distributions of fractures can be simplified as

$$E = \sum_{k=1}^{N} \sum_{\substack{l=1 \\ k \neq l}}^{N} A u_k u_l [\eta |cos(\theta_k - \theta_l)| + |cos(\alpha - \theta_l) cos(\alpha - \theta_k)|] / r_{kl} \tag{4.7}$$

where $A = < E > /16\pi\mu(1\text{-}\nu)$, N is the number of fractures in the system, and α, θ_k and θ_l are the orientation of distance vector r and fractures u_k and u_l with respect to the horizontal, respectively and u_k and u_l are the length of fractures in k and l direction. This equation computes the pairwise interactions of fractures.

4.3 Modeling Methods and Analysis

4.3.1 Simulated Annealing Algorithm

Simulated Annealing (SA) is a stochastic optimization method that has been used in variety of problems that involve finding global optimum values of a function consisting of large number of independent variables. Tran (2007) suggests that the basic concept behind SA originates from the physical process of metallurgical annealing where annealing process occurs when a metal in a heat bath, initially at very high temperature, is slowly cooled. In the beginning at very high temperature, all the particles are distributed randomly in a quasi-liquid state and as the temperature drops, particles arrange themselves in low-energy ground state, probably at or very close to global minimum of energy, forming a crystal. To apply SA for any problem, one must define following terms:

- A description of set of possible configuration of the system.

- A random number generator that can be used for systematic perturbing or changing the configuration of the system.
- An objective function E (analog of energy) whose global minimization should be the goal of the procedure.
- And a control parameter T (analog of temperature) and an annealing schedule of changing a temperature-like parameter, so that system can reach its equilibrium.

Appendix B provides pseudocode for the typical Simulated Annealing Algorithm. In application of SA to the current fracture modeling problem, the energy function is the elastic energy function (Equation 4.7), while the fracture model parameters such as position, length and orientation are the quantities that are rearranged in an optimal, low-energy configuration. The goal of the SA application is to find a spatial distribution, or distributions, of fractures that honors their spatial correlation given by Equation 4.7. The first step in the application of SA is to choose the initial set of fracture configuration. Since SA is independent of choice of initial configuration, so we can start with any configuration i.e fractures having length l and orientation θ in a square system of side length L. We start with the calculation of initial energy of the fracture configuration, E_i, using Equation 4.7: The initial temperature, T_i, is chosen at the same order of magnitude as energy function so that acceptance ratio at the start is approximately 99%-100%. In order to change the current configuration of fractures, a fracture j is selected randomly and its length, orientation and/ or position is changed slightly. The algorithms used for for changing the orientation, length and the position are, identical to Masihi et al.(2007),

$$\theta_j^{new} = \theta_j + 0.05\pi(2R - 1) \tag{4.8a}$$

$$l_j^{new} = l_j + 0.5(2R - 1) \tag{4.8b}$$

$$r_j^{new} = r_j + 0.5(2R - 1) \tag{4.8c}$$

where R is a random number selected from a uniform distribution in the range of [0-1]. Once again the energy of new state of the configuration, E_j, is calculated using Equation 4.7. To check the acceptance of new perturbed configuration, E_j, with respect to previous configuration, E_i, the change in energy $\Delta E = E_j$ - E_i is calculated assuming A to be one as it as just scaling factor. If $\Delta E < 0$, then perturbed

configuration is accepted unconditionally and we go back to previous step with $E_i = E_j$. If $\Delta E > 0$, then the new perturbed state is accepted or rejected on the basis of Metropolis algorithm. This means that new state j will be accepted if exp[-(E_j - E_i)/T] > r where r is a uniform random number in the range [0,1]. This allows the algorithm to escape from local minima. This step is performed for 20-30 iterations at a particular temperature where every fracture is visited at every iteration. Then the temperature parameter is changed using the exponential cooling schedule T^{new}=αT^{old} where $\alpha = 0.97$. Here, we take large number of temperature iterations, assuming the function reaches optimal minima of the solution after significantly large number of iterations.

4.3.2 Periodic Boundary Condition (PBC) Implementation

In order to apply SA algorithm, we choose a model of finite size having finite fractures that could image the whole area. Since the model that we have chosen is of finite size, the truncation or the boundaries of the model can introduce artificial effects in the output of final configuration of fractures from SA that are not commonly observed in nature. So, understanding the effect of boundaries on overall configuration of fractures becomes very important. This is because fractures close to the boundary experience different effective stress, hence energy, compare to fractures in the center of the model. Also, while changing the configuration of fractures by perturbing their position some fractures close to the boundary can move out of the model, thus affecting the number density of fractures in the model as shown in Figure 4.1. These limitations can affect our prediction of final configuration of fracture system in an area. So, in order to eliminate these problems, periodic boundary conditions are used by periodically imaging the representative model in whole area. But this may sometime lead to infinite pairs of calculations during the application of SA. So, one of the major concern while applying periodic boundary condition is at what we can truncate calculations without losing accuracy. In most of the cases of use of PBC, either one or two images are used to cover the whole area (Masihi and King, 2007). But this arbitrary choice can either make the algorithm computationally slow or results inaccurate. So here, we proposed a systematic procedure for determining the minimum number of images required to keep the method accurate and computationally fast.

We can establish criteria for determining the maximum distance, and number of

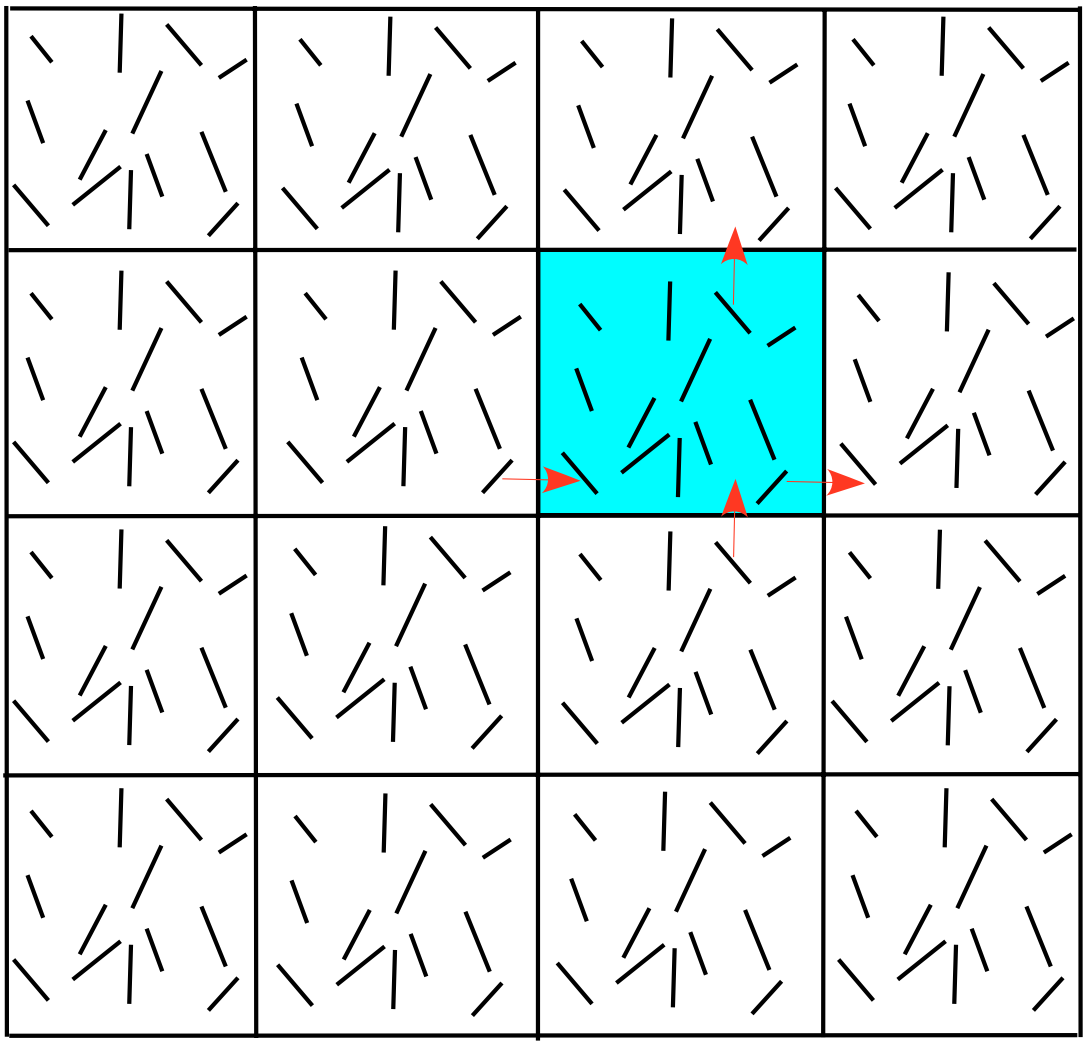

Fig. 4.1. An example of periodic boundary condition for fracture modeling. The arrow shows the simultaneous replacement of fractures in order to maintain the number density of fractures in any cell.

repeated model cells, that must be considered in implementing the PBC in the SA code using a simple test model. This model includes 2500 fractures in a square area 5000 m on each side, each fracture 50 m in length with a random orientation between -30 to +30 degree (Figure 4.2). This model was used to estimate the maximum distance at which significant fracture interaction occurs. In other words, we needed to determine the distance up to which a slight change in fracture configurations influence other fractures or affects the total energy value. The most important factors are relative orientation of fractures and ratio of length of fractures. For detailed analysis, an arbitrary fracture (the first fracture of the test model) was taken and the total initial energy was calculated using Equation 4.9.

$$E_i = \sum_{\substack{l>1 \\ k=1}}^{N} A u_k u_l [\eta |cos(\theta_k - \theta_l)| + |cos(\alpha - \theta_l) cos(\alpha - \theta_k)|] / r_{kl} \tag{4.9}$$

The effect of the orientation of each of the other fractures was then quantified by recomputing the total energy value by rotating a single fracture at r = (100,50), (200,50), (300,50)...(4000,50) etc. one at a time, changing the orientation by 15° (Figures 4.3(a)). The influence of fracture length as a function of the separation between fractures was tested in the same way (Figure 4.3(b)). The results confirm that fractures close to the reference fracture have significantly larger influence than fractures at a distance, which is not surprising given that energy is inversely proportional to distance (Equation 4.9). In fact, fractures at distances larger than r = 1200 m have negligible influence on total energy value. So, for our modeling study the cutoff radius (r_{cutoff}), the distance up to fractures influence each other, is 1200 m. Hence, the number of periodic image at least require for PBC can be calculated as follows: if $r_{cutoff} > a$ then n = r_{cutoff}/a else $n = (r_{cutoff}/a) + 1$, where a is the one side of square representative model and n is the number of model image require to constrain the usage of PBC. So the number of periodic image surrounding the model cell will be equal to n in both side in x- and y- directions in order to neutralize the effect of boundaries of the model cell.

The periodic boundary condition can be implemented by copying enough images of the model to extend to a distance of r_{cutoff} in all directions. Figure 4.4 and Figure 4.5 compares the final configuration of fractures without and with periodic boundary condition generated using simulated annealing algorithm. Figure 4.4(a)

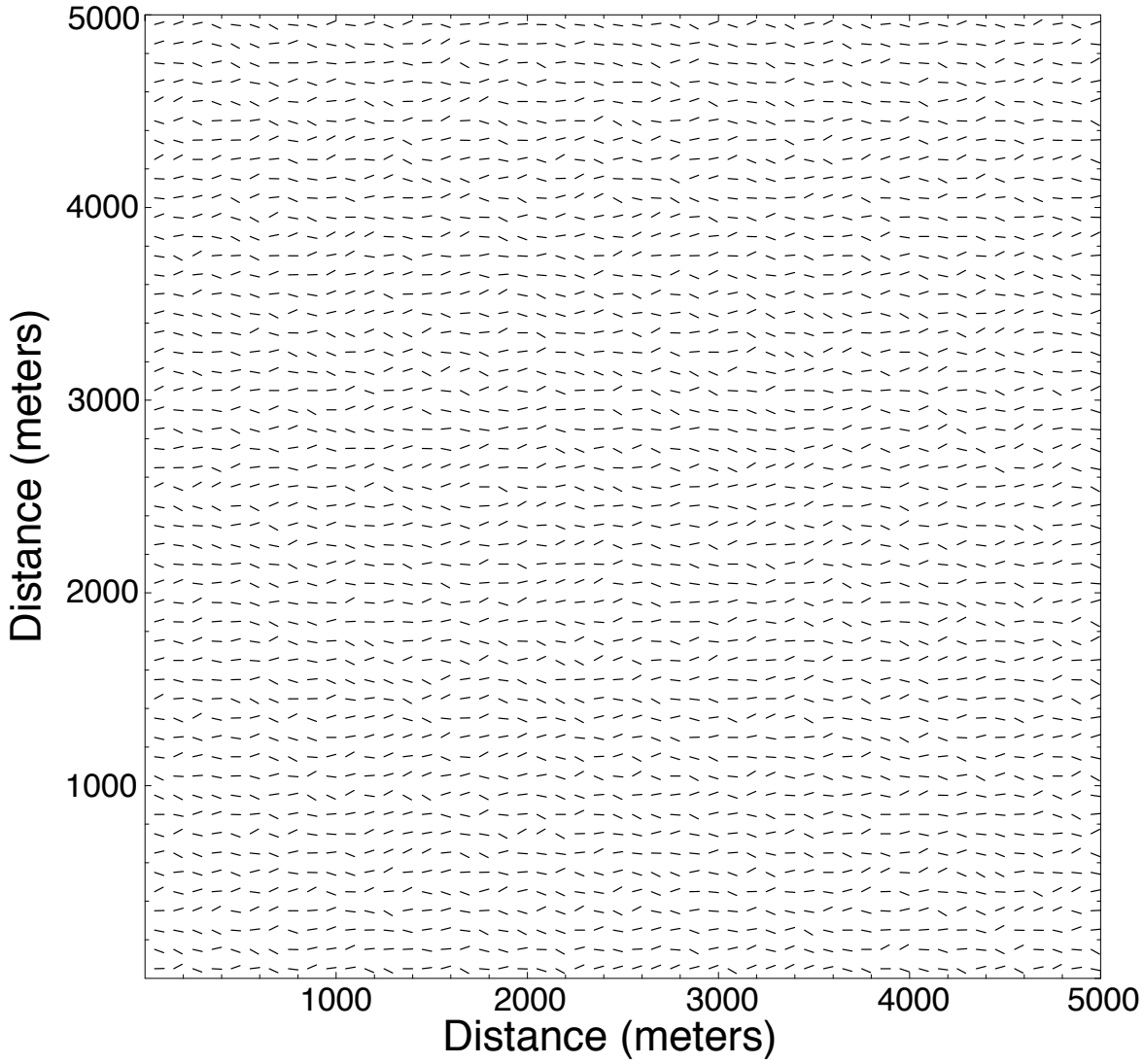

Fig. 4.2. The starting model used for testing factors affecting periodic boundary condition. This model consists of 2500 fractures in a square area with each side=5000 m.

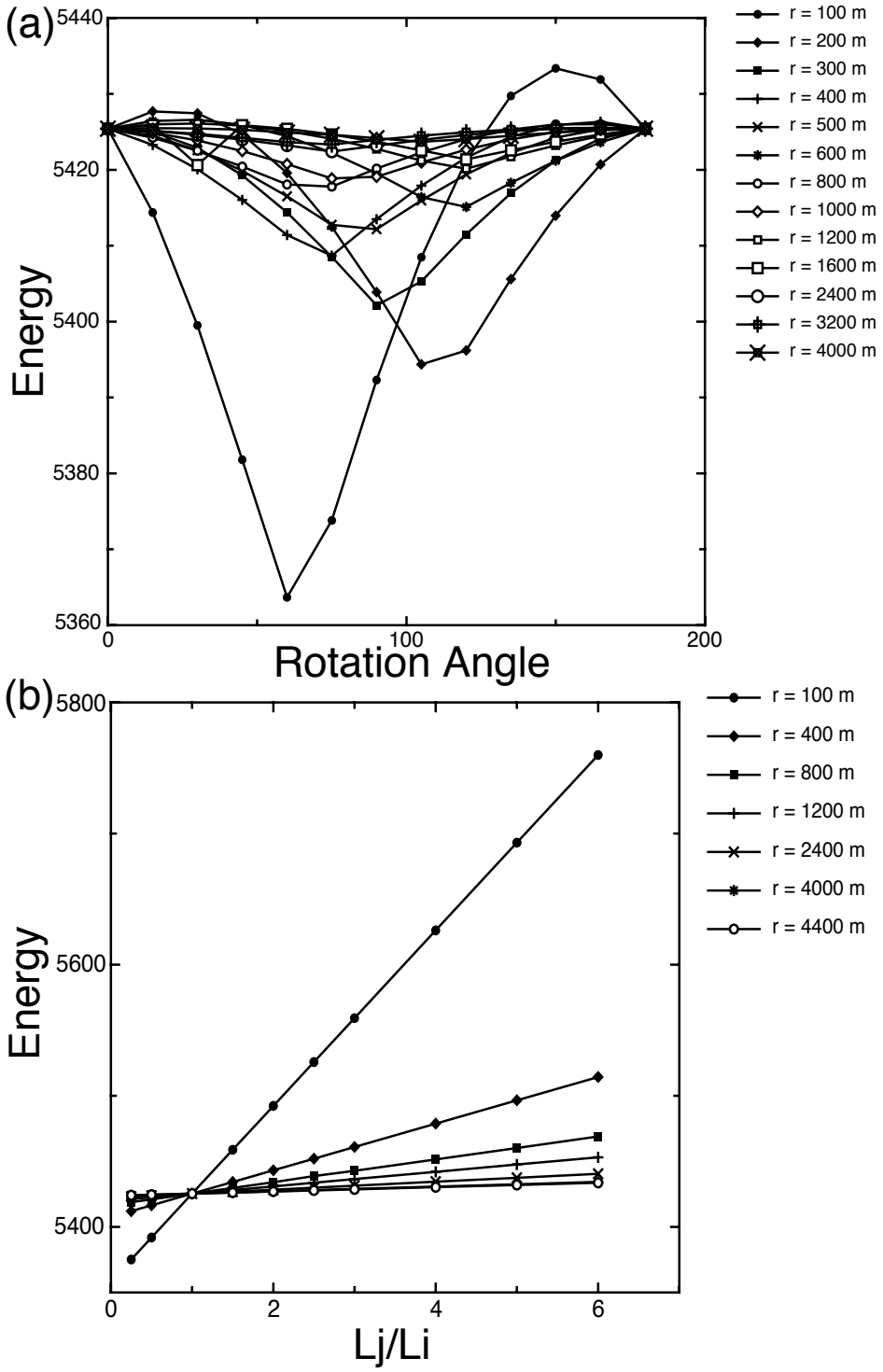

Fig. 4.3. (a) The effect of rotation or relative orientation of fracture on total energy value. Here r represents x-coordinate and y-coordinate=50 m. (b) The effect of relative lengths of fracture on total energy value. Here, Li is the first fracture and Lj is the fracture whose length is changed.

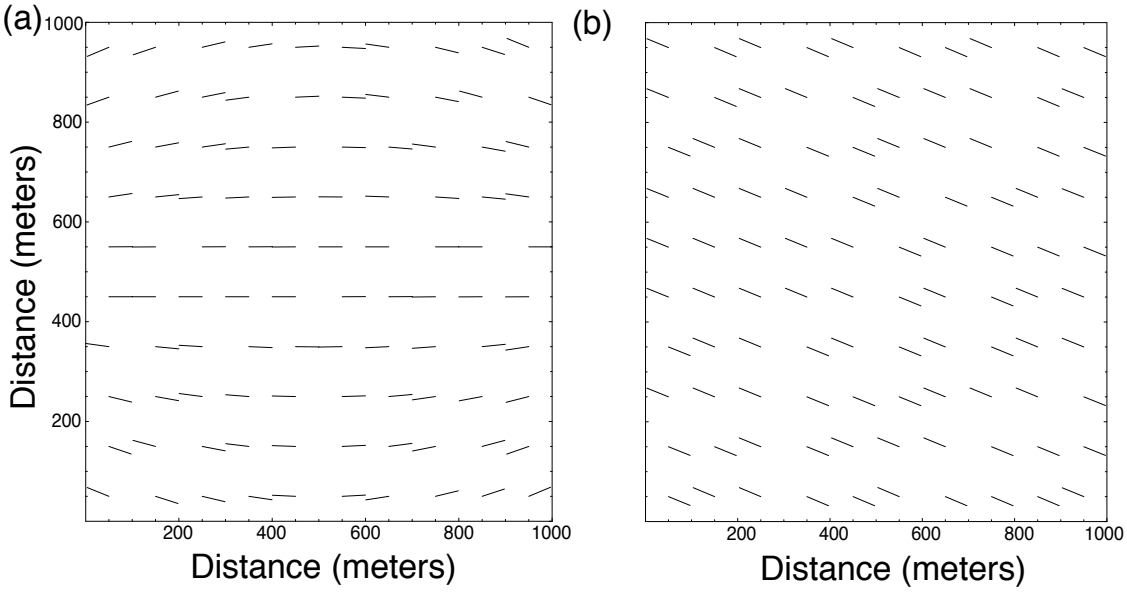

Fig. 4.4. Final configuration of fractures for η = -1 (a) without PBC (b) with PBC.

without PBC shows that fractures near the boundary don't get properly aligned whereas Figure 4.4(b) with PBC shows all fractures becoming parallel to each other. This is because fractures near the boundary experience different stress compare to fractures near the center of the model. However, when we apply PBC, all fractures experience similar stress because of images surrounding the model boundary. Also, if fractures close to the boundary move out of the model cell then their image enter into the model. Thus, the usage of PBC during modeling assures that fracture density remains constant at every realization. We also test the effect of PBC for $\eta = 0.25$ as shown in Figure 4.5. Figure 4.5(d) shows that number of fractures become equal in orthogonal directions using PBC.

4.3.3 Sensitivity of η

The energy function or objective function used to determine the spatial correlation of fractures includes several parameters that control the distribution of fractures. In general, while minimizing the energy function (Equation 4.7), the first cosine term favors orthogonal sets of fractures while second combined cosine term favors parallel and in line fracture configuration. This is because the first cosine term becomes zero

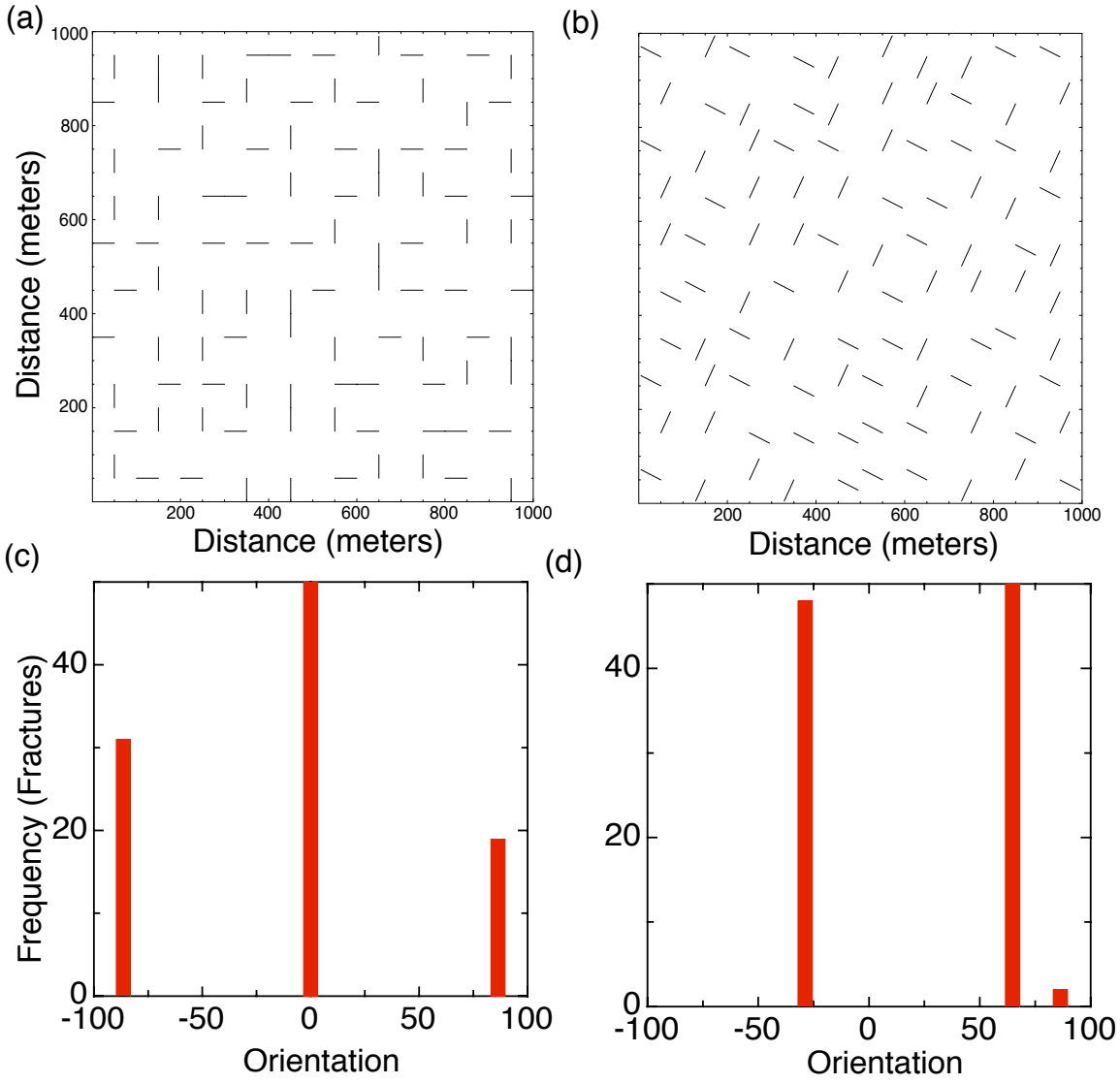

Fig. 4.5. Final configuration of fractures for $\eta = 0.25$ (a) without PBC (b) with PBC. Histogram of final configuration of fractures (c) without PBC (d) with PBC.

for orthogonal set of fractures whereas second cosine term becomes zero for parallel and in line fractures, thus leading to minimization of energy function. The parameter η associated with the first cosine term in the energy function is also very important as it controls the internal configuration of fractured rocks by controlling the behavior of objective function. For example, mathematically it can be observed that energy function for $\eta > 0$ minimizes only when fractures become orthogonal to each other. However for $\eta < 0$, second combined cosine term controls the behavior of energy function that favors parallel and in line fractures. The coefficient η is related to rock properties as η = 3-4ν or $(\lambda+3\mu)/(\lambda+\mu)$ where ν is Poisson's ratio, λ and μ are Lamé parameters that depends on the type of rock sample. Landau and Lifshitz et al. (1982b) suggests that the lower and upper bound for ν as -1 and +0.5 respectively, implies η in the range of [1,7]. This is calculated from mathematical expression (shown below)

$$\sigma = \frac{1}{2}\frac{(3\kappa - 2\mu)}{3\kappa + \mu} \tag{4.10}$$

where σ lies between -1 (for κ=0) and 1/2 (for μ=0). However in reality, Poisson ratio's varies between 0 and 1/2 and there are no known substance for $\sigma < 0$, i.e., substance that would expand transversely when stretched longitudinally. The most common value of Poisson ratio, ν, for subsurface geological rocks are between 0.2 and 0.3 (Engelder and Peacock, 2001). Here, our goal is to test the sensitivity of η on fracture configuration and hence, we consider η from negative to positive values, though negative values are not going to be applicable to field settings in any realistic case.

The starting model for this test is a simple model including 100 fractures in a square box of with sides 1000 m in length. Initially each fracture is 50 m long and are randomly oriented where orientation is chosen uniformly between -30° to +30°. In this initial test, only fracture orientations are allowed to vary. The effect of different values of η after 10000 iterations is shown in Figure 4.6. These results suggest that $\eta > 0$ favors orthogonal sets of fractures whereas $\eta < 0$ favors one set of parallel fractures. This is because η is associated only with first cosine term in energy equation. So for $\eta > 0$, the energy function will be minimized if the second term becomes minimum which is possible only when fractures become orthogonal. Similarly for $\eta < 0$, the energy function will be minimized if the second term becomes maximum which is possible only when fractures become parallel to each other. However, most rocks

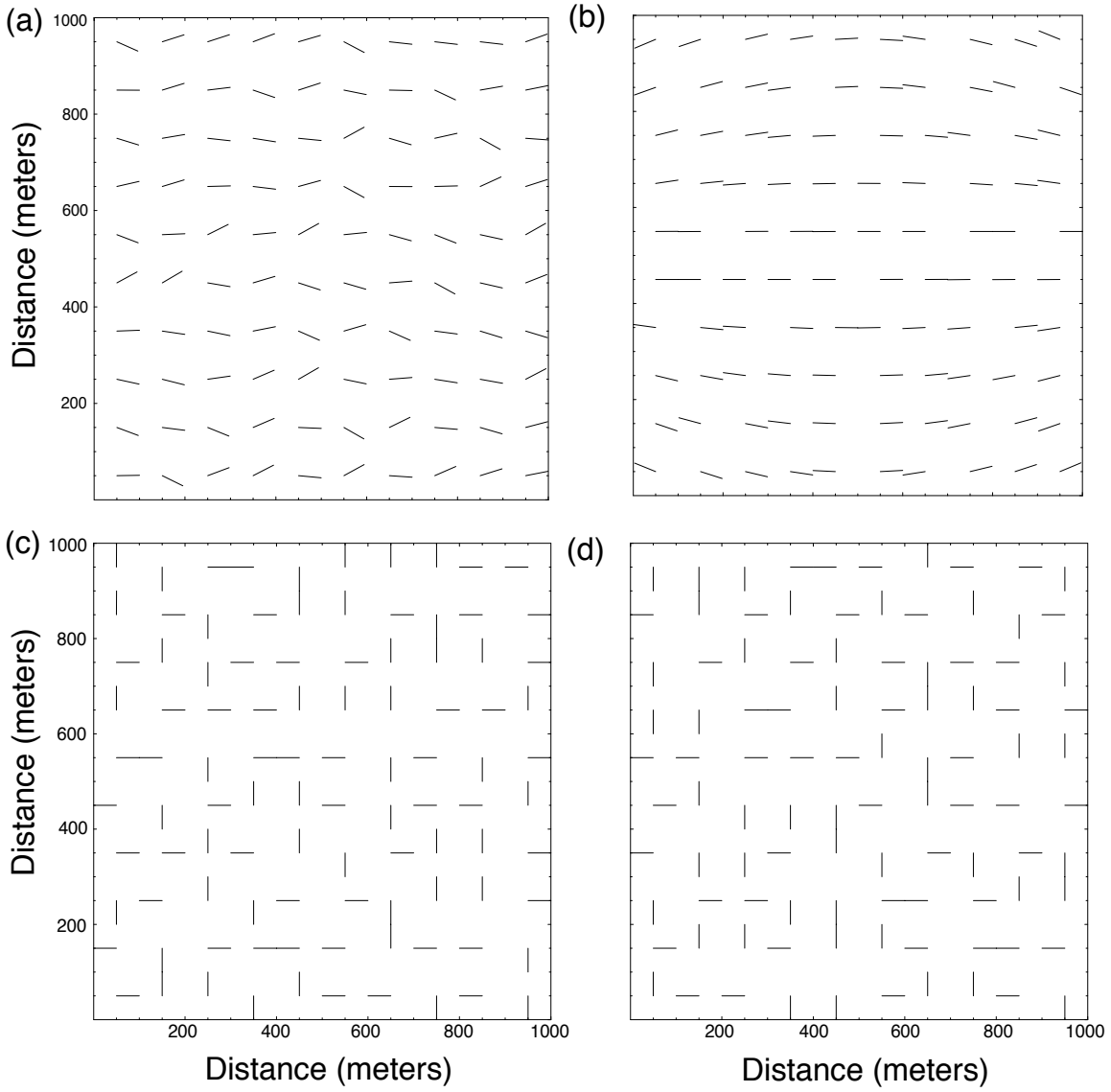

Fig. 4.6. (a) Initial fracture model, and final fracture configurations for (b) η = -1, (c) $\eta = 1$, and (d) $\eta = 2$ respectively.

have $\nu = 0.25$ or $\eta = 2$, so this theory favors dominant existence of orthogonal sets of fractures. This orthogonal feature may seem surprising since the stress field and the material are both isotropic, but it is quite common fractures setting during basin formation. An example of conjugate sets of fracture observed is in Upper Cretaceous (Senonian) Chalk in Kent (Belayneh et al., 2007) where conjugate set of fractures were studied to be formed during basin subsidence.

4.3.4 Sensitivity of Model Parameters

The goal of this section to explain the modeling scheme, understand the sensitivity of model parameters on the objective energy function and their application on field data. The most important model parameters in the objective energy function used for SA algorithm are length, orientation and position of fractures. Any slight change in any of these parameters affect the final configuration of fractures and also the decay of energy function. Here, we study their effects by slightly changing either one parameter or combination of parameters in SA algorithm. In this section, another goal will be to look non-uniqueness in the result and will suggest methods to constrain the model parameters.

We used an initial model containing 100 fractures with lengths selected from a Gaussian distribution (mean 50 m, standard deviation 20 m) to examine these issues (Figure 4.7(a)). The model parameters are perturbed using Equation (4.8). Figure 4.7(b) shows the effect of perturbation of orientation only and orientation and length together on the energy function with change in number of iterations. In accord with general SA study, for the first few iterations at high T, the energy function fluctuates significantly because a large number of perturbations/realizations are accepted, but fluctuations decrease with the increase of number of iterations suggesting large number of rejections of fracture configuration. The energy function becomes stable around 6000 iterations suggesting that the energy function is close to minimum. The fracture model corresponding to these iterations can be taken as one of the realization as several realizations can correspond to same minima; the solution is nonunique. The orientation of fractures of the final output fracture model is not stable, though energy gets minimized, so fractures need to be rotated to match the field data. The histogram of change in orientation after 20000 at 10 successive iterations is shown in Figure 4.8. Figure 4.8 shows that the orientation of fractures

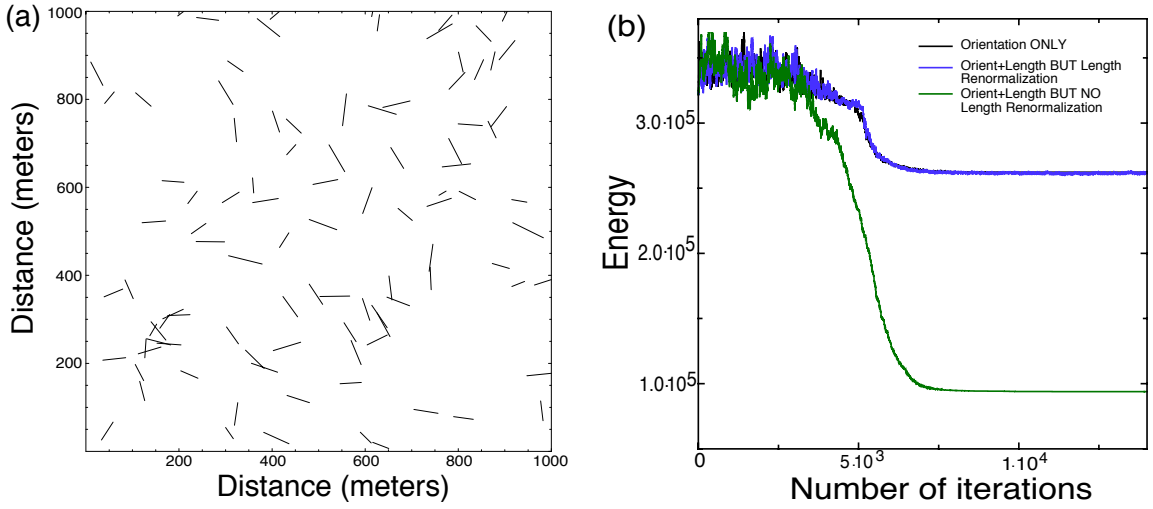

Fig. 4.7. (a) Original model of 100 fractures with Gaussian distribution of length of mean=50 m and std. dev.=20 m (b) Comparison of energy value for different cases after 14000 iterations.

are not stable, even though fractures become orthogonal around 6000 iterations.

Also, if we increase the number of visits to each fracture from 20 to 30 at a particular temperature then the final orientation of the output model doesn't remains same, though fractures become orthogonal and system reaches energy minima in both the cases. Figure 4.9 compares both the cases where the orthogonality of fractures confirm that system is at energy minima. However, the final orientations of fractures are not the same which is another example of non-uniqueness in the result. Hence, the final realization generated using SA algorithm needs to updated corresponding to field data. The other problem of perturbation algorithm (Equation (4.8)(b)) is that successive iterations can make the length of fractures negative which is not possible. Hence, it becomes important to constrain the length of fractures at every iteration. So we decided that the length of fractures at every iteration needs to be renormalized such that the mean length of fractures remains same as field data or initial mean length of the starting model. Also Figure 4.7(b) compares the change in energy function with the number of iterations for cases with and without (but constrained to minimum and maximum fracture length) renormalization to mean length. The figure clearly shows that if the fracture length is renormalized to mean length, the energy function coincides with the case of orientation perturbation only (Figure 4.7(b)) which is expected. Figure 4.7(b) also shows that for the case of orientation and length per-

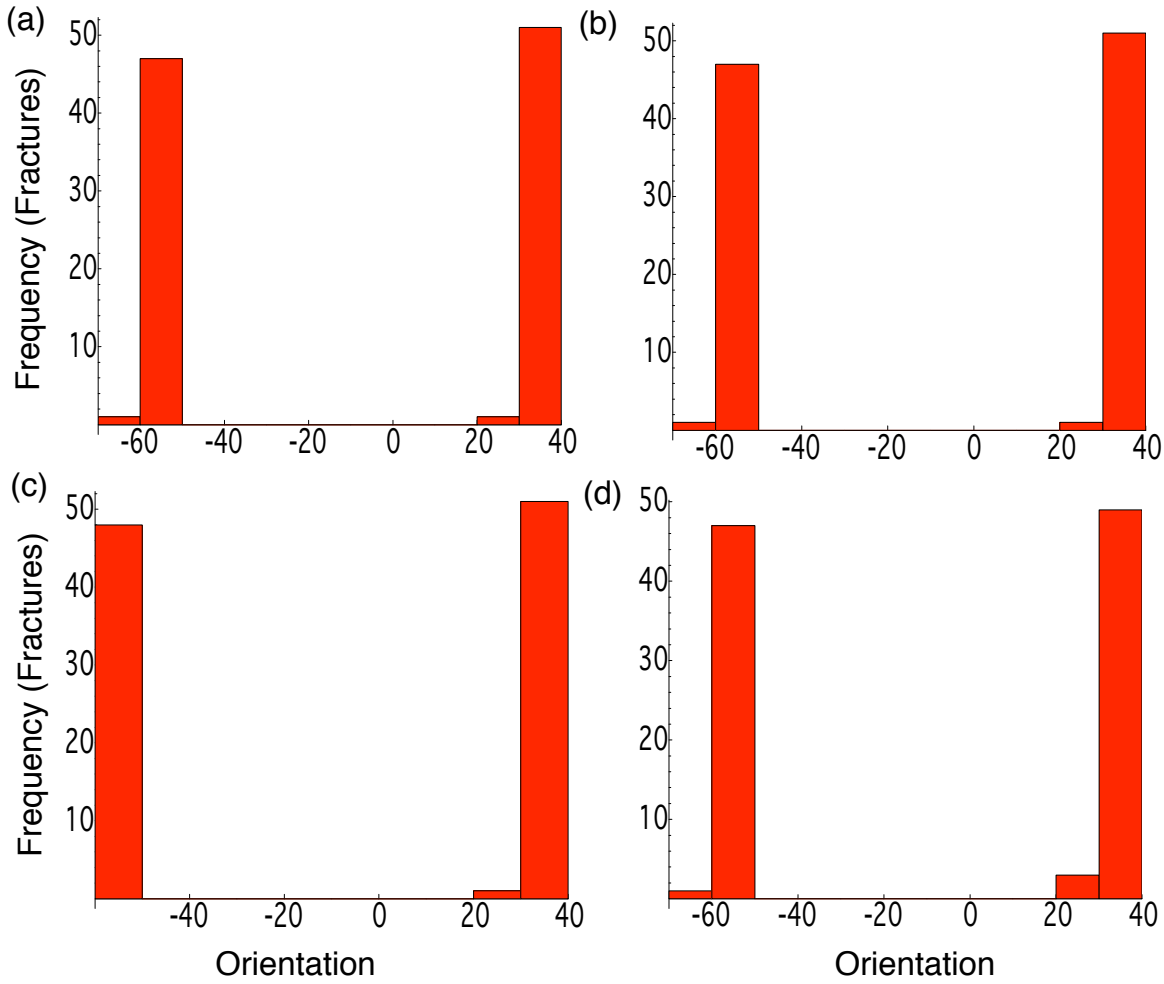

Fig. 4.8. Histogram of orientation of fractures after (a) 20000 (b) 20010 (c) 20020 and (d) 20040 iterations respectively.

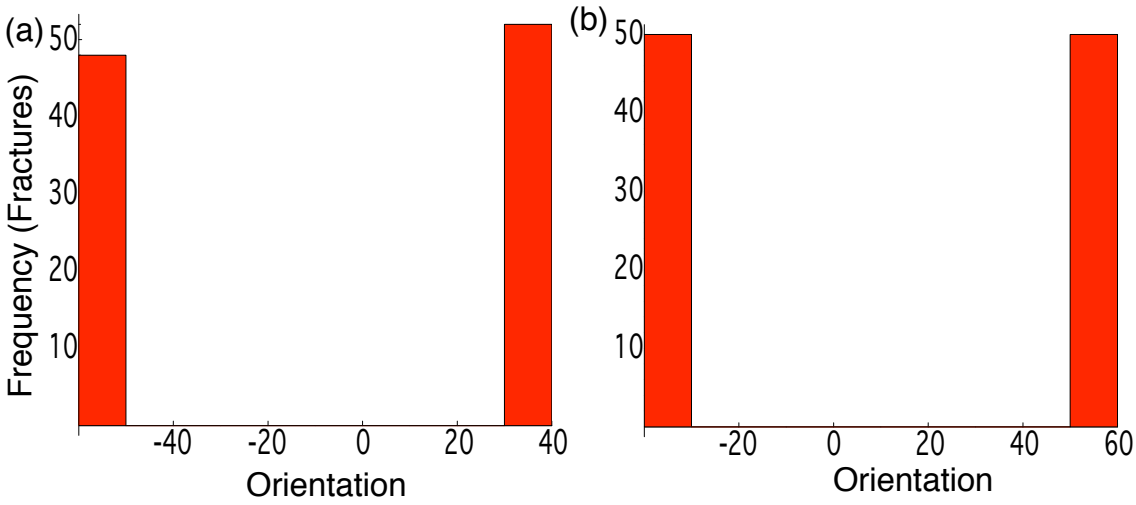

Fig. 4.9. Histogram of orientation of fractures for (a) 20 visits to each fracture (b) 30 visits to each fracture at a particular temperature.

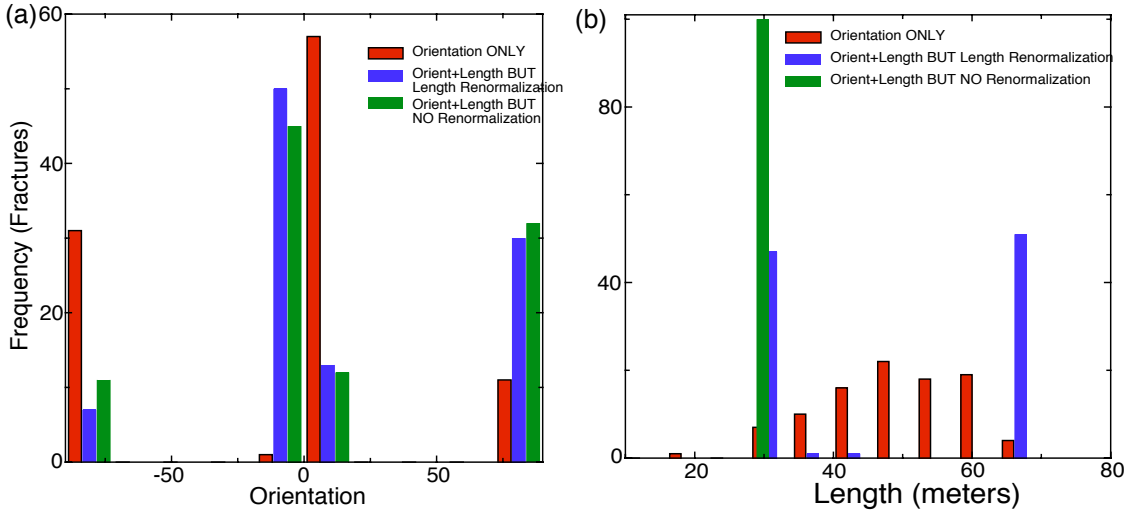

Fig. 4.10. (a) Comparison of final orientation of fractures (b) Comparison of final length of fractures.

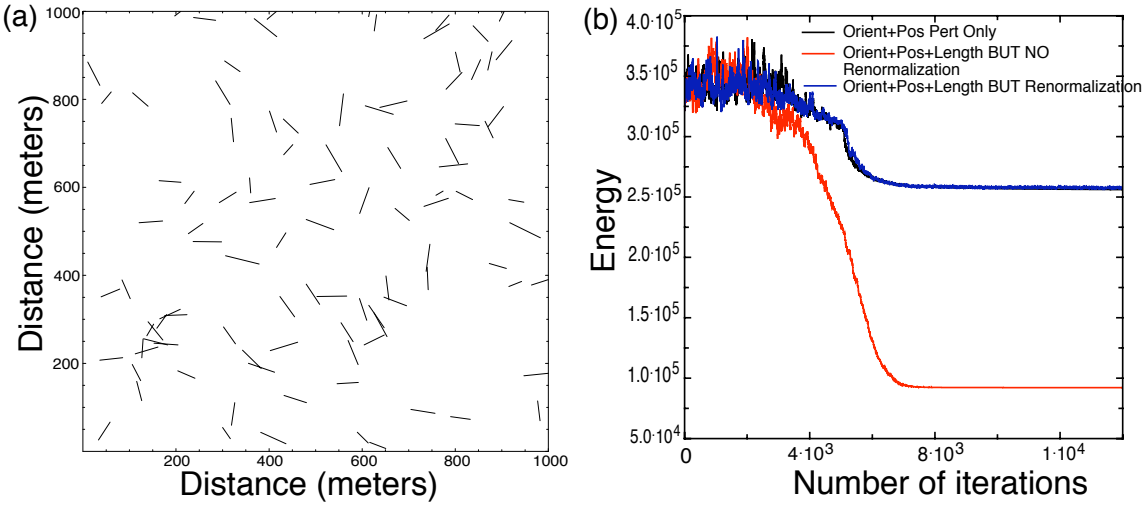

Fig. 4.11. (a) Original model of 100 fractures with Gaussian distribution of length of mean= 50 m and std. dev.= 20 m. (identical to Figure 4.7(a)) Here, position of fractures are also perturbed. (b) Comparison of energy value for different cases.

turbation together without renormalization, the energy function continue decreasing till all fractures reaches minimum length or fractures become unimodal to minimum constrained length. So, if we don't constrain the length of fractures then length of fractures can become negative which will make no sense. Hence, this test shows that the length of fractures needs to be first constrained to minimum and maximum length of fractures and then renormalize to mean length of fractures. Figure 4.10 shows final orientation and length distribution of fractures for all three cases. For the case when length is renormalized, the energy function reaches minima when fractures become bimodal, whereas for the case without renormalization, the energy gets minimized when fractures become unimodal to constrained minimum length.

To study the effect of perturbation of position, a similar study was performed including the perturbation of the position of fractures for the above model. This is important as it can help in restricting the movement of fractures with respect to field data. Figure 4.11 shows the effect of perturbation including position perturbation for the same model and compare different cases. We calculated the total displacement of fractures at every iterations. The histogram of total displacement of fractures at different iterations is shown in Figure 4.12, 4.13, 4.14 and 4.15. Figure 4.12 suggests that the fracture movement is larger at high temperature, ranging from 0.5 m to 40-45 m for first the 2000 iterations. However, as the temperature decreases, the

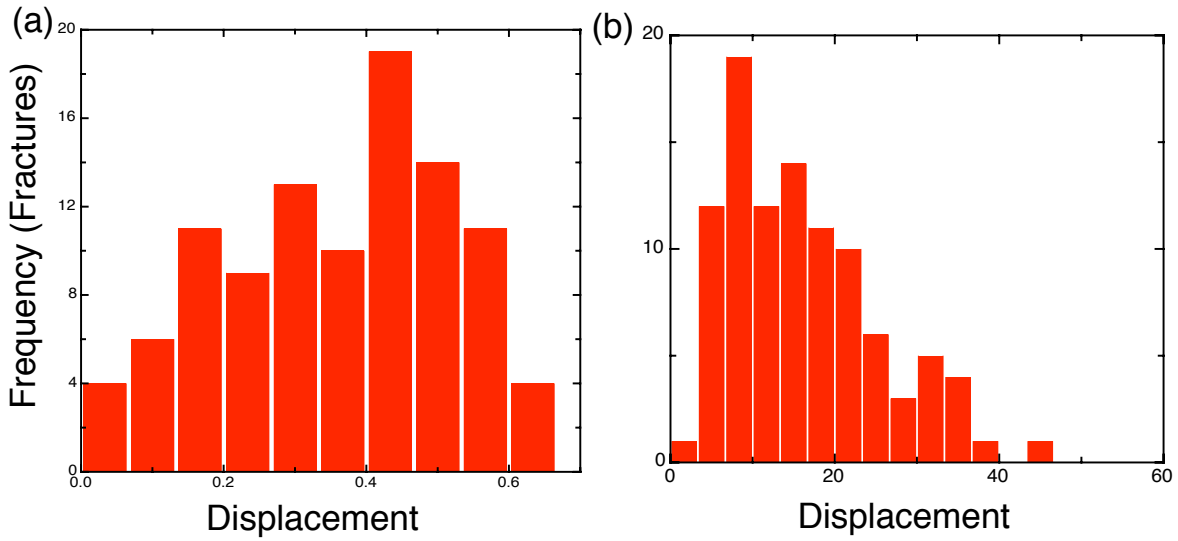

Fig. 4.12. (a) Total displacement after 1st iteration. (b) Total displacement after 2000 iterations.

increase in total displacement also decreases, approx. 0-60 m around 4000 and 6000 iterations (Figure 4.13). For further decrease in temperature as the system tends to equilibrium, the total displacement is constrained to 0-75 m as shown in Figure 4.15. This is analogous to Brownian motion or metal annealing where particle movement decreases with the reduction in temperature.

4.4 Comparison with DFN Models

In this section, our goal is to compare the two different approaches to fracture modeling proposed in this thesis. As already discussed, discrete fracture network (DFN) model is a statistical method which uses location, size, and orientation of fractures collected from field data to generate several stochastic realizations of fractures. However, the other method, proposed in this chapter, generates fractures based on physics of fracturing where fractures are spatially correlated in length, orientation position at every realization. In order to compare them, we generated SA models with a starting model of 3000 fractures, randomly oriented but with starting position the same as in a DFN model. Then we applied simulated annealing, visiting each fracture 30 times at one particular T. At every iteration orientation, length and position of each fracture is changed using the same perturbation algorithm as discussed previously

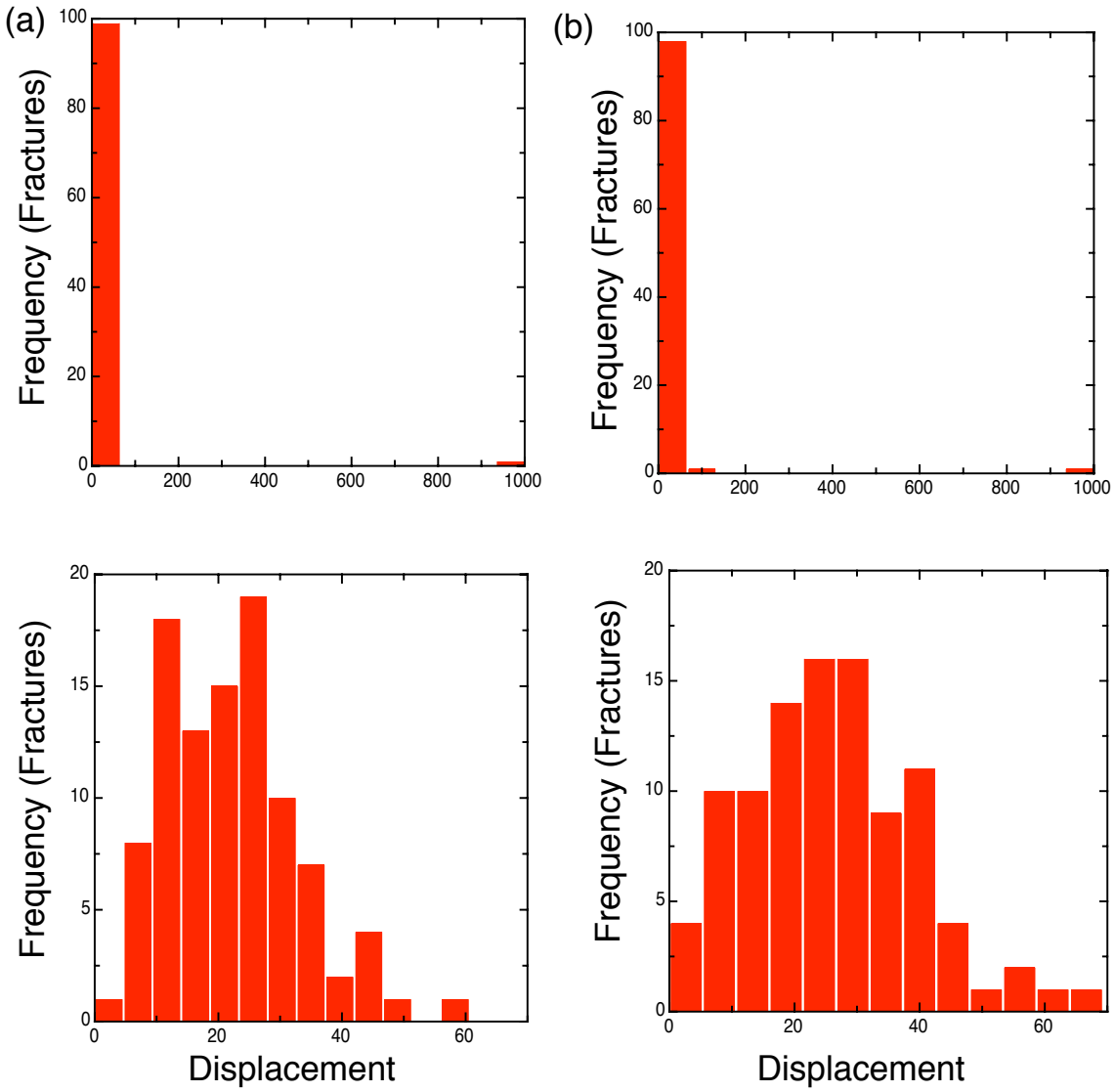

Fig. 4.13. (a) Total displacement after 4000 iterations. Top of (a) is histogram including 1 outlier due to PBC. Bottom of (a) excluding the outlier suggesting the maximum total displacement is 60 m. (b) Total displacement after 6000 iterations. Top of (b) is histogram including 1 outlier due to PBC. Bottom of (b) is excluding the outlier suggesting the maximum total displacement is around 65 m.

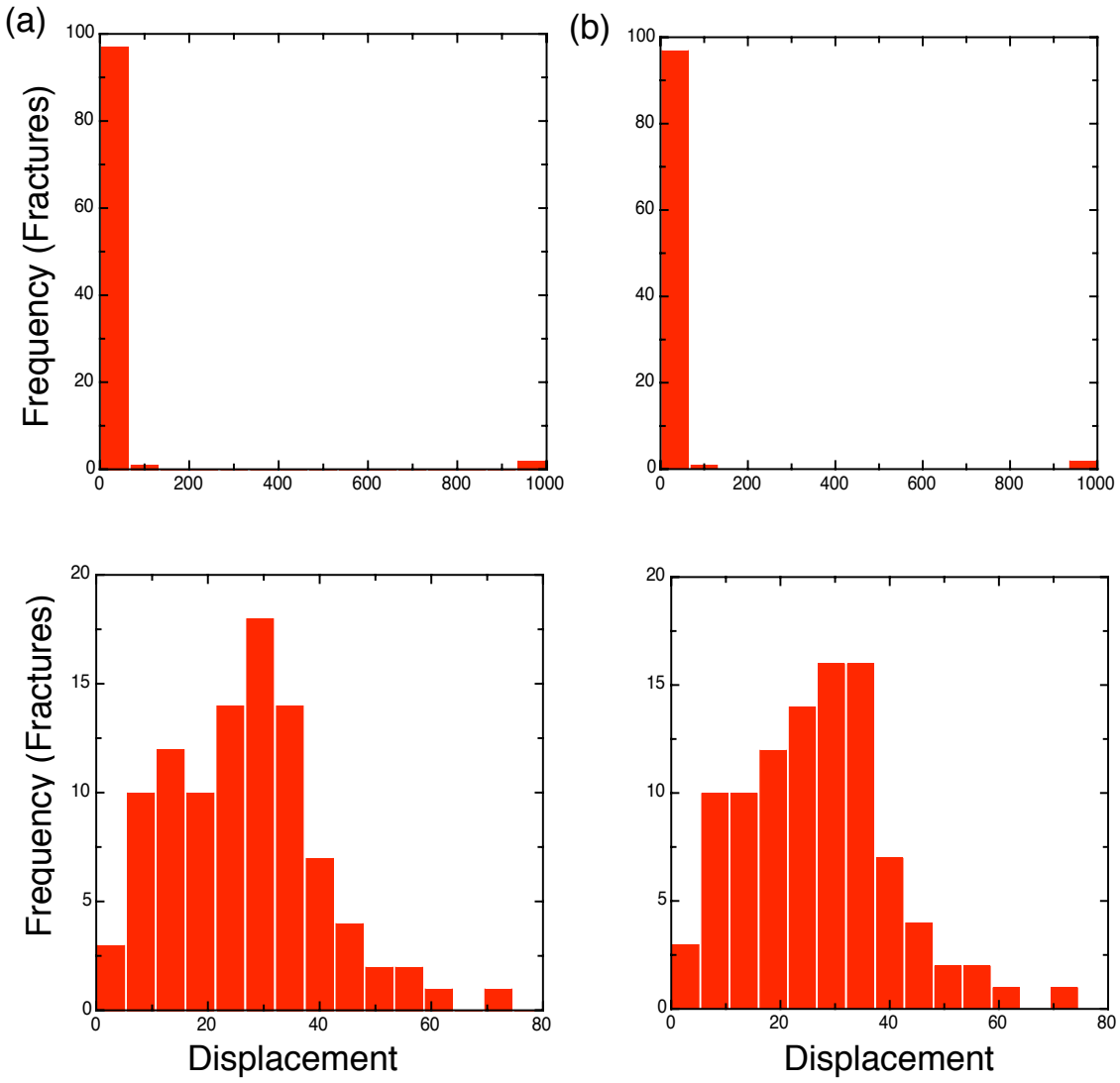

Fig. 4.14. (a) Total displacement after 8000 iterations. Top of (a) is histogram including 1 outlier due to PBC. Bottom of (a) excluding the outlier suggesting the maximum total displacement is 75 m. (b) Total displacement after 10000 iterations. Top of (b) is histogram including 1 outlier due to PBC. Bottom of (b) is excluding the outlier suggesting the maximum total displacement is around 75 m.

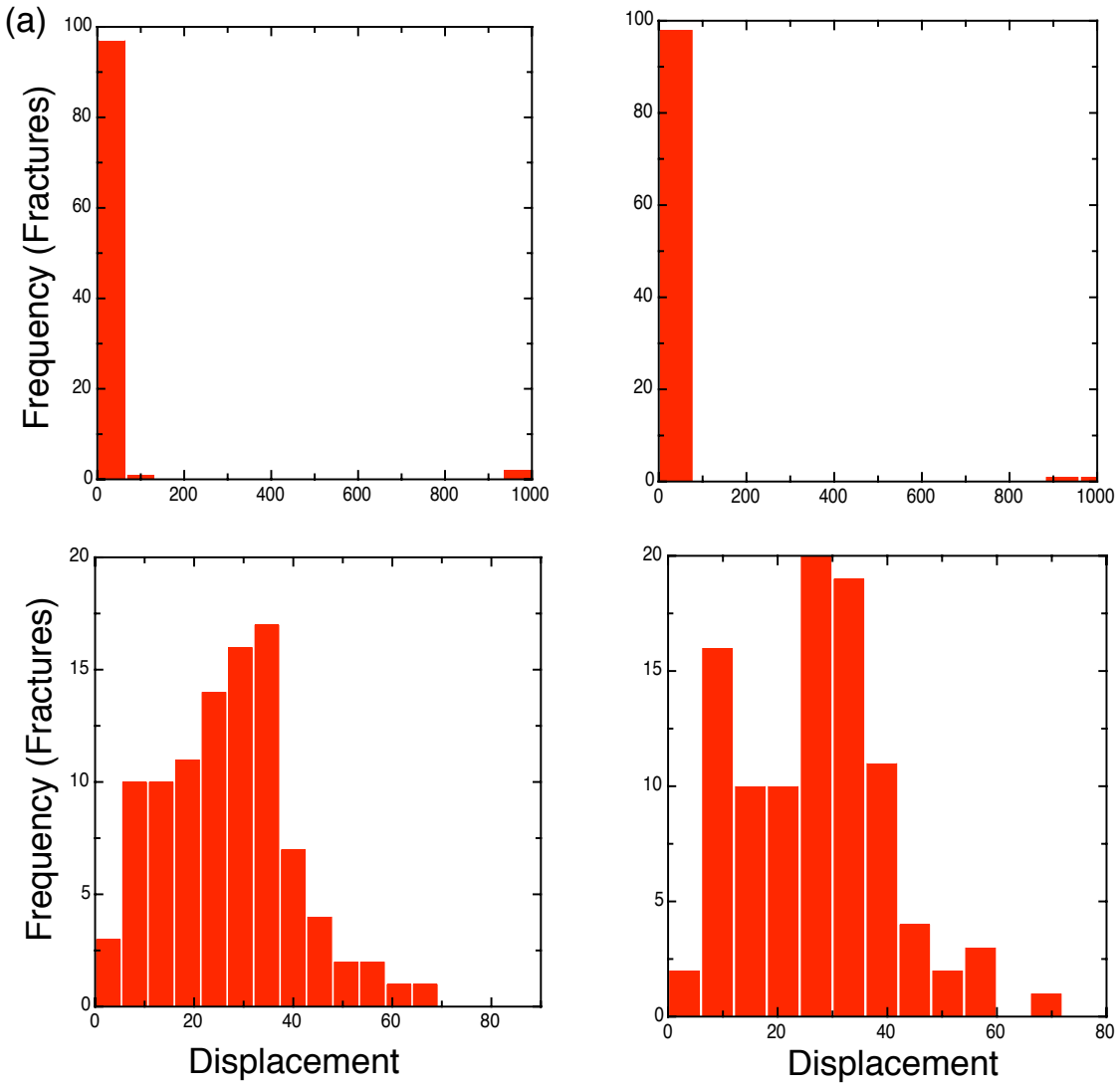

Fig. 4.15. (a) Total displacement after 12000 iterations. Top of (a) is histogram including 1 outlier due to PBC. Bottom of (a) excluding the outlier suggesting the maximum total displacement is 70 m. (b) Total displacement after 14000 iterations. Top of (b) is histogram including 1 outlier due to PBC. Bottom of (b) is excluding the outlier suggesting the maximum total displacement is around 70 m.

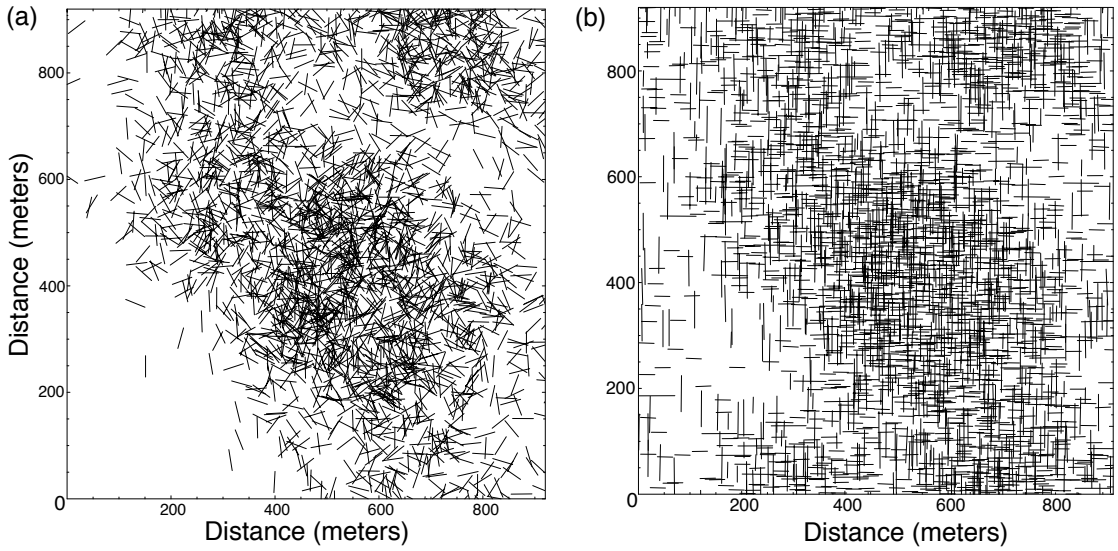

Fig. 4.16. (a) Starting model of 3000 fractures having random orientation to compare DFN model. (b) Final fracture output model after 30,000 iterations.

(Equation (4.8)). Here also we rescaled the length of fractures at each iteration such that the mean length of fracture system remains same as DFN model. Figure 4.16 (a) is the starting model whereas Figure 4.16 (b) is the final orthogonal fracture model after 30000 iterations (1000 T reduction and 30 visits to each fracture at every temperature). Since fractures in the original DFN model (Figure 2.2) are either 45° or 135°, so we rotated final fracture model by 45° to generate another fracture model similar to DFN model (shown in Figure 4.17(a)). Figure 4.17(b) shows the corresponding Energy vs Number of iterations plot.

We tried to compare these two approaches by computing both the fractal dimension and crack density, generated similarly as in DFN model in section 2.4. Fractals are entities that display self-similarity in their geometry such that any portion of the system is the image of whole area on large scale. These fractal entities have fractal dimension that describes the manner in which the fractal entity fills the available Euclidean space. This is consider to be an important tool to study fractures as fractures exhibit scaling behavior ranging from few microns in thin section to thousand of kilometers around faults and form complex patterns (Roy et al., 2007).

Mandelbrot (1983) defines a fractal as an entity for which Hausdroff-dimension (D) strictly exceeds the topological dimension. According to Bonnet et al. (Bonnet et al., 2001), the classical definition of a fractal is given by the number of segments,

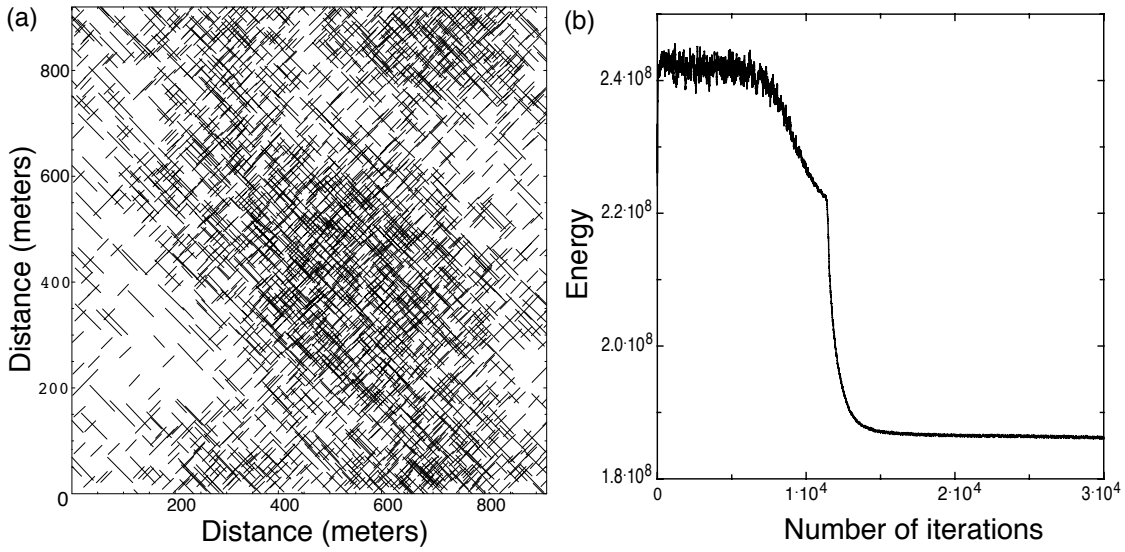

Fig. 4.17. (a) SA output model rotated to 45 degree in order to replicate DFN model. (b) Energy vs Number of iteration curve for simulating 3000 fractures using energy method.

circles, or spheres of dimension d (either 1, 2 or 3) and characteristic length scale r require to cover the part of fractal object included in the volume R^d. The number of circles or sphere required should vary as

$$N(r, R) \approx (R/r)^D \tag{4.11}$$

where D denotes the fractal dimension and which is defined as follows:

$$D = \lim_{r \to 0} \frac{lnN(r)}{ln(1/r)} \tag{4.12}$$

This is the typical box-counting method for which the fractal dimension is obtained even for infinitely small details of the object.

We calculated fractal dimension for both the methods using Equation 4.12. Figure 4.18 shows that the fractal dimension generated by both the methods are very close. This fractal dimension is also in accord with the general field observation for linear features i.e. between 1 and 2. Figure 4.19 compares the crack density or seismic model (section 2.4) generated from both the methods. The seismic model generated using SA algorithm has more highs and spread of crack density compare to seismic model generated using DFN technique as shown in Figure 4.19. The difference is due to change in configuration i.e. length, orientation and position of original fractures

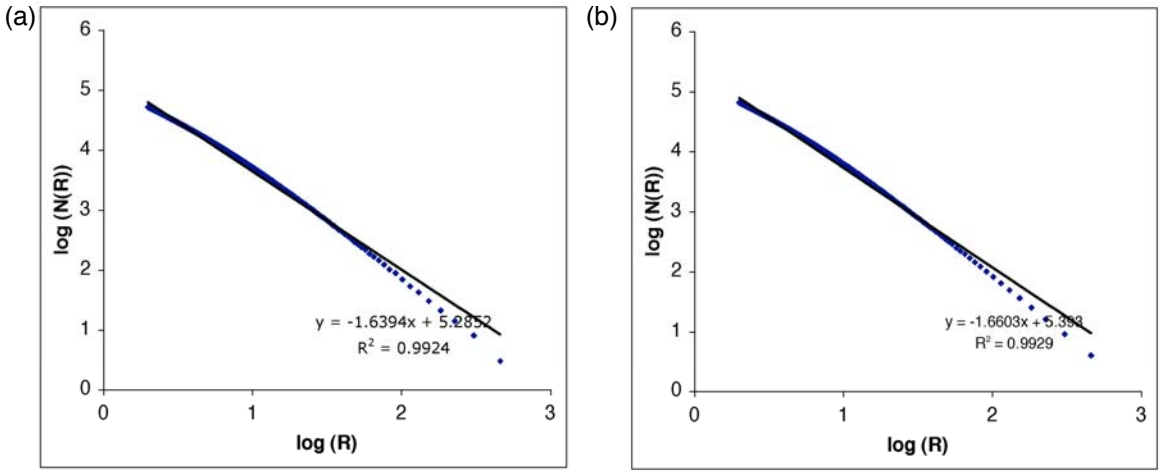

Fig. 4.18. Fractal dimension of (a) DFN model (b) model generated using energy method.

(see Figure 4.16) during SA in order to minimize the energy function to generate optimized fracture model.

4.5 Ray-Born Seismic Modeling

The fracture model generated using simulated annealing algorithm can be further analyzed by computing 3D synthetic seismograms using ray-Born algorithm (Beydoun and Mendes, 1989; Gibson et al., 1993). This method estimates wave fields scattered by small perturbations in the properties of an elastic medium. In our study, velocities and density of overburden layers are assumed to be homogenous. Though this assumption is not valid for true earth but still can be acceptable for time-lapse seismic modeling as properties and geology of overburden layers change very little during hydrocarbon production. In our seismic modeling, the synthetic reservoir model is 920 m×920 m, discretized into smaller cells of 43.8 m×43.8 m for geocellular modeling. The reservoir was assumed to be at depth of 1000 m and to be 20 m thick bounded by homogenous media with velocities V_p=4000 m/s, V_s=2309.6 m/s and ρ=2200 kg/m^3. This 20 m fractured reservoir was assigned 10% porosity and 10 mD permeability (same host rock as in DFN, section 2.4). The reservoir is saturated with 60% oil, 20% brine and 20% gas. There are 90 source-recmandereiver pairs in inline and cross-line direction with 20 m spacing, covering 3D reservoir. We simulated zero-

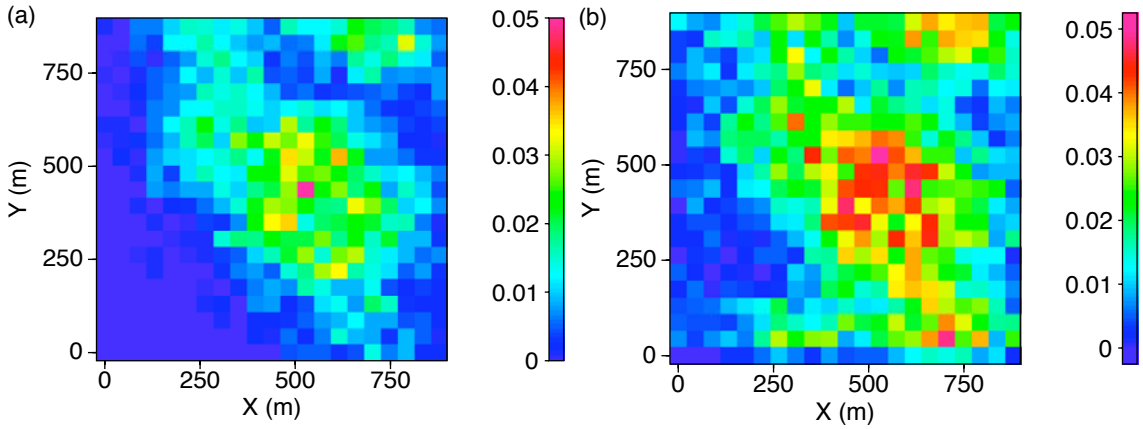

Fig. 4.19. Crack density of (a) DFN model. (b) model generated using energy method.

offset, medium offset and far-offset where the medium offset seismic arrays have 598 m source-geophone offset corresponding to 15° incident angle. The far-offset seismic arrays have 1136 m source-geophone offset corresponding to 30° incident angle. We also applied normal move out (NMO) and phase-shift migration to all the seismogram. Figure 4.20 shows the composite reflection amplitude at zero offset, medium offset and large offset respectively. As expected, the reflection amplitude decreases with increase in incident angle or at far-offset. Similar to our DFN time-lapse modeling, the fracture model generated using physics based stochastic process can be used for time-lapse modeling. Several inlines, crosslines and 2D section (For example, Figure 4.21) can be extracted for detail analysis of the composite reflection amplitudes.

4.6 Conclusions

Our study presents another method of fracture modeling based on physics of fracturing. Several realizations of fractures can be generated based on the assumption that elastic free energy due to fracture density follows Boltzmann distribution. The goal of the new method is to generate several realizations of spatially correlated fracture networks using SA annealing algorithm, update minimum energy realization with field data and predict the flow behavior. The algorithm was further improved by introducing periodic boundary conditions that can enhance the computational speed and accuracy of the algorithm. We also suggested methods of constraining the model parameters in accord to field observations. The fracture model generated using SA

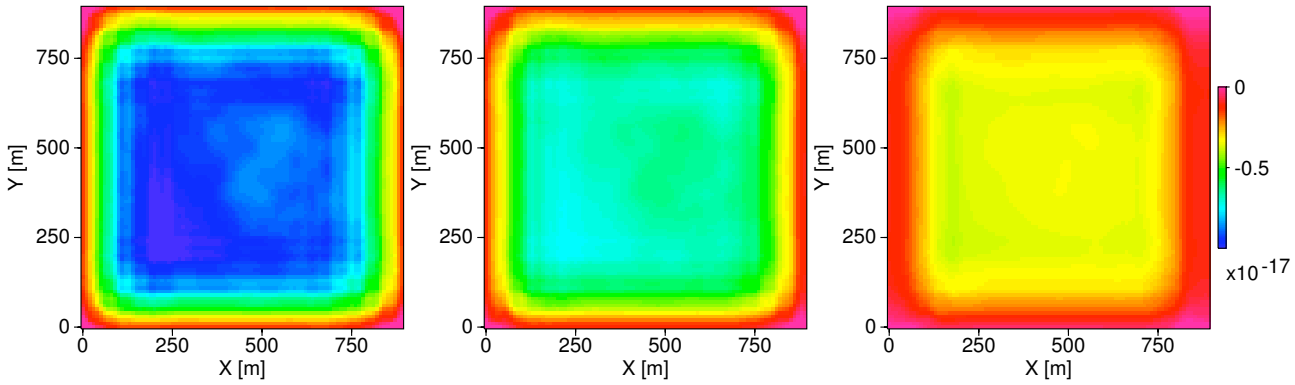

Fig. 4.20. Composite reflection amplitude calculated at zero, medium and far offset respectively (from left to right).

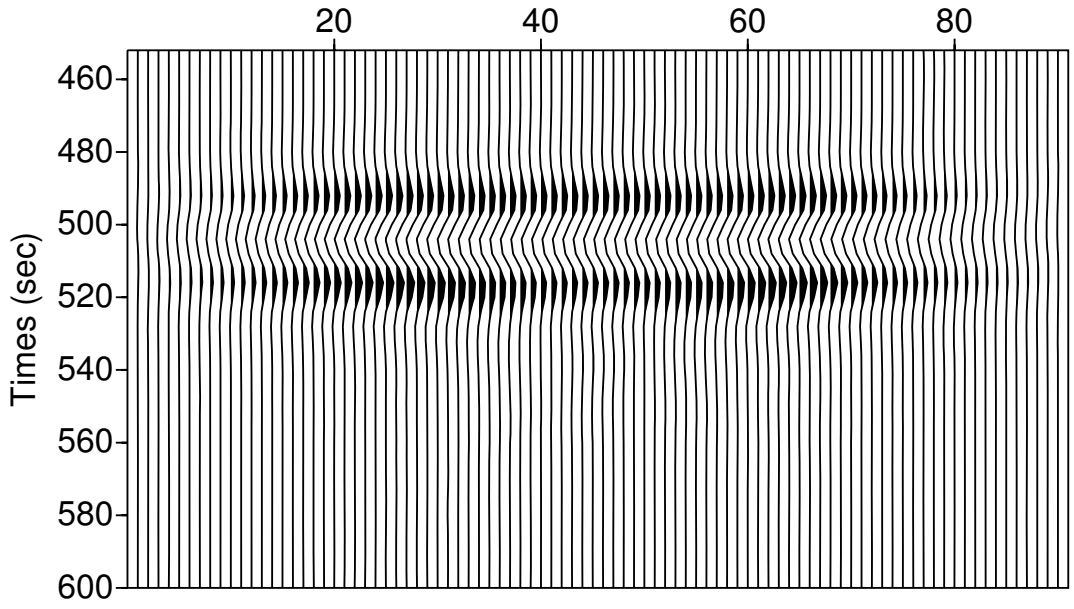

Fig. 4.21. Composite reflection amplitude of 2D seismic section taken diagonally across the 3D fractured reservoir.

can be considered better than DFN as DFN generates realizations based on only statistical distribution of fractures, without any knowledge of physics of fracturing. Also, fractures generated at different realization are not spatially correlated unless statistically constrained. However, the energy constraint used while applying SA algorithm always generate spatially correlated fracture networks. These correlated fracture networks can be used to determine the connectivity of fractures that can help in predicting the flow behavior of the area. Our detail analysis suggests that fractures generated by the isotropic stress field favor orthogonal sets of fractures in most subsurface rocks. We have also shown that this energy based fracture model can also be converted to seismic model, similar to DFN study, that can be further used for synthetic seismic modeling using ray-Born algorithm.

CHAPTER V

CONCLUSIONS

The accurate characterization of fractured reservoirs is of great importance for hydrocarbon production. This is because these fractures control permeability by providing conductive flow paths which can have significant effect on hydrocarbon production especially in low permeable carbonate reservoirs. However, till today most of the study lacks comprehensive knowledge about fracture characterization. Our study proposes methodology to integrate geology, geophysics and reservoir engineering for better characterization of fractured reservoirs. However, our greater interest still exists in developing models relating fracture properties with seismic attributes.

For our modeling study, we used randomly oriented fracture, isotropic reservoirs with a porous background matrix. Our numerical analysis suggests that seismic waves through these fluid saturated fractures undergo significant attenuation and dispersion and attenuation and dispersion of seismic waves depend upon the crack size and permeability of host rock. We have developed methods for relating discrete fracture network models used by engineers to set up fluid flow simulations to models of crack density that can be used to predict seismic reflections from the fractured reservoir. This is an important first step in developing integrated tools for fractured reservoir characterization. AVO results for our example model predict that supercritical carbon dioxide is easier to detect than brine in the fractured reservoirs. The total modeling process is fast and comparatively simple, leading to a prediction of AVO results for comparison to field measurements. Our time- lapse study integrating flow simulation suggest significant change in Q_p, V_p and AVO attributes with change in saturation. The 10% to 12% decrease of intercept with respect to background for SCF CO_2 saturated reservoir shows as potential attribute for detecting fluids in reservoirs. Also, the opposite trend of *differences* of various parameters can be useful in detecting the type of fluids present in the reservoir. Our seismic modeling using ray-Born algorithm suggest significant relative change in amplitude at far-offset that can be useful for AVO analysis. Also, other methods such as instantaneous attributes study suggest Q can be affected even by thin layers and can distinguish fluids in thin and thick reservoirs. We anticipate that this general procedure will have some important applications for

reservoir monitoring studies. Future work should be to apply this methodology to field data, if available, and update the models.

As we know, the knowledge of movement of CO_2 front inside the reservoir is also very important for hydrocarbon production as well as CO_2 sequestration. This becomes more important because of distinctive properties of CO_2 such as low viscosity, low density and its chemical interaction with host rock and other reservoir fluids. We developed a modeling technique that combines comprehensive flow simulation, including chemical processes, with seismic simulations to model the CO_2 injection that includes all the accompanying phase behavior and geochemical effects. The CO_2 dissolution and the acidification triggers a variety of geochemical reactions that can significantly alter the rock-fluid properties. Our modeling shows that intra-aqueous reactions are more significant during injection of CO_2, while slower mineral reactions dominate after pressure equilibrium is achieved. Overall both types of geochemical reactions, intra-aqueous and mineral reactions, cause a change in reflection coefficient of 2 to 5%. So, even though geochemical reactions affect seismic data during CO_2 injection, the seismic signals are dominated by reductions in bulk modulus associated with fluid substitution effects modeled using the Gassmann equation. However, the significant change in various seismic properties at the boundaries because of the continuous chemical activities can be used to detect the flow path of CO_2 inside the reservoirs. The future study should be to develop more complicated models esp. leaky CO_2 reservoir that may show more significant relative change in reflection amplitude for detection even in noisy field data.

We also extended another method of generating fractures developed by Masihi et al. (2007) to more realistic field model. This method is based on physics of fracturing, with assumption that fracture density follows Boltzmann distribution, generates several stochastic realizations of fractures whose statistical distribution can be used for better understanding of the spatial correlation of fractures. Our analysis suggests that the isotropic stress field generates orthogonal sets of fractures in most subsurface rocks. We also propose methodology to convert fracture model to seismic model, similar to DFN study, that can be further used for synthetic seismic modeling using ray-Born algorithm. Future work is to enhance simulated annealing algorithm especially computational speed and improve the method to constrain the model parameters with respect to field data.

REFERENCES

Al-Harbi, M., Cheng, M. H., He, Z., and Datta-Gupta, A., 2004, Streamline-based production data integration in naturally fractured reservoirs: SPE Annual Technical Conference, Houston, Texas, 26-29 September.

Angerer, E., Lanfranchi, P., and Rogers, S. F., 2003, Fractured reservoir modeling from seismic to simulator: A reality?: The Leading Edge, **22**, 684–689.

Bachu, S., 2003, Screening and ranking of sedimentary basins for sequestration of CO_2 in geological media in response to climate change: Environmental Geology, **44**, 277–289.

Balberg, I., Anderson, C. H., Alexander, S., and Wagner, N., 1984, Excluded volume and its relation to the onset of percolation: Phys. Rev. B, **30**, no. 7, 3933–3943.

Batzle, M., and Wang, Z., 1992, Seismic properties of pore fluids: Geophysics, **57**, 1396–1408.

Belayneh, M., Matthai, S. K., and Cosgrove, J. W., 2007, The implications of fracture swarms in the chalk of SE England on the tectonic history of basin and their impact on fluid flow in high-porosity, low permeability rocks: Geological Society, London, Special Publications, **272**, 499–517.

Beretta, M., Bernasconi, G., and Drufuca, G., 2002, AVO and AVA inversion for fractured reservoir characterization: Geophys. Prosp., **67**, 300–306.

Berkowitz, B., 1995, Analysis of fracture network connectivity using percolation theory: Math. Geol., **27**, no. 4, 467–483.

Berkowitz, B., Bour, O., and Odling, N., 2000, Scaling of fracture connectivity in geological formations: Geophys. Res. Lett., **27**, no. 14, 2061–2064.

Beydoun, W. B., and Mendes, M., 1989, Elastic ray-born l_2-migration/inversion: Geophs. J. Int., **97**, 151–160.

Bonnet, E., Bour, O., Davy, P., Main, I., Cowie, P., and Berkowitz, B., 2001, Scaling of fracture systems in geological media: Review of Geophysics, **39**, no. 3, 347–383.

Bour, O., and Davy, P., 1997, Connectivity of random fault networks following a power law fault length distribution: Water Resour. Res., **33**, no. 7, 1567–1583.

——— 1999, Clustering and size distributions of fault pattern; theory and measurements: Geophys. Res. Lett., **26**, no. 13, 2001–2004.

Brown, L. T., 2002, Integration of rock physics and reservoir simulation for the interpretation of time-lapse seismic data at Weyburn Field, Saskatchewan: Ph.D. dissertation, Colorado School of Mines.

Brown, R., 2003, Seismic determination of saturation changes in fractured reservoirs.: 73^{th} Ann. Int. Mtg. Soc. Expl. Geoph, Expanded Abstract., **22**, 1569–1572.

Chapman, M., 2003, Frequency-dependent anisotropy due to meso-scale fractures in the presence of equant porosity: Geophys. Prosp., **51**, 369–379.

Cicirello, V. A., 2008, On the design of an adaptive simulated annealing algorithm: research.microsoft.com/constraint-reasoning/ Workshops/Autonomous-CP07/Papers/2.pdf.

Daly, C., 2001, Stochastic vector and tensor fields applied to strain modelling: Pet. Geosci., **7**, S97–S104.

Darcel, C., Bour, O., Davy, P., and de Dreuzy, R., 2003b, Connectivity properties of two-dimesional fracture networks with stochastic fractal correlation: Water Resour. Res., **39**, no. 10, 1272–1285.

Dershowitz, W., LaPointe, P., Eiben, T., and Wei, L., 2000, Integration of discrete fracture network methods with conventional simulator approaches: SPE, paper 49069, 165–170.

Energy, D. E., 2008, Carbon dioxide sequestration: Carbon dioxide storage: http://www.netl.doe.gov/technologies/carbon_seq/core_rd/storage.html.

Engelder, T., and Peacock, D. C. P., 2001, Joint development normal to regional compression during flexural-flow folding: The lilstock buttress anticline: J. Struct. Geol., **23**, 259–277.

Eshelby, J. D., 1957, The determination of the elastic field of an ellipsoidal inclusion, and related problems: Proc. R. Soc. Lond., **241**, 376–396.

Ganda, S., Bachu, S., and Celia, M., 2004, Spatial characterization of the location potentially leaky wells penetrating a deep saline aquifer in a mature sedimentary basin: Environment Geology, **46**, 707–720.

Gassmann, F., 1951, Elastic waves through a packing of spheres: Geophysics, **16**, 673–685.

Gibson, R. L., Toksoz, M. N., and Batini, F., 1993, Ray-born modeling of fracture-zone reflections in the Larderello Geothermal Field: Geophs. J.Int., **114**, 81–90.

Ha-Dong, M., and Keith, D., 2003, Carbon storage: The economic efficiency of storing CO_2 in leaky reservoirs: Clean. Techn. Environ. Policy., **5**, 181–189.

Harris, J., Nolen-Hoeksema, R., Langan, R., Van Schaack, M., Lazaratos, S. K., and Rector III, J. W., 1995, High-resolution crosswell imaging of a West Texas carbonate reservoir: Part 1 - summary and interpretation: Geophysics, **60**, 667–681.

Heffer, K. J., and King, P., 2006, Spatial scaling of effective modulus and correlation of deformation near the critical point of fracturing: Pure and Appl. Geophys., **163**, no. 10, 2223–2242.

Hepple, R. P., and Benson, S. M., 2005, Geological storage of carbon dioxide as a climate change mitigation strategy: Performance requirements and the implications of surface seepage: Environmental Geology, **47**, 577–585.

Hudson, J. A., 1980, Overall properties of a cracked solid: J. Acoust. Soc. Amer., **87**, 133–150.

——— 1981, Wave speeds and attenuation of elastic waves in material containing cracks: J. Acoust. Soc. Amer., **87**, 133–150.

——— 1986, A higher order approximation to the wave propagation constants for a cracked solid.: Geophys. J. Roy. Astr. Soc., **87**, 265–274.

Hudson, J. A., Liu, E., and Crampin, S., 1996, The mechanical properties of materials with interconnected cracks and pores: Geophys. J. Int., **124**, 105–112.

Kumar, A., Datta-Gupta, A., Shekhar, R., and Gibson, R. L., 2008, Modeling time lapse seismic monitoring of CO_2 sequestration in hydrocarbon reservoirs including compositional and geochemical effects: Petroleum Science and Technology (in press).

Landau, L. D., and Lifshitz, E. M., 1982b, Theory of elasticity: Pergamon, London.

Li, Y. K., and Nghiem, L. X., 1986, Phase equilibria of oil, gas and water/brine mixtures from a cubic equation of state and Henry's law: Can. J. Chem. Eng., **64**, 486–496.

Lin, L., and Phair, R., 1993, AVO tuning: 63rd SEG meeting, Washington, DC, Expanded Abstracts, 727-730.

Liu, E., Hudson, J. A., and Pointer, T., 2000, Equivalent medium representation of fractured rock: J. Geophys. Res., **105**, 2981–3000.

Macbeth, C., and Lynn, H., 2000, Applied seismic anisotropy: Theory, background, and field studies.: Soc. Expl. Geophys., **20**, 676–681.

Mandelbrot, B. B., 1983, The fractal geometry of nature: W. H. Freeman.

Masihi, M., and King, P. R., 2007, A correlated fracture networks: Modeling and percolation properties: Water Resour. Res., **43**, W07439.

Masihi, M., King, P. R., and Nurafza, P., 2005, Fast estimation of performance in fractured reservoirs using percolation theory: SPE Paper 94186, 1–12.

Mavko, G., Mukerji, T., and Dvorkin, J., 2003, The rock physics handbook: Tools for seismic analysis of porous media.: Cambridge University Press.

Mavko, G., and Nur, A., 1975, Melt squirt in the asthenosphere: J. Geophys. Res., **80**, 161–178.

Nghiem, L., 2002, Compositional simulator for carbon dioxide sequestration: Computer Modeling Group Ltd.

——— 2003, Compositional simulator for carbon dioxide sequestration - Part 2: Computer Modeling Group Ltd.

Nolen-Hoeksema, R., Wang, Z., Harris, J., and Langan, R., 1995, High-resolution crosswell imaging of a West Texas carbonate reservoir: Part 5 - core analysis: Geophysics, **60**, 712–726.

Peacock, S., and Hudson, J. A., 1990, Seismic properties of rocks with distributions of small cracks: Geophs. J.Int., **102**, 471–484.

Pérez, M., Gibson, R., Yu, and Toksoz, M., 1999, Detection of fracture orientation using azimuthal variation of P-wave AVO responses: Geophysics, **64**, 1253–1265.

Pointer, T., Liu, E., and Hudson, J. A., 2000, Seismic wave propagation in cracked porous media: Geophys. Prosp., **49**, 509–522.

Rathore, J., Fjaer, E., Holt, R. M., and Renlie, L., 1991, Acoustic anisotropy in synthetics with controlled crack geometry: 53rd EAGE meeting, Florence, Italy, Expanded Abstracts, **53**, 538–539.

——— 1995, P- and S- wave anisotropy of a synthetic sandstone with controlled crack geometry: Geophys. Prosp., **43**, 711–728.

Reichl, L. E., 1998, A model course in statistical physics: John Wiley and Sons, Inc.

Robinson, P. C., 1984, Numerical calculations of critical densities for lines and planes: J. Phys. A Math. Gen., **17**, no. 14, 2823–2830.

Roy, A., Perfect, E., Dunne, W. M., and McKay, L. D., 2007, Fractal characterization of fracture networks: An improved box-counting technique: Journal of Geophysical Research, **112**, no. B12201, 1–9.

Schoenberg, M., 1980, Elastic wave behavior across linear slip interfaces.: J. Acoust. Soc. Amer., **68**, 1516–1521.

Schoenberg, M., and Sayers, C. M., 1995, Seismic anisotropy of fractured rock: Geophysics, **60**, 204–211.

Shuey, R., 1985, A simplification of the Zoeppritz equations: Geophysics, **50**, 609–614.

Stumn, W., and Morgan, J. J., 1996, Aquatic Chemistry: Chemical equilibria and rates in natural waters: John Wiley and Sons, Inc.

Taner, M., Koehler, F., and Sheriff, R. E., 1979, Complex seismic trace analysis: Geophysics, **44**, 1041–1063.

Thomsen, L., 1986, Elastic anisotropy due to aligned cracks; theoretical models: Eos. Trans. Am. Geophys. Un., **67**, 1207.

——— 1995, Elastic anisotropy due to aligned cracks in porous rock.: Geophys. Prosp., **43**, 805–829.

Tod, S., 2001, The effects on seismic waves of interconnected nearly aligned cracks.: Geophys. J. Int., **146**, 249–263.

Tran, N. H., 2007, Simulated annealing technique in discrete fracture network inversion: Optimizing the optimization: Comput. Geosci., **11**, 249–260.

Tsang, C.-F., Beson, S. M., Kobelski, B., and Smith, R. E., 2002, Scientific considerations related to regulation development for CO_2 sequestration in brine formations: Environmental Geology, **42**, 275–281.

Vargaftik, N., 1975, Tables of thermophysical properties of liquid and gases: John Wiley and Sons.

Wang, Z., Cates, M. E., and Langan, R. T., 1998, Seismic monitoring of a CO_2 flood in a carbonate reservoir: A rock physics study: Geophysics, **63**, 1604–1617.

Zhu, P., Wang, J., Yu, W., and Zhu, G., 2004, Inverting reservoir crack density from P-wave AVOA data.: J. Geophys. and Engg., **1**, 168–175.

APPENDIX A

EQUANT POROSITY

Hudson et al. (1996) tried to studies the effect of the overall properties of a cracked solid having connections between isolated cracks with small-scale porosity within the solid material where the size of pores is an order of magnitude smaller than the cracks. In such solids, the pressure within the crack is relieved due to diffusion from the crack into matrix rather than flow from cracks to cracks. Such kind of model is called as Equant Porosity Model (Thomsen, 1986). The derivation of dimesionless parameters for this model are as follows:

Using D'Arcy's law and conservation of fluid mass, the porosity ϕ_m within the matrix must satisy the diffusion equation

$$\frac{\partial}{\partial_t} = \nabla.(\rho_f D_m \nabla p_f) \tag{A.1}$$

where ρ_f is the local fluid density and p_f is the pressure, while D_m is the coefficient of diffusion relating the volume flux to the pressure gradient within the porous matrix. For mathematical simplicity, it was assumed that ϕ_m remains constant i.e. we neglected the effect of stress and fluid pressure on ϕ_m. Also, Equation 8 from Hudson et al. (1996) suggest that the relative increase of the volume of the fluid above its volume in the unstressed state is related to fluid pressure as

$$\frac{\rho_o}{\rho_f} - 1 = -p_f/k_f \tag{A.2}$$

where ρ_o is the density of unstressed fluid and k_f is the bulk modulus of the fluid. Substituting above equation into Equation A.1, we can get

$$\frac{\phi_m}{k_f}\frac{\partial p_f}{\partial_t} = D_m \nabla^2 p_f \tag{A.3}$$

Also, the diffusion was assumed to be linear away from a crack face in the plane $x_3 = 0$. So, for such cases if the time variations are harmonic, then fluid pressure p_f within the matrix satisfies

$$p_f = p_c exp\{-(1+i)qx_3 + i\omega t\} \tag{A.4}$$

where

$$q^2 = \frac{\omega\phi_m}{2k_f D_m}, q > 0 \tag{A.5}$$

and p_c is the fluid pressure in the crack. The mass flow into the crack of circular radius a, is

$$\dot{m}_c = 2\pi a^2 D_m \rho_f \left.\frac{\delta p_f}{\delta x_3}\right|_{x_3=0} = -2(1+i)\pi a^2 q D_m \rho_c p_c \tag{A.6}$$

where ρ_c is the fluid density in the crack.

Now the next step is to calculate the relationships between crack- opening displacements and fluid density, mass and pressure. Here, one important point to note is that only the axial stress σ_{33} gives rise to changes of volume of the crack and the corresponding crack-opening displacement is given as (Hudson, 1981),

$$[u_3] = \frac{a}{\mu}\sigma_{33}^{\infty} U_{33}(r) \tag{A.7}$$

where σ_{33}^{∞} is the value of the axial stress at infinity and r is the distance from the center of the crack. The corresponding change in the volume of the crack, upto the first order is,

$$\delta V_c = \int_{S_c} [u_3] dS = \frac{a}{\mu}\sigma_{33}^{\infty} \int_{S_c} U_{33}(r) dS, \tag{A.8}$$

where S_c is the plane face of the crack.

Hence, the corresponding change in density, $\delta\rho_c$, is given by

$$\frac{\delta\rho_c}{\rho_o} = \frac{\delta m_c}{m_o} - \frac{\delta V_c}{V_o} \tag{A.9}$$

to the first order, where ρ_o, m_o, V_o are the properties in unstressed equilibrium. Also, we have

$$\frac{\delta\rho_c}{\rho_o} = \frac{p_c}{k_f} \tag{A.10}$$

From above two equations, we can simplify to

$$\frac{p_c}{k_f} = \frac{\delta m_c}{m_o} - \frac{\delta V_c}{V_o} \tag{A.11}$$

and substitution of δm_c from Equation A.6 and δV_c from above results in

$$\frac{-p_c}{k_f} = \frac{3a}{4\pi c\mu}\sigma_{33}^{\infty}\bar{U}_{33} + \frac{3(1-i)qD_m p_c}{2c} \tag{A.12}$$

where

$$\bar{U}_{33} = \frac{1}{a^2}\int_{S_c} U_{33}(r)dS \tag{A.13}$$

Using the result of dry crack from Eshelby et al. (1957), we have

$$U_{33}(r) = \frac{2}{\pi}\left(\frac{\lambda+2\mu}{\lambda+\mu}\right)(1-r^2/a^2)^{1/2}(1+p_c/\sigma_{33}^{\infty}) \tag{A.14}$$

and so integrating over S_c, we get

$$\bar{U}_{33} = \frac{4}{3}\left(\frac{\lambda+2\mu}{\lambda+\mu}\right)\left(1 - \frac{(3ak_f/4\pi c\mu)\bar{U}_{33}}{(1+3(1-i)k_f qD_m/2c)}\right) \tag{A.15}$$

Finally rearranging the terms we get,

$$\bar{U}_{33} = \frac{4}{3}\left(\frac{\lambda+2\mu}{\lambda+\mu}\right)/(1+K), \tag{A.16}$$

where K is,

$$K = \frac{1}{\pi}\frac{a}{c}\frac{k_f}{\mu}\frac{4}{3}\left(\frac{\lambda+2\mu}{\lambda+\mu}\right)/[1+3(1-i)J/2c] \tag{A.17}$$

and

$$J^2 = \omega\phi_m k_f D_m/2, J > 0 \tag{A.18}$$

The second crack parameter, $\bar{U_{11}}$, which appears in overall elastic parameters is unaffected by interconnections between pores as shear stress applied to a crack face does not give rise to a volume change.

APPENDIX B

SIMULATED ANNEALING PSEUDOCODE

Simulated annealing is a stochastic optimization method used in variety of problems involve finding optimum values of a function consisting of large number of independent variables. The following pseudocode implements (Cicirello, 2008) standard Simulated Annealing algorithm starting from initial state S continued till maximum, i_{max} steps. The neighbor state S is selected randomly and metropolis algorithm is used to decide whether to accept or reject the new state. The exponential annealing schedule is used for this algorithm.

$S \leftarrow$ **GenerateInitialState**

$T \leftarrow$ Some Initial High Temperature, T_o

for i from 1 to i_{max}

  $S^{'} \leftarrow$ **PickRandomState(Neighborhood(*S*))**

  if Energy$(S^{'}) <$ **Energy** (S)

    $S \leftarrow S^{'}$ {Note: accepting a move}

  else

    $r \leftarrow$ **Random**(0,1)

    if $r <$ exp{(**Energy**(s) - **Energy**$(s^{'})$)/T}

      $S \leftarrow S^{'}$ {Note: accepting a move}

    end

  end

$T \leftarrow T_o.\alpha^i$

end

This pseudocode refers to general SA algorithm where PickRandomState refers to a function that randomly selects the neighborhood state, Energy at a particular state refers to value of objective function at that particular state, and α represents the temperature reduction factor.

APPENDIX C

DERIVATION OF OBJECTIVE ENERGY FUNCTION

According to Masihi and King et al. (2007), a fracture is defined as discontinuity in the displacement vector in the elastic medium. So, any displacement vector is assumed to have continous part (elastic displacement u^e) and a discontinous part (the inelastic displacement u^i) that can acts as a source for inelastic strain. Similarly, strain and stress can be decomposed into elastic and inelastic parts,

$$e_{ij} = e^e_{ij} + E_{ij} \text{ and } \sigma_{ij} = \sigma^e_{ij} + S_{ij} \tag{C.1}$$

If the system is in mechanical equilibrium i.e. in the absence of any external body forces, the equation of continuity becomes,

$$\partial_j \sigma_{ij} = \partial_j \sigma^e_{ij} + \partial_j S_{ij} = 0 \text{ or } \partial_j \sigma^e_{ij} = -\partial_j S_{ij} \tag{C.2}$$

Since the system is in equilibrium, the inelastic part of stress becomes the fictitious input driving force that gives rise to displacement and fracturing and also keeps fractures open, From Heffer and King et al. (2006), the total elastic energy per unit volume required to keep fractures open is the work done by elastic forces on the total strain which includes elastic and inelastic strain. This total elastic energy is given by equation C.3

$$E = \frac{1}{2}\sigma^e_{ij}\epsilon^e_{ji} \tag{C.3}$$

The definition of elastic strain in fourier domain is given as

$$\epsilon^e_{ji} = \frac{i}{2}\Big(u^e_i k_j + u^e_j k_i\Big) = \frac{i}{2}\Big(\delta_{aj}\delta_{il} + \delta_{ai}\delta_{jl}\Big)k_a u^e_l \tag{C.4}$$

where u_i and u_j is the displacement at i and j locations and k_i and k_j is the wavenumber associated with displacements at respective locations.

Similarly, the stress can be written as

$$\sigma^e_{ij} = i\lambda_{ijal} k_a u^e_l \tag{C.5}$$

where λ_{ijal} is the standard isotropic elasticity tensor, related to Lamé constants, λ and μ, by

$$\lambda_{ijal} = \lambda\delta_{ij}\delta_{al} + \mu(\delta_{ia}\delta_{jl} + \delta_{il}\delta_{ja}) \tag{C.6}$$

Contracting above terms together leads to an expression for the elastic energy given as

$$\begin{aligned} E(\mathbf{k}) &= \frac{1}{2}[(\lambda+\mu)k_k k_l + \mu k^2\delta_{kl}]u_k^e(\mathbf{k})u_l^e(-\mathbf{k}) = \frac{1}{2}\mu[k^2\delta_{kl} + \frac{1}{1-2\nu}k_k k_l] \\ &= \frac{\mu}{2}L_{kl}(\mathbf{k})u_k^e(\mathbf{k})u_l^e(-\mathbf{k}) \end{aligned} \tag{C.7}$$

where L_{kl} is the usual linear operator of isotropic elasticity and is the inverse of the Green's function, $L_{kl}G_{lm} = \delta_{km}$

Here, we will use the hypothesis that the frequency distribution of strain energy due to the displacements/dislocations or fractures follows Boltzmann Law

$$p(E) \propto exp(-E/ < E >) \tag{C.8}$$

Assuming the fracture system to be ergodic in nature i.e. equiprobable existence of all possible energy states, Boltzmann Distribution Law can be written as

$$\begin{aligned} p(E(\mathbf{k})) &= Z^{-1}exp\Big(-\frac{E(\mathbf{k})}{< E >}\Big) \\ &= Z^{-1}exp\Big(-\frac{\mu}{2 < E >}L_{kl}(\mathbf{k})u_k^e(\mathbf{k})u_l^e(-\mathbf{k})\Big) \end{aligned} \tag{C.9}$$

where Z is the normalization for the possible existence in different energy states.

Hence, the probability distribution of fluctuations about equilibrium using equation C.9 can be given as

$$p(E(\mathbf{u})) = Z^{-1}exp\Big(-\frac{\mu}{2 < E >}\mathbf{L} : \mathbf{uu}\Big) \tag{C.10}$$

Using Einstein Fluctuation Theory ((Reichl, 1998), pg 350-351) about equilibrium, assuming linear translation fluctuation is given as $\mathbf{h}.\mathbf{u}$, the more general form of integral is represented as,

$$\mathbf{I} = Z^{-1}\int_{-\infty}^{\infty} D\mathbf{u}exp\Big(-\frac{\mu}{2 < E >}\mathbf{L} : \mathbf{uu} + \mathbf{h}.\mathbf{u}\Big) \tag{C.11}$$

Here Z is partition function, hence it holds following relationship from Boltzmann's

law,

$$\begin{aligned} Z &= \int_{-\infty}^{\infty} D\mathbf{u} exp\Big(- \frac{\mu}{2 < E >} \mathbf{L} : \mathbf{uu} \Big) = 1 \\ &= \int_{-\infty}^{\infty} du_1 du_2 du_3 ..... du_n exp\Big(- \frac{\mu}{2 < E >} \sum_{\substack{1 \le k \le n \\ 1 \le l \le n}} L_{kl} u_k u_l \Big) \end{aligned} \tag{C.12}$$

Also, $\mathbf{L}$ is symmetric matrix, hence it can be diagonalized using an orthogonal matrix, $\mathbf{O}$ such that $\mathbf{O}.\mathbf{L}.\mathbf{O^T} = \Gamma$ where $\mathbf{\Gamma}$ is diagonal ($\Gamma_{ii} = \gamma_i$ and Γ_{ij}=0 for $i \neq j$) (Reichl et al.,pg 187-188) and equation C.12 can be rewritten as,

$$\int_{-\infty}^{\infty} du_1 du_2 .... du_n exp\Big(- \frac{\mu}{2 < E >} \mathbf{L} : \mathbf{uu} \Big) = \int_{-\infty}^{\infty} d\alpha_1 d\alpha_2 d\alpha_3 ..... d\alpha_n exp\Big(- \frac{\mu}{2 < E >} \sum_{1 \le i \le n} \gamma_i \alpha_i^2 \Big) \tag{C.13}$$

where $\det(\mathbf{L}) = \gamma_1 \gamma_2 ... \gamma_n$ and $\alpha = \mathbf{O}.\mathbf{u} = (\alpha_1, \alpha_2, ... \alpha_n)$.

Using infinite integrals properties $\int_{-\infty}^{\infty} exp(-ax^2) dx = \sqrt{(\frac{\pi}{a})}$ where a>0, it can be shown from Equation C.12 and Equation C.13 that $Z^{-1} = \sqrt{\frac{\mu \gamma_1 \gamma_2 ... \gamma_n}{(2\pi < E >)^n}} = \sqrt{\frac{\mu det(\mathbf{L})}{(2\pi < E >)^n}}$.

Similarly, equation C.11 can be rewritten as

$$\begin{aligned} \mathbf{I} &= Z^{-1} \int_{-\infty}^{\infty} du_1 du_2 .... du_n exp\Big(- \frac{\mu}{2 < E >} \mathbf{L} : \mathbf{uu} + \mathbf{hu} \Big) \\ &= \int_{-\infty}^{\infty} exp\Big(- \frac{\mu}{2 < E >} \gamma_1 \alpha_1^2 + h_1 \alpha_1 \Big) d\alpha_1 \int_{-\infty}^{\infty} exp\Big(- \frac{\mu}{2 < E >} \gamma_2 \alpha_2^2 + h_2 \alpha_2 \Big) d\alpha_2 ..... \\ &\quad ..... \int_{-\infty}^{\infty} exp\Big(- \frac{\mu}{2 < E >} \gamma_n \alpha_n^2 + h_n \alpha_n \Big) d\alpha_n \end{aligned} \tag{C.14}$$

Using the identity $\int_{-\infty}^{\infty} exp(-ax^2) exp(2bx) dx = \sqrt{\frac{\pi}{a}} exp(\frac{b^2}{a})$ where a>0 and Z, it can be shown that the most general integral equation C.14 can be written as

$$\mathbf{I} = exp(\frac{< E >}{2\mu} L_{kl}^{-1} h_k h_l). \tag{C.15}$$

Also the joint moment identity,$< x_i, x_2, ..x_n >$ for jointly distributed stochastic variables is given as

$$< x_i, x_2, ...x_n > = \lim_{k_1 \to 0} ..... \lim_{k_n \to 0} (-i)^n \frac{\partial}{\partial k_1} ..... \frac{\partial}{\partial k_n} f_{x_1 ....., x_N}(k_1, ..., k_N) \tag{C.16}$$

where $f_{x_1 ....., x_N}(k_1, ..., k_N)$ is the jointly distributed characteristic function for stochas-

tic variables ((Reichl, 1998), pg 186)

Similarly, the correlation or second moment between two fractures located at k and l is given as

$$\begin{aligned} C_{kl}(\mathbf{k}) &= < u_k(\mathbf{k}) u_l(-\mathbf{k}) > = \lim_{\mathbf{h}\to 0} \frac{\partial}{\partial h_k} \frac{\partial}{\partial h_l} [\mathbf{I}] \\ &= \lim_{h_k \to 0} \lim_{h_l \to 0} \frac{\partial}{\partial h_k} \frac{\partial}{\partial h_l} \Big[\frac{< E >}{2\mu} \Big(L_{kk}^{-1} h_k^2 + 2 L_{kl}^{-1} h_k h_l + L_l^{-1} h_l^2) \Big] \\ &= \frac{< E >}{\mu} L_{kl}^{-1}(\mathbf{k}) = \frac{< E >}{\mu} G_{kl}(\mathbf{k}) \end{aligned} \tag{C.17}$$

In real space, correlation function (equation C.17) is given as,

$$C_{kl}(\mathbf{r}) = \frac{< E >}{\mu} G_{kl}(\mathbf{r}) \tag{C.18}$$

From Landau and Lifshitz ((1982b), pg 115), Green's tensor in an isotropic medium is given as

$$G_{kl}(\mathbf{r}) = \frac{1}{16\pi\mu(1-\nu)r} \{ (3-4\nu)\delta_{kl} + \mathbf{n_k} \mathbf{n_l} \} \tag{C.19}$$

where,
r is the radius vector of displacement vector from k to l i.e. $r = \|\mathbf{r_k} - \mathbf{r_l}\|$,
$\mathbf{n_k}$ is unit vector in k direction i.e. direction of displacement $= \frac{\mathbf{r_k}}{r}$
$\mathbf{n_l}$ is unit vector in l direction i.e. direction of displacement $= \frac{\mathbf{r_l}}{r}$

Hence, using Equation C.19 into Equation C.18, the correlation between two fractures is given as,

$$\begin{aligned} C_{kl}(\mathbf{r}) &= \frac{< E >}{\mu} G_{kl}(\mathbf{r}) \\ &= \frac{< E >}{16\pi\mu(1-\nu)} \Big(\frac{(3-4\nu)\delta_{kl}}{r} + \frac{\mathbf{r_k} \mathbf{r_l}}{r^3} \Big) \end{aligned} \tag{C.20}$$

So, basically $C_{kl}(\mathbf{r})$ represents second moment tensor of each displacement with

respect to the origin of force. We can rewrite Equation C.20 as,

$$\begin{aligned} C_{kl}(r) &= A(r)r_k r_l + B(r)\delta_{ij} \\ A(r) &= \frac{D}{r^3}, \\ B(r) &= \frac{(3-4\nu)D}{r}, \\ D &= \frac{< E >}{16\pi\mu(1-\nu)}, \end{aligned} \tag{C.21}$$

which is the necessary conditions for determining covariance tensor between two vectors separated by r in an isotropic vector field (Daly et al. (2001)).

Daly et al. (2001) shows that in any isotropic vector field, the covariance between two vectors $\mathbf{u_k}$ and $\mathbf{u_l}$, separated by $\mathbf{r}$, having component relationship shown in equation C.21 can be rewritten as

$$C_{kl}(\mathbf{r}) = Cov(\mathbf{u_k}(\mathbf{r}), \mathbf{u_l}(-\mathbf{r}))$$

$$C(\mathbf{r} : \mathbf{u_k}, \mathbf{u_l}) = A(\mathbf{r})(\mathbf{r}, \mathbf{u_k})(\mathbf{r}, \mathbf{u_l}) + B(\mathbf{r})(\mathbf{u_k}, \mathbf{u_l})$$

substituting A, B and C from above

$$\begin{aligned} &= \frac{D}{r^3}(\mathbf{r}, \mathbf{u_k})(\mathbf{r}, \mathbf{u_l}) + \frac{(3-4\nu)}{r}\frac{D}{r}(\mathbf{u_k}, \mathbf{u_l}) \\ &= \frac{D}{r}\Big[\eta(\mathbf{u_k}, \mathbf{u_l}) + \frac{(\mathbf{r}, \mathbf{u_k})(\mathbf{r}, \mathbf{u_l})}{r^2}\Big] \\ &= \frac{< E >}{16\pi\mu(1-\nu)r}\Big[\eta(\mathbf{u_k}, \mathbf{u_l}) + \frac{(\mathbf{r}, \mathbf{u_k})(\mathbf{r}, \mathbf{u_l})}{r^2}\Big] \end{aligned} \tag{C.22}$$

where $\eta = 3 - 4\nu$.

Now according to L.E. Reichel's book, the response of fluctuations of energy in a randomly distributed system can be expressed in terms of covariance or correlation function for equilibrium fluctuations. Therefore, objective energy function for our fracture modeling from equation C.22 is,

$$E = \sum_{k=1}^{N}\sum_{\substack{l=1 \\ k\neq l}}^{N} A u_k u_l [\eta |cos(\theta_k - \theta_l)| + |cos(\alpha - \theta_l) cos(\alpha - \theta_k)|]/r_{kl} \tag{C.23}$$

where N is the number of fractures in the system and α, θ_k and θ_l are the orientation of distance vector r and fractures u_k and u_l with respect to the horizontal, respectively.

VITA

Ravi Shekhar was born in Bihar, India. He received his B.S. and M.S. degree in applied geology from Indian Institute of Technology, Kharagpur, India in 2001 and 2003, respectively. He immediately joined Texas A&M University for his Ph.D. in geophysics. He started his research under Dr. Richard Gibson in Fall, 2003. His research interests are rock physics, reservoir characterization integrating geology, geophysics and engineering, and geophysical modeling. He received his Ph.D. in May 2008. He will start working with ExxonMobil Upstream Research Company. He can be reached at the Dept. of Geology and Geophysics, Dr. Richard Gibson, 3115 Texas A&M University, College Station, TX 77843. His email address is ravisk9822213@yahoo.com.

This document was typeset in LaTeX by Ravi Shekhar.